High Energy Particles in Hot Accretion Flows onto a Supermassive Black Hole

Shigeo Kimura

Department of Earth and Space Science

Graduate School of Science

Osaka University, Osaka, JAPAN

1-1 Machikaneyama-cho, Toyonaka, Osaka 560-0043, Japan

kimura@vega.ess.sci.osaka-u.ac.jp

February 2015

Abstract

Active galactic nuclei (AGNs) are believed to emit radiations using the gravitational energy released through accretion onto black holes. For low accretion rates, the flows are hot and tenuous due to the inefficient cooling. This is called the radiatively inefficient accretion flows (RIAFs). The relaxation time for protons is typically longer than the infall time in RIAFs. Thus, non-thermal protons naturally exist inside the flows. The non-thermal protons can escape from the flow directly through diffusive motion. They are likely to generate the neutrinos and gamma rays through the interaction with protons or photons. The generated particles are also able to escape. Since the escaping particles carry away some amount of energy, the non-thermal particles can potentially affect the dynamical structure of the flow. The observational possibility of these escaping particles are worth investigating because the origin of extraterrestrial neutrinos detected by the IceCube is likely to be astrophysical. In this thesis, we address two issues: the effects of non-thermal particles on the dynamical structure of RIAFs, and the neutrino emission from Low-Luminosity AGNs (LLAGNs).

In the first part of this thesis, we study the effects of non-thermal particles on the dynamical structure of RIAFs using one-dimensional equations including the feedback from non-thermal particles consistently. From the steady state solutions, we find that the non-thermal particles do not affect the dynamical structure very much when their energy density is less than that of the thermal particles. For the cases that the non-thermal particles dominate over the thermal particles, the temperature of thermal particles are much lower than that without non-thermal particles. However, the dynamical structures are still advection dominated, and the physical

quantities except the temperature do not change by more than an order of magnitude. For the flow structure to change to a Keplerian disk, the escaping protons need to extract almost all the energy released. Since this situation is quite extreme, we conclude that it is difficult that the non-thermal particles affect the dynamical structure of the hot accretion flows.

In the second part of this thesis, we study the emission of neutrinos and cosmic-ray protons from RIAFs in LLAGNs. We calculate the energy spectrum of the relativistic protons in RIAFs using the Fokker-Planck equation with the one-zone approximation. We estimate the timescales of acceleration, escape, and cooling in RIAFs, and find that the diffusive escape suppresses the acceleration of protons for a typical LLAGN. The energy of protons in LLAGNs can be as high as $E_p \sim 10^{16}$ eV for reasonable parameters. The neutrinos are produced by both pp and $p\gamma$ reactions. The efficiency of meson production is at most 10%. We calculate the diffuse neutrino intensity, and find that the observed IceCube data can be fitted for reasonable parameters if non-thermal protons gain $\sim 1\%$ of the accretion luminosity. Although LLAGNs are much fainter than quasars, they can contribute to the diffuse neutrino intensity owing to their high number density.

Contents

Acknowledgements

I am deeply grateful to Professors Fumio Takahara and Kenji Toma for fruitful discussions and continuous support. I am also grateful to Professor Toru Tsuribe for his guidance and support. I would like to express my gratitude to Professors Kentaro Nagamine, Yutaka Fujita, and Hideyuki Tagoshi for valuable support and advice over my research life. I would like to thank Professor Kohta Murase for helpful comments and useful discussions. I would like to thank the past and present members of the Theoretical Astrophysical Group in Osaka University for great discussions and pleasant talks, and Secretary Ms. Yasuko Nishii for her kind support. I thank my family and friends for their support throughout my life.

This work is supported by the JSPS Research Fellowship for Young Scientists (251784).

Chapter 1

Introduction

Active galactic nuclei (AGNs) are one of the most powerful objects in the Universe. They emit strong radiations ranging from radio to X-rays or gamma rays. It is believed that the radiations are produced using the gravitational energy through the accretion onto supermassive black holes (SMBHs) located at the centers of galaxies. Since AGNs have strong magnetic fields with large spatial scales, they are considered as a possible source of the high energy cosmic rays including neutrinos. Recently, the neutrino telescope IceCube detected the extraterrestrial neutrinos (Aartsen et al. 2013a, 2014). Although the origin of IceCube neutrinos are still unknown, AGNs are viable candidates. In this chapter, we review the general properties of the accretion flow and observations of the cosmic rays.

1.1 General introduction of accretion flows

Many X-ray sources were discovered in 1960s, and most of them are located at the same positions as the usual stars. Since it seems difficult for the stars to emit such strong and steady X-rays, they are expected to be binaries consisting of a usual star and a compact object. It is expected that the circumstellar matters accreting onto the compact object emit strong and steady X-rays. The released energy per particle by accretion onto the compact

objects is about $0.1 m_p c^2 \sim 100$ MeV, which is much greater than that by the nuclear fusion ~ 7 MeV. Thus, the accretion onto compact objects are suitable for explaining the X-ray sources if sufficient materials are able to fall onto them.

In general, materials accreting onto the compact objects have some angular momentum. They cannot fall directly because of the centrifugal barrier, and a rotationally supported disks are likely to form around the compact objects. The angular momentum should be transported outward for continuous accretion. Ordinary molecular viscosity is too weak to transport the angular momentum efficiently. Turbulent viscosity seems important in the accretion flows, because high Reynolds numbers are expected there. Shakura & Sunyaev (1973) introduced a phenomenological viscosity called the "alpha prescription," and found the solutions for the "standard" accretion disks emitting thermal X-rays or ultraviolet photons (see Section 2). Although the origin of turbulent viscosity was one of the biggest problems in astrophysics for a long time, Balbus & Hawley (1991) showed that weakly magnetized plasma with differential rotation is unstable, and the non-linear growth of this instability, called the magneto-rotational instability (MRI), can produce strong viscosity including both Reynolds stress and Maxwell stress (see also Velikhov 1959; Chandrasekhar 1961). Therefore, it is believed that the materials accreting onto the compact objects can emit strong X-rays.

However, the standard disk model cannot explain all the phenomena related to accretion onto compact objects, and this problem has been actively discussed for a long time. Observations find that some X-ray binaries consist of a star and a black hole, whose mass is typically $10 M_\odot$. It has been shown that there are two major states in accretion flows onto black holes. The upper panel of Figure 1.1 shows the schematic and observed spectra of these two states (Poutanen & Coppi 1998). One is the "high-soft" state that has a strong thermal component and a weak power-law tail. An optically thick accretion disk around the black hole emits this thermal component. The power-law tail may be produced by the inverse Compton scattering in the hot plasma located above the accretion disk. The other is the "low-hard" state that has a hard power-law component. Since there is no thermal component, an optically thin

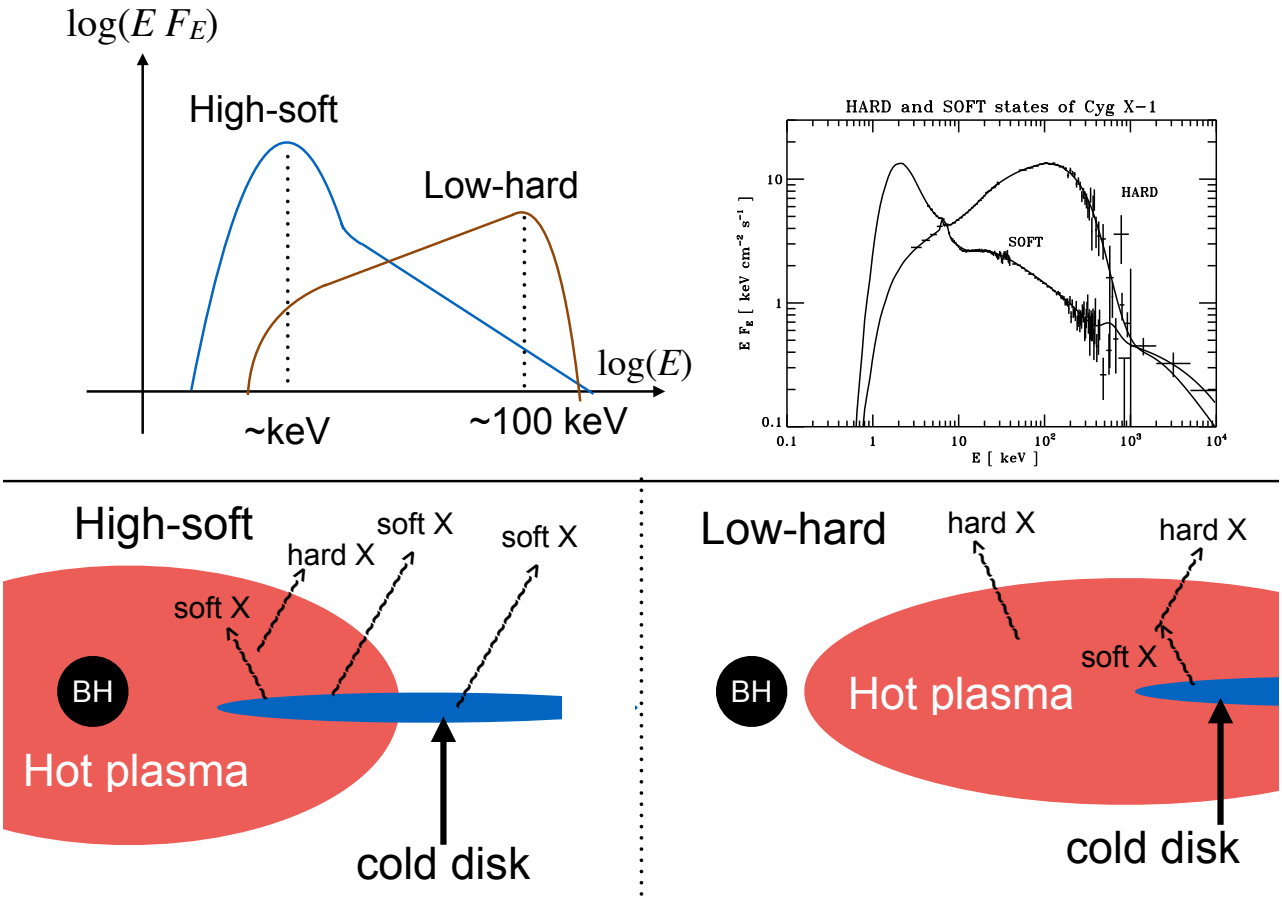

Figure 1.1: *Upper panel*: The schematic spectrum of the two states (left) and the observed spectrum in Cyg X-1 (right). The right figure is taken from Figure 1 of Poutanen & Coppi (1998) with permission from one of the authors. The high-soft state, observed by XTE/PCA and OSSE, has a thermal component and a soft power-law tail. The low-hard state, observed by Ginga, OSSE and COMPTEL, has a hard power-law component without any thermal component. *Lower panel*: The schematic picture of the accretion flow for the two states (e.g., Esin et al. 1997; Zdziarski et al. 2002). The geometrically thin disk is close to the black hole in the high-soft state, while only the hot plasma is close to the black hole in the low-hard state.

flow seems to exist around the black hole. The flow probably consists of hot plasma emitting hard X-rays through the inverse Compton process. The lower panel of Figure 1.1 shows the schematic picture of the two states (e.g., Esin et al. 1997; Zdziarski et al. 2002). The low-hard state is realized when the mass accretion rate is much lower than the Eddington accretion rate $\dot{M}_{\rm Edd} = L_{\rm Edd}/c^2$, where $L_{\rm Edd} = 4\pi cGm_pM_{\rm BH}/\sigma_{\rm T}$ is the Eddington luminosity. The high-soft state is realized when the mass accretion rate is comparable to $\dot{M}_{\rm Edd}$. Transition between these two states are observed for most of the black hole binaries. Nevertheless, the physical conditions of accretion flows during the transition are not understood well. This is one of the biggest problems in the study of accretion flows.

Accretion flows onto a black hole are also seen at the centers of galaxies, including the Milky Way. Some galaxies host a nuclei in their center, which is much brighter than other usual galaxies. This is called the active galactic nuclei (AGNs). It is likely that a supermassive black hole (SMBH) whose mass is typically $10^6 - 10^9 M_\odot$ exists at the center, and the accreting materials emit powerful radiation using the released gravitational energy. Although only $\sim$1% of galaxies have such luminous AGNs, it is believed that most galaxies host SMBH at their centers. Observations of AGNs show that there are also two states of accretion flows corresponding to low-luminosity AGNs (LLAGNs) and luminous AGNs called quasars. The LLAGNs typically have bolometric luminosities of $L_{\rm bol} \sim 10^{40}$ erg s^{-1}, while the quasars are much brighter with $L_{\rm bol} \sim 10^{45}$ erg s^{-1}. This difference probably originates from different mass accretion rates for these two types of AGNs. The upper panel of Figure 1.2 shows the average spectral energy distribution (SED) of radio-quiet AGNs binned by Eddington ratio (Ho 2008), including radio-quiet quasars (open circles) and low-luminosity AGNs (open squares). Here, the luminosity is normalized such that the LLAGNs have the same luminosity as the quasars at 1 μm for comparison. The quasars have a peak in the ultraviolet range called the "big blue bump," which may correspond to the thermal emission from the standard disks with high mass accretion rate. On the other hand, LLAGNs have a dip in the ultraviolet range. This suggests that there is no standard disk but a hot accretion flow near the SMBH for LLAGNs (see the

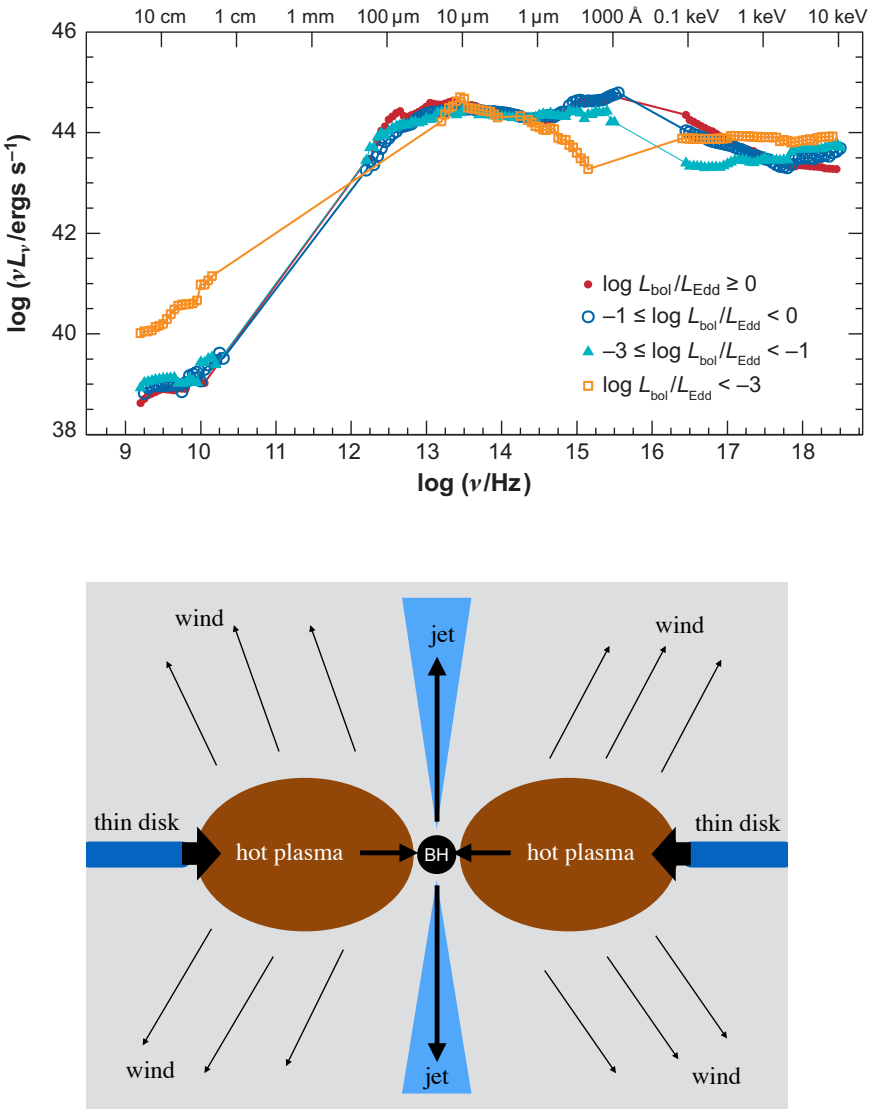

Figure 1.2: *Upper panel*: The average SED for radio-quiet AGNs binned by Eddington ratio. This figure is taken from Figure 7 of Ho (2008) with a permission from the author and the Annual Review of Astronomy and Astrophysics. The quasars (open circles) have a bump, while LLAGNs (open squares) have a dip in the ultraviolet range. The SED of LLAGNs is scaled such that it has the same luminosity at 1 μm for comparison. *Lower panel*: The schematic picture of an LLAGN. There are a hot accretion flow around an SMBH, a thin disk in the outer region, and jets and winds around the SMBH. The arrows show the flow directions of the plasma.

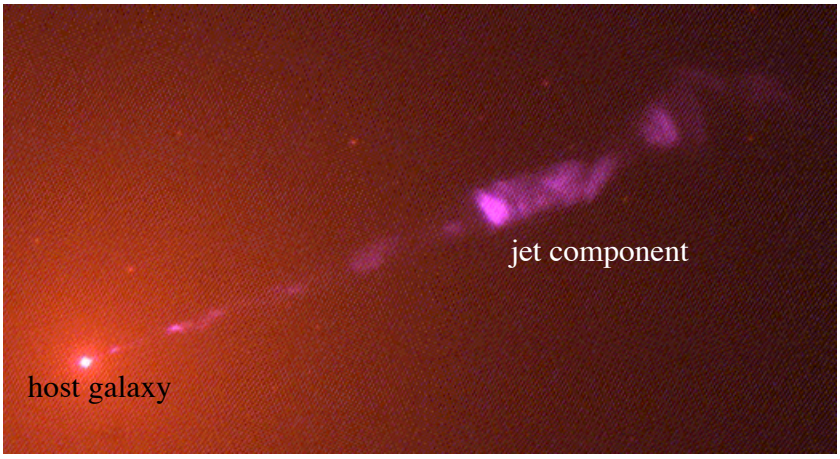

Figure 1.3: The jet from a radio galaxy M87 observed by the Hubble Space Telescope. We can see that a jet component is launched from the host galaxy, but the counter jet component is invisible due to the relativistic effect. (Photo credit: NASA, http://hubblesite.org/gallery/album/galaxy/pr1999043c/web/)

lower panel of Figure 1.2).

The physics of accretion flows seems closely related to other astrophysical phenomena that have not been understood well yet. Some AGNs are very bright in the radio band (radio-loud AGNs), and some of them have external jet components (see Figure 1.3). These radio emissions are considered to originate from the electrons accelerated at shocks produced by the jets. These jets are considered to be relativistic because the counter jet is not observed due to the relativistic beaming effect. Production mechanism of these relativistic jets is one of the biggest problems in high-energy astrophysics. LLAGNs are likely to have jets because LLAGNs are usually bright in the radio band (see the upper panel of Figure 1.2). The hot accretion flows are probably related to jet production because their Bernoulli parameters are

positive (see Chapter 2).

AGNs may accelerate the protons up to ultrarelativistic energy owing to the strong magnetic fields with large scales. Some mechanisms of particle acceleration at the vicinity of SMBHs are proposed, such as the Fermi acceleration at an accretion shock (Begelman et al. 1990; Stecker et al. 1991), the electric field acceleration around a rotating black hole (Levinson 2000), the shear acceleration in an accretion disk (Katz 1991), and the stochastic acceleration at a "corona" located above the disk (Dermer et al. 1996). The accelerated protons naturally interact with surrounding protons and/or photons, and generate neutrinos and gamma rays. The multi-messenger observations of ANGs can probably restrict some models of particles acceleration.

The activity of AGNs is expected to affect the galaxy formation and evolution. Some parts of the gravitational energy released through accretion is carried away by photons and/or materials as outflows. These photons and materials heat up and/or push away surrounding materials, which may affect the mass accretion rate onto the SMBH. In addition, observations show the tight correlation between SMBH mass and the velocity dispersion of bulge component of the host galaxies (e.g., Kormendy & Ho 2013). Thus, SMBHs and host galaxies are likely to coevolve, affecting each other. Therefore, understanding the physics of accretion flows is important not only for high-energy astrophysics but also for galaxy formation and evolution.

As described above, accretion flows are related to many astrophysical phenomena. However, there still remain some problems to be solved, such as the relation to jet production and the physics of state transition. In order to understand the accretion phenomena, we should clarify the effects of magnetic fields, radiation fields, general relativity, and/or non-thermal processes. Although the numerical simulations are shedding light on these effects (e.g., Ohsuga & Mineshige. 2011; Narayan et al. 2012; Hoshino 2013), we are still far from the understanding of whole picture of accretion phenomena.

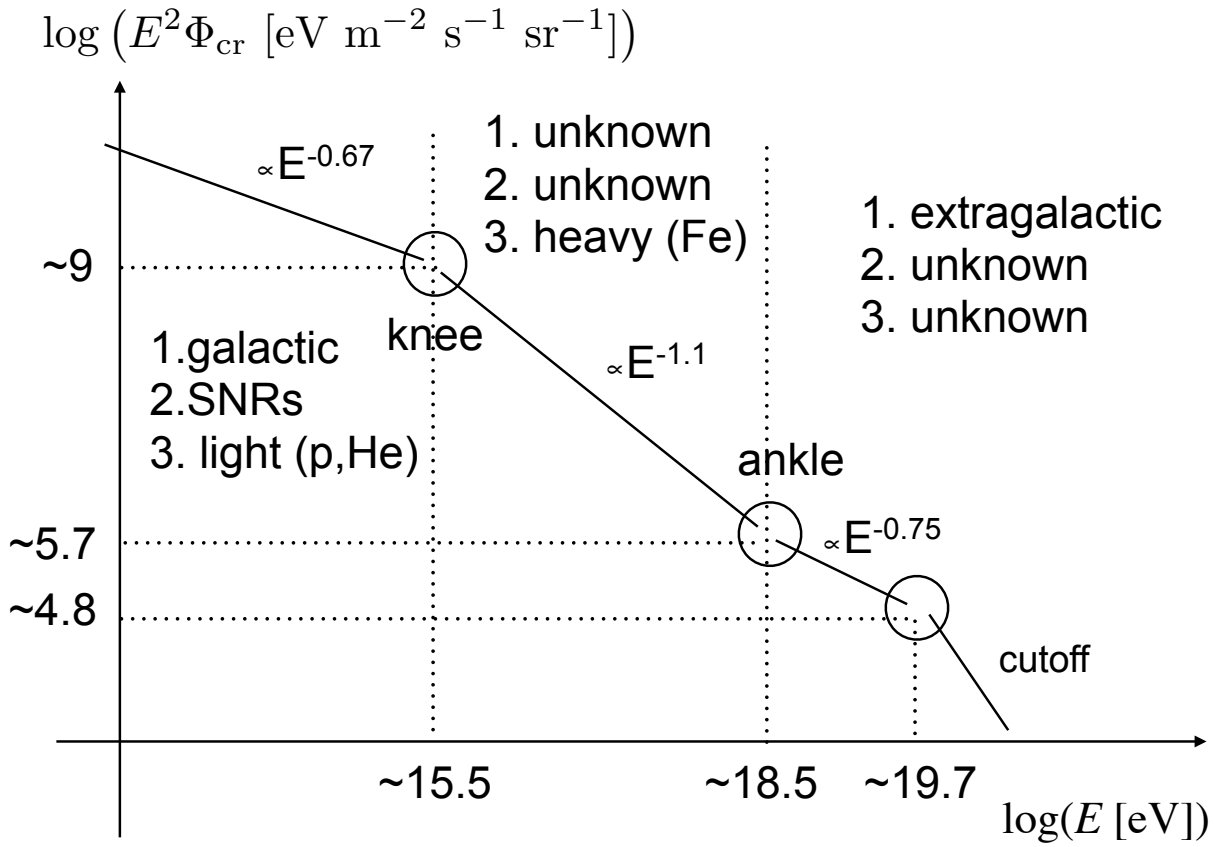

Figure 1.4: Schematic picture of the cosmic-ray spectrum of charged particles. The spectrum is expressed as a broken power-law function. For each region, we show (1) extragalactic or galactic, (2) source candidates, and (3) the main composition.

1.2 Observations of cosmic rays

The cosmic-ray spectrum of charged particles are described by a power-law function, introducing two break points called "knee" and "ankle." Figure 1.4 shows the schematic picture of the cosmic-ray spectrum. It is believed that the cosmic rays below the knee ($E < 10^{15.5}$ eV) originate from supernova remnants in our Galaxy. The origin between the knee and the

ankle is still unclear. It is controversial even whether the sources are extragalactic or not. The cosmic rays above the ankle ($E > 10^{18.5}$ eV), called ultra-high energy cosmic rays (UHECRs), are likely to come from extragalactic sources, although the sources are unknown. The cosmic rays at $E > 10^{19.7}$ eV are expected to lose their energy by interaction with the cosmic microwave background photons (Greisen 1966; Zatsepin & Kuzmin 1966). This theoretical prediction is consistent with the spectrum of UHECRs observed by the High Resolution Fly's Eye (Abbasi et al. 2008, HiRes,), the Pierre Auger Observatory (PAO, Abraham et al. 2008), and the Telescope Array (TA, Abu-Zayyad et al. 2013).

The cosmic rays below about 1 PeV are mainly protons as shown by the Russian Nippon Joint Balloon Collaboration (RUNJOB, Derbina et al. 2005). Tibet AS-gamma Experiment (Tibet) shows that the composition seem to shift to the heavy-nuclei dominant around the knee (Amenomori et al. 2006). The Karlsruhe Shower Core and Array Detector-Grande (KASCADE-Grande) argue that the heavy nuclei are dominant for $E_p \lesssim 10^{17}$ eV (Apel et al. 2013). The cosmic rays around the ankle are probably protons, while the composition for $E > 10^{19}$ eV is still controversial. HiRes and TA collaborations report the proton-dominated composition (Abbasi et al. 2010, 2015), while PAO indicate the heavy nuclei-dominated (Abraham et al. 2010).

The neutrino energy detected by IceCube ranges from TeV to PeV, whose spectrum is shown in Figure 1.5. Assuming a single power-law function, the neutrino spectrum per flavor is expressed as

$$E_\nu^2 \Phi_\nu = 2.06 \times 10^{-8} \left(\frac{E_\nu}{10^5 \mathrm{GeV}} \right)^{-0.46} \mathrm{GeV\ cm^{-2}\ sr^{-1}\ s^{-1}}. \tag{1.1}$$

This energy flux for PeV range is the same order as that of UHECRs. This fact motivates some researchers to consider that the sources of UHECRs and the IceCube neutrinos are the same, although their energy range is different by about two orders of magnitude.

In the astrophysical context, the high-energy neutrinos are expected to be generated by the interaction of high-energy protons with the energy of $E_\nu \sim 0.05 E_p$. At first, the cosmic-ray

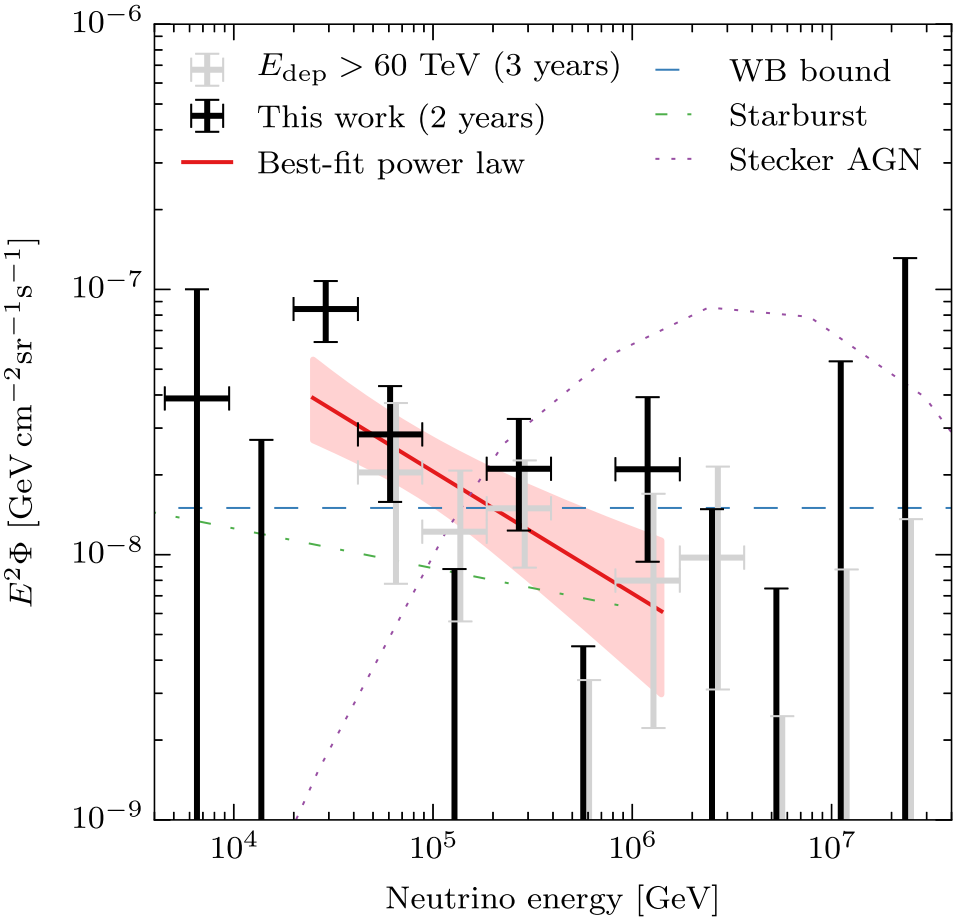

Figure 1.5: The neutrino spectrum reported by the IceCube collaboration (Aartsen et al. 2015) with the permission from the author. The thin lines shows the neutrino spectra from the theoretical predictions, including the UHECR model (dashed, Waxman & Bahcall 1998), AGN core model (dotted, Stecker 2005), and starburst galaxies (dot-dashed, Loeb & Waxman 2006). Copyright (2015) by The American Physical Society.

protons produce pions through the interaction with protons and/or photons:

$$p + p \rightarrow p + p(n) + \pi^0(\pi^+) + A\pi^+ + A\pi^- + B\pi^0, \tag{1.2}$$

$$p + \gamma \rightarrow p(n) + \pi^0(\pi^+), \tag{1.3}$$

where $2A + B$ is the number of multiple pions. Then, the generated pions are decay to gamma rays, neutrinos, electrons, and positrons as follows:

$$\pi^0 \rightarrow 2\gamma, \tag{1.4}$$

$$\pi^+ \rightarrow \mu^+ + \nu_\mu, \quad \mu^+ \rightarrow e^+ + \nu_e + \overline{\nu_\mu}, \tag{1.5}$$

$$\pi^- \rightarrow \mu^- + \overline{\nu_\mu}, \quad \mu^- \rightarrow e^- + \nu_\mu + \overline{\nu_e}. \tag{1.6}$$

The generated neutrinos can travel the cosmological distance owing to the small cross section of the weak interaction. In reality, the pp and $p\gamma$ interaction creates other particles, such as eta mesons and electron-positron pairs, but we neglect them in this thesis because they are sub-dominant (e.g. Kawasaki et al. 2005; Kelner et al. 2006; Kelner & Aharonian 2008).

Since the pion energy is roughly equally divided among their final products (e.g., Kelner et al. 2006), the flavor ratio of the neutrinos at the sources is $\Phi_{\nu_e} : \Phi_{\nu_\mu} : \Phi_{\nu_\tau} = 1 : 2 : 0$, where Φ_{ν_l} indicate the combined flux of ν_l and $\overline{\nu_l}$. Since the neutrinos travel greater distance than the oscillation length, the neutrino oscillation converts the flavor ratio to $\Phi_{\nu_e} : \Phi_{\nu_\mu} : \Phi_{\nu_\tau} = 1 : 1 : 1$ after the propagation from sources to Earth (e.g., Learned & Pakvasa 1995). Note that neutrino oscillation does not always make the flavor ratio $1 : 1 : 1$. For example, the observed flavor ratio is $\Phi_{\nu_e} : \Phi_{\nu_\mu} : \Phi_{\nu_\tau} = 1 : 1.8 : 1.8$ (e.g., Gonzalez-Garcia & Nir 2003), when the flavor ratio at the sources is $\Phi_{\nu_e} : \Phi_{\nu_\mu} : \Phi_{\nu_\tau} = 0 : 1 : 0$. This flavor ratio is realized if the cooling time of muons is much shorter than their lifetimes (Kashti & Waxman 2005).

Many models are suggested to explain the IceCube neutrinos, such as AGN jets (e.g., Murase et al. 2014), AGN cores (e.g., Stecker 2013), galaxy mergers (Kashiyama & Mészáros 2014), low-luminosity gamma-ray bursts (Murase & Ioka 2013), and starburst galaxies (e.g., Tamborra et al. 2014). However, their origin is still controversial. The models are roughly

categorized into two types by the way of neutrino production. One is the *pp* models in which hadronic interaction creates the neutrinos, and the other is the $p\gamma$ models in which the neutrinos are generated by photomeson production. The observation of isotropic gamma-ray background (IGB) observed by *Fermi* strongly restricts the *pp* models. The profile of neutrino spectra produced by *pp* collisions is similar to those of protons. For the soft proton spectra as $\Gamma > 2.2$, where $dN/dE_p \propto E_p^{-\Gamma}$, the resultant gamma-ray flux exceeds IGB (Murase et al. 2013), while the observed neutrino spectrum is soft ($\Gamma \simeq 2.3-2.5$). Therefore, *pp* models with single power-law protons are disfavored to explain the IceCube neutrinos. On the other hand, $p\gamma$ models are not restricted by IGB because the neutrino spectra in these models are modified by the target photon spectra. However, some $p\gamma$ models, including AGN models, suffer from the lack of target photons when we consider the relatively low energy neutrinos $E_\nu \lesssim 100$ TeV. The required target photon energy is $E_\gamma \gtrsim 100$ eV, which is higher than the average temperature of the accretion disks in observed AGNs. Thus, it is not easy to explain the IceCube neutrinos by the single component models. A two component model is proposed to avoid these difficulties (Chen et al. 2014).

1.3 Purpose and content

In this thesis, we focus on the non-thermal particles inside hot accretion flows that have not been studied very well up until now. The hot accretion flows are so hot and tenuous that plasma can be collisionless, which means that the Coulomb interactions are inefficient. If turbulent magnetic fields are inside the collisionless plasma, non-thermal and high-energy particles can be generated through magnetic reconnection or stochastic acceleration. The purpose of this thesis is to discuss the effects and influences of these particles. It is interesting to study the effects on the dynamical structure because non-thermal particles may carry away some amount of energy through the neutrino production or diffusive escape. The detection of extraterrestrial neutrinos motivates us to investigate the energy spectrum of escaping particles.

This thesis consists of following chapters. In Chapter 2, we review the physics about hot accretion flows. We formulate a set of one-dimensional equations that describes accretion flows, and give basic properties of the standard accretion disks and the hot accretion flows. Then, we estimate some timescales in the hot accretion flows to introduce the notion of collisionless flows, and discuss the effects and influence of the non-thermal particles. In Chapter 3, we see the effect of non-thermal particles on dynamical structure of accretion flows. We reformulate the set of equations including the effects of non-thermal particle, and show that the non-thermal particles do not affect the dynamical structure very much. In Chapter 4, the neutrino and cosmic-ray proton emission from LLAGNs are discussed. We estimate the neutrino and cosmic-ray luminosities from LLAGNs using a one-zone approximation, and suggest LLAGNs as an origin of the extraterrestrial neutrinos reported by the IceCube collaboration (Aartsen et al. 2013a,b). We summarize the overall results in Chapter 5.

Chapter 2

Basic Picture of Hot Accretion Flows

In this chapter, we summarize the characteristics of the hot accretion flows. The basic picture of the hot accretion flows is quite different from the standard disks. We derive the solutions of hot accretion flows, and discuss some characteristics. In addition, we introduce the notion of collisionless flows, which is important for the non-thermal particles inside the flows.

2.1 Basic equations of accretion flows

Accretion flows are usually described as viscous fluids, so the basic equations are the equation of continuity, the momentum conservations, and the energy equation:

$$\frac{\partial \rho}{\partial t} + \boldsymbol{\nabla} \cdot (\rho \boldsymbol{v}) = 0, \tag{2.1}$$

$$\frac{\partial (\rho \boldsymbol{v})}{\partial t} + \boldsymbol{\nabla} \cdot (\rho \boldsymbol{v}\boldsymbol{v}) = -\boldsymbol{\nabla} p_{\rm tot} + \boldsymbol{F} - \boldsymbol{\nabla} \cdot \boldsymbol{\Pi}, \tag{2.2}$$

$$\frac{\partial (\rho \epsilon)}{\partial t} + \boldsymbol{\nabla} \cdot (\rho \epsilon \boldsymbol{v}) = -p_{\rm g} \boldsymbol{\nabla} \cdot \boldsymbol{v} + q_{\rm vis} - q_{\rm cool}, \tag{2.3}$$

where $\boldsymbol{F} = -\boldsymbol{\nabla}\Phi$ is the gravity, $\boldsymbol{\Pi}$ is the viscous stress tensor, $p_{\rm g}$ is the gas pressure, $p_{\rm tot}$ is the total pressure including magnetic pressure, $q_{\rm vis}$ is the viscous heating rate, and $q_{\rm cool}$ is the cooling rate. Derivation of Equation (2.3) is described in Appendix A. In addition, we often

use the equation of state for ideal gas,

$$p_{\rm g} = (\gamma - 1)\rho\epsilon, \tag{2.4}$$

where γ is the specific heat ratio and ϵ is the specific internal energy.

2.1.1 Useful approximations

For simplicity, we often use some assumptions to obtain the solutions of accretion flows. Hereafter, we use the cylindrical coordinate $(r,\ \phi,\ z)$. First, we assume the axisymmetric flow, i.e., $\partial/(\partial\phi) = 0$. Second, we use hydrostatic equilibrium for the vertical direction, in which the scale height of the flow H is

$$H \approx c_{\rm s}/\Omega_{\rm K}, \tag{2.5}$$

where $\Omega_{\rm K}$ is the Keplerian angular velocity and $c_{\rm s} = \sqrt{p_{\rm tot}/\rho}$ is the effective sound velocity. Dividing by r, we can write Equation (2.5) as $H/r \simeq c_{\rm s}/v_{\rm K}$. Thus, geometrically thin disks satisfy $c_{\rm s} \ll v_{\rm K}$, which means the pressure is negligible compared to the gravity. When the radial velocity is greater than the sound speed, this assumption is not valid (see Appendix A). Third, we use the alpha viscosity, where kinetic viscosity ν is described as

$$\nu \approx \alpha c_{\rm s} H. \tag{2.6}$$

Here, α is a parameter that represents the strength of turbulence. This is a phenomenological expression of turbulent viscosity whose eddy scale is $\sqrt{\alpha}H$ and eddy velocity is $\sqrt{\alpha}c_{\rm s}$.

Although we should compute in Schwarzschild-metric or Kerr-metric to include the gravity correctly, we approximate the gravity with the Newtonian framework. When our interest is in the region far from the black hole, we often reduce the gravity to a Newtonian one, $\Phi = -GM/\sqrt{r^2 + z^2}$. When we consider the global structure of accretion flows, we often use the pseudo Newtonian gravity

$$\Phi = -\frac{GM}{\sqrt{r^2 + z^2} - R_{\rm S}}, \tag{2.7}$$

where $R_{\rm S} = 2GM/c^2$ is the Schwarzschild radius. This potential reproduces the innermost stable circular orbit (ISCO) at $r = 3R_{\rm S}$, which is the same for the Schwarzschild metric. Both potentials depend only on the distance from the central object, i.e., $\Phi(r, z) = \Phi(\sqrt{r^2 + z^2})$

2.1.2 Vertical integration

Next, we integrate the basic equations to the vertical direction, introducing the integrated variables such as the surface density $\Sigma = \int \rho(z)dz$. This integration allows us to write down the basic equations as one-dimensional equations. We have to assume the vertical structure of the flow for this integration. We assume that density, radial velocity, and angular momentum are constant for the vertical direction, and use vertically integrated pressure and vertically averaged internal energy.

Equation (2.4) is integrated as

$$P_{\rm g} = (\gamma - 1)\Sigma E, \tag{2.8}$$

where we use vertically integrated pressure $P_{\rm g} = \int p_{\rm g} dz$ and vertically averaged specific internal energy $E = \int \epsilon dz/(2H)$.

The equation of continuity and the angular momentum conservation are written as

$$\frac{\partial \rho}{\partial t} + \frac{1}{r}\frac{\partial}{\partial r}\left(r\rho v_r\right) + \frac{\partial}{\partial z}\left(\rho v_z\right) = 0, \tag{2.9}$$

$$\frac{\partial(\rho l_z)}{\partial t} + \frac{1}{r}\frac{\partial}{\partial r}\left(r\rho l_z v_r\right) + \frac{\partial}{\partial z}\left(\rho l_z v_z\right) = \frac{1}{r}\frac{\partial}{\partial r}\left(r^3 \nu \rho \frac{d\Omega}{dr}\right), \tag{2.10}$$

where Ω is the angular velocity and $l_z = r^2\Omega$ is the specific angular momentum. We assume that the stress tensor has only $r\phi$ component because velocity shear is the strongest in this direction. After taking $\int_{-\infty}^{\infty} dz$, we can write down these equations as

$$\frac{\partial \Sigma}{\partial t} + \frac{1}{r}\frac{\partial}{\partial r}\left(r\Sigma v_r\right) = 0, \tag{2.11}$$

$$\frac{\partial(\Sigma l_z)}{\partial t} + \frac{1}{r}\frac{\partial}{\partial r}\left(r\Sigma l_z v_r\right) = \frac{1}{r}\frac{\partial}{\partial r}\left(r^3 \nu \Sigma \frac{d\Omega}{dr}\right), \tag{2.12}$$

where we assume $\rho = 0$ for $z > H$.

The radial momentum conservation is represented as

$$\frac{\partial}{\partial t}(\rho v_r) + \frac{1}{r}\frac{\partial}{\partial r}(r\rho v_r^2) + \frac{\partial}{\partial z}(\rho v_z v_r) = -\frac{\partial p_{\rm tot}}{\partial r} + \rho r\Omega^2 - \rho\frac{d\Phi}{dr}, \tag{2.13}$$

Expanding Φ with the condition $z/r \ll 1$ and neglecting terms of the order $(z/r)^3$, we integrate Equation (2.13) as

$$\frac{\partial}{\partial t}(\Sigma v_r) + \frac{1}{r}\frac{\partial}{\partial r}(r\Sigma v_r^2) = -\frac{\partial P_{\rm tot}}{\partial r} + \Sigma r(\Omega^2 - \Omega_{\rm K}^2) - \Omega_{\rm K}\frac{d\Omega_{\rm K}}{dr}\frac{\Sigma H^2}{3}, \tag{2.14}$$

where $P_{\rm tot} = \int dz p_{\rm tot}$ and

$$\Omega_{\rm K} = \sqrt{\frac{1}{r}\frac{\partial\Phi}{\partial r}}\Big|_{z=0} \tag{2.15}$$

is the Keplerian angular velocity. The last term of Equation (2.14) accounts for the z dependence of the radial component of the gravitational force (cf., Matsumoto et al. 1984).

The energy conservation is

$$\frac{\partial}{\partial t}(\rho\epsilon) + \frac{1}{r}\frac{\partial}{\partial r}(rv_r\rho\epsilon) + \frac{\partial}{\partial z}(v_z\rho\epsilon) = -p_{\rm g}\boldsymbol{\nabla}\cdot\boldsymbol{v} + q_{\rm vis} - q_{\rm cool}. \tag{2.16}$$

We evaluate the compression term $-p_{\rm g}\boldsymbol{\nabla}\cdot\boldsymbol{v}$. Equation (2.11) can be expressed as

$$\frac{d\ln\Sigma}{dt} = -\frac{1}{r}\frac{\partial}{\partial r}(rv_r), \tag{2.17}$$

where $d/dt = \partial/\partial t + \boldsymbol{v}\cdot\boldsymbol{\nabla}$ is the Lagrangian derivative. The equation of continuity is written as

$$\frac{d\ln\rho}{dt} = -\boldsymbol{\nabla}\cdot\boldsymbol{v}. \tag{2.18}$$

Using $\rho = \Sigma/(2H)$, we obtain

$$\boldsymbol{\nabla}\cdot\boldsymbol{v} = -\frac{d\ln\rho}{dt} = -\frac{d\ln\Sigma}{dt} + \frac{d\ln H}{dt} = \frac{1}{r}\frac{\partial}{\partial r}(rv_r) + \frac{d\ln H}{dt} \tag{2.19}$$

Since Σ and H are independent of z, we find that $\boldsymbol{\nabla}\cdot\boldsymbol{v}$ is independent of z. Thus, we can integrate the compressional heating term as

$$\begin{aligned} Q_{\rm V} = -\int p_{\rm g}\boldsymbol{\nabla}\cdot\boldsymbol{v}dz &= -\frac{P_{\rm g}}{r}\frac{\partial}{\partial r}(rv_r) - \frac{P_{\rm g}v_r}{H}\frac{\partial r}{\partial H} \\ &= -\frac{P_{\rm g}}{rH}\frac{\partial}{\partial r}(rHv_r). \end{aligned} \tag{2.20}$$

Here, we assume that $\partial/\partial t = 0$ since we are interested in the steady state solutions. Then, Equation (2.16) is integrated and written as

$$\frac{\partial}{\partial t}(\Sigma E) + \frac{1}{r}\frac{\partial}{\partial r}\left(r v_r \Sigma E\right) = Q_{\rm V} + Q_{\rm vis} - Q_{\rm cool}, \tag{2.21}$$

where $Q_{\rm vis}$ and $Q_{\rm cool}$ is the vertically integrated viscous dissipation rate and cooling rate, respectively. We write the viscous dissipation rate as

$$Q_{\rm vis} = \Sigma\nu\left(r\frac{\partial\Omega}{\partial r}\right)^2, \tag{2.22}$$

and the compressional heating rate is given in Equation (2.20). This treatment includes the effect of vertical velocity for compressional heating. This expression of compressional heating is the same as that of Le & Becker (2005) although its derivation is slightly different.

2.2 The standard disk solutions

Before describing hot accretion flows, we review the standard disk solutions derived by Shakura & Sunyaev (1973). These solutions, called Shakura-Sunyaev disks (SSDs), have a great success to explain the high-soft state of X-ray binaries and the big blue bump of quasars. Assumptions of the SSDs are summarized below:

1. Steady accretion flow $\partial/\partial t = 0$,
2. Newtonian gravity $\Phi = -GM_{\rm BH}/r$,
3. Optically thick plasma enough to emit thermal radiation,
4. Keplerian rotation $v_\phi = v_{\rm K} = \sqrt{GM_{\rm BH}/r}$,
5. Slow infall velocity $v_r \ll v_\phi$,
6. Geometrically thin disks satisfying $H \ll r$, which means $c_{\rm s} \ll v_{\rm K}$.

Since the disks are geometrically thin and optically thick, we express the cooling rate as diffusion toward the vertical direction,

$$Q_{\rm cool} = \frac{16\sigma_{\rm SB}T^3}{3\kappa\rho}\frac{\partial T}{\partial z} \approx \frac{32\sigma_{\rm SB}T_c^4}{3\kappa\Sigma}, \tag{2.23}$$

where T_c is the temperature at midplane $z = 0$, κ is the mean opacity in the disk, and $\sigma_{\rm SB}$ is the Stephan Boltzmann constant. We neglect the advection terms in the energy equation and momentum conservation because of low v_r. The pressure gradient force and the compressional heating are also neglected because we assume thin disk $r \ll H$. Then, we can write the basic equations as

$$\dot{M} = -2\pi r v_r \Sigma, \tag{2.24}$$

$$\Omega = \Omega_{\rm K}, \tag{2.25}$$

$$r v_r \Sigma l_z = r^3 \Sigma \nu \frac{d\Omega}{dr}, \tag{2.26}$$

$$\Sigma\nu\left(r\frac{\partial\Omega}{\partial r}\right)^2 = \frac{32\sigma_{\rm SB}T_c^4}{3\kappa\Sigma}, \tag{2.27}$$

where we neglect the effect of the inner boundary, considering only far away from the black hole. For simplicity, we assume Thomson scattering opacity $\kappa = \sigma_{\rm T}/m_p$, where $\sigma_{\rm T}$ is the Thomson cross section and m_p is the proton mass. We consider both radiation and gas pressure for equation of state as

$$p_{\rm tot} = p_{\rm g} + p_{\rm rad} = \frac{2\rho k_{\rm B} T_c}{m_p} + \frac{aT_c^4}{3}, \tag{2.28}$$

where $p_{\rm tot}$ is the total pressure, $p_{\rm rad}$ is the radiation pressure, $k_{\rm B}$ is the Boltzmann constant, and a is the radiation constant. The plasma is assumed to be completely ionized.

First, we consider a case that the gas pressure dominates over the radiation pressure. Then, the solution can be derived as follows (e.g., Shakura & Sunyaev 1973; Kato et al. 2008):

$$v_\phi = v_{\rm K} = 6.7 \times 10^9 \varpi_1^{-1/2} \ [{\rm g\ cm^{-2}}], \tag{2.29}$$

$$\Sigma = 1.7 \times 10^6 \alpha_{-1}^{-4/5} M_{\rm BH,7}^{1/5} \dot{m}^{3/5} \varpi_1^{-3/5} \ [{\rm g\ cm^{-2}}], \tag{2.30}$$

$$|v_r| = 4.3 \times 10^3 \alpha_{-1}^{4/5} M_{\rm BH,7}^{-1/5} \dot{m}^{2/5} \varpi_1^{-2/5} \ [{\rm cm\ sec^{-1}}], \tag{2.31}$$

$$T_c = 1.7 \times 10^6 \alpha_{-1}^{-1/5} M_{\rm BH,7}^{-1/5} \dot{m}^{2/5} \varpi_1^{-9/10} \ [{\rm K}], \tag{2.32}$$

$$H/r = 2.6 \times 10^{-3} \alpha_{-1}^{-1/10} M_{\rm BH,7}^{-1/10} \dot{m}^{1/5} \varpi_1^{1/20}, \tag{2.33}$$

where $\alpha_{-1} = \alpha/0.1$, $M_{\rm BH,7} = M_{\rm BH}/(10^7 M_\odot)$, $\varpi_1 = \varpi/10$. Note that $v_{\rm K}$ depends only on ϖ. The mass accretion rate and radius are normalized as $\dot{m} = \dot{M}/\dot{M}_{\rm Edd}$ and $\varpi = r/R_{\rm S}$, respectively. In this solution, the released gravitational energy is carried away by the thermal radiation, so that the disk temperature is cold enough to maintain $H \ll r$. The standard disks mainly emit X-ray photons for stellar mass black holes ($M_{\rm BH} \sim 10 M_\odot$) in X-ray binaries or ultraviolet photons for SMBHs ($M_{\rm BH} \sim 10^6 - 10^9 M_\odot$) in AGNs. The radial velocity is expressed as $v_r \sim \nu/r \simeq \alpha (H/r) c_{\rm s}$. Thus, $v_r \ll c_{\rm s}$ is satisfied when $H/r \ll 1$. The standard disk satisfies $v_r \ll c_{\rm s} \ll v_\phi$, which implies that the local thermal equilibrium is a good approximation.

If we consider closer region to the black hole or higher mass accretion rate, the temperature is so high that radiation pressure dominates over the gas pressure. This gives another solution of SSD (Shakura & Sunyaev 1973; Kato et al. 2008):

$$v_\phi = v_{\rm K} = 6.7 \times 10^9 \varpi_1^{-1/2} \ {\rm g\ cm^{-2}}, \tag{2.34}$$

$$\Sigma = 3.2 \times 10^4 \alpha_{-1}^{-1} \dot{m}^{-1} \varpi_1^{3/2} \ [{\rm g\ cm^{-2}}], \tag{2.35}$$

$$|v_r| = 2.4 \times 10^5 \alpha_{-1} \dot{m}^2 \varpi_1^{-5/2} \ [{\rm cm\ sec^{-1}}], \tag{2.36}$$

$$T_c = 6.5 \times 10^5 \alpha_{-1}^{-1/4} M_{\rm BH,7}^{-1/4} \varpi_1^{-3/8} \ [{\rm K}], \tag{2.37}$$

$$H/r = 1.6 \times 10^{-2} \dot{m} \varpi_1^{-1}. \tag{2.38}$$

We note that this solution is unstable to both thermal and viscous instabilities (e.g., Kato et al. 2008), and thus, it seems unrealistic. However, observations suggest the existence of this

radiation-dominated SSDs (e.g., Ross et al. 1992). Although the thermal stability of this disks is investigated by numerical simulations including both radiation and magnetic fields (Hirose 2009; Jiang et al. 2013), it is still controversial.

As the mass accretion rate becomes higher, temperature becomes higher, so that the disk becomes thicker with $H \sim r$ when $\dot{m} \sim 10$. This makes the infall velocity greater, and advection of the thermal energy becomes important. This effect gives another solution of accretion disks, so called the "slim disks" (Abramowicz et al. 1988). In this solution, the optical depth is so large that the photons cannot escape efficiently. Most of the photons fall into the black hole together with the accreting materials.

2.3 The power-law solutions

When the mass accretion rate is low enough, the radiation cooling is so inefficient that the hot accretion flow, so called the radiatively inefficient accretion flow (RIAF), is likely to be realized. The RIAF model also succeed in explaining the low-hard state of X-ray binaries and LLAGNs (e.g., Yuan & Narayan 2014; Nemmen et al. 2014). Although we neglect the advection and pressure terms in SSDs, these effects are important for the hot accretion flows. The advection dominated accretion flows (ADAFs, Narayan & Yi 1994) is a solution of hot accretion flows that includes the effect of advection. In this section, we derive the power-law solution of ADAF. This gives us the basic picture of hot accretion flows.

As a set of basic equations for ADAFs, we have four Equations (2.11), (2.12), (2.14), (2.21), with four variables (Σ, v_r, $c_{\rm s}$, Ω). The other variables are expressed as a combination of these variables. We consider only gas pressure, $P_{\rm tot} = P_{\rm g} = (\gamma - 1)\Sigma E$, for simplicity. Assuming the

steady accretion flow, the basic equations are represented as follows:

$$\dot{M} = -2\pi r v_r \Sigma, \tag{2.39}$$

$$\frac{1}{r}\frac{d}{dr}\left(r\Sigma v_r^2\right) = -\frac{\partial P_{\rm g}}{\partial r} + \Sigma r\left(\Omega^2 - \Omega_{\rm K}^2\right) - \Omega_{\rm K}\frac{d\Omega_{\rm K}}{dr}\frac{\Sigma H^2}{3}, \tag{2.40}$$

$$\frac{1}{r}\frac{d}{dr}\left(r v_r \Sigma l_z\right) = \frac{1}{r}\frac{d}{dr}\left(r^3\Sigma\nu\frac{d\Omega}{dr}\right), \tag{2.41}$$

$$\frac{1}{r}\frac{d}{dr}\left(r v_r \Sigma E\right) = f_{\rm c}\Sigma\nu\left(r\frac{d\Omega}{dr}\right) - \frac{P_{\rm g}}{rH}\frac{\partial}{\partial r}(rHv_r), \tag{2.42}$$

where $\dot{M}$ is the mass accretion rate and $f_{\rm c}$ is the cooling parameter defined as $Q_{\rm vis} - Q_{\rm cool} = f_{\rm c}Q_{\rm vis}$. In the case of no cooling limit, we have $f_{\rm c} = 1$, while $f_{\rm c} \to 0$ for efficient cooling limit. We search for a solution in which all the variables are power-law function, $X = X_0 r^Y$, assuming the Newtonian gravity $\Omega_{\rm K} = \sqrt{GM_{\rm BH}/r^3} = g_0 r^{-3/2}$. From the dimensional analysis, we find $\Sigma = \Sigma_0 r^{-1/2}$, $v_r = v_0 r^{-1/2}$, $c_{\rm s} = c_0 r^{-1/2}$, and $\Omega = \Omega_0 r^{-3/2}$. After some algebra, we obtain following four equations:

$$\Sigma_0 = -\frac{\dot{M}}{2\pi v_0}, \tag{2.43}$$

$$v_0^2 + 4c_0^2 + 2\Omega_0^2 - 2g_0^2 = 0, \tag{2.44}$$

$$v_0 = -\frac{3\alpha}{2g_0}c_0^2, \tag{2.45}$$

$$-\frac{3}{2}\xi v_0 = \frac{9\alpha}{4g_0}\Omega_0^2, \tag{2.46}$$

where

$$\xi \equiv \frac{5/3 - \gamma}{(\gamma - 1)f_{\rm c}}. \tag{2.47}$$

Solving Equations (2.43) - (2.46), we obtain the solution as follows:

$$\Sigma = -\frac{\dot{M}}{2\pi r v_r} \approx \frac{2(2+\xi)\dot{m}}{6\pi\alpha r v_{\rm K}} \simeq 2.2\times10^{-1}\alpha_{-1}^{-1}\dot{m}_{-2}\varpi_1^{-1/2}\ {\rm g\ cm^{-2}} \tag{2.48}$$

$$v_r = -\frac{2(2+\xi)}{3\alpha}g(\alpha,\xi)v_{\rm K} \approx -\frac{3\alpha}{2(2+\xi)}v_{\rm K} \simeq 3.4\times10^{8}\alpha_{-1}\varpi_1^{-1/2}\ {\rm cm\ s^{-1}} \tag{2.49}$$

$$c_{\rm s} = \frac{2}{3\alpha}\sqrt{(2+\xi)g(\alpha,\xi)}v_{\rm K} \approx \sqrt{\frac{1}{(2+\xi)}}v_{\rm K} \simeq 3.9\times10^{9}\varpi_1^{-1/2}\ {\rm cm\ s^{-1}} \tag{2.50}$$

$$v_\phi = \frac{2}{3\alpha}\sqrt{\xi(2+\xi)g(\alpha,\xi)}v_{\rm K} \approx \sqrt{\frac{\xi}{(2+\xi)}}v_{\rm K} \simeq 3.9\times10^{9}\varpi_1^{-1/2}\ {\rm cm\ s^{-1}}, \tag{2.51}$$

$$g(\alpha,\xi) = \sqrt{1+\frac{9\alpha^2}{2(2+\xi)^2}} - 1, \tag{2.52}$$

where $\dot{m}_{-2} = \dot{m}/0.01$. We approximate with $\alpha^2 \ll 1$ from the second to the third equations, and use $\xi = 1$ from the third to the final equations. To obtain this solution, we need four parameters (α, ξ, $\dot{m}$, and ϖ), which does not include $M_{\rm BH}$. Thus, both AGN and X-ray binaries have the same values of Σ, v_r, v_ϕ, and $c_{\rm s}$. Note that the density $\rho = \Sigma/(2H)$ depends on $M_{\rm BH}$ because $H \simeq c_{\rm s}/\Omega_{\rm K} \propto M_{\rm BH}\varpi$. The physical quantities per unit mass or unit area are independent of $M_{\rm BH}$ while those in unit volume depend on it.

In this power-law solution, $\Sigma \propto \dot{M}$, while v_r, $c_{\rm s}$, and v_ϕ are independent of $\dot{M}$. In the limit of $\alpha^2 \ll 1$, the radial velocity is related to α but $c_{\rm s}$ and v_ϕ are independent of α. The sound velocity and angular velocity are only related to ξ that is determined by the cooling efficiency and specific heat ratio. For $\xi \sim 1$, we can give an order-estimate as $v_\phi \sim v_{\rm K}$, $c_{\rm s} \sim v_{\rm K}$, and $v_r \sim \alpha v_{\rm K}$. This means that large fraction of the released energy is used to heat the materials, and this internal energy of the gas falls into the black hole without energy loss by radiation.

For $\gamma = 5/3$, we have $\xi = 0$, therefore this solution has no angular momentum $v_\phi = 0$. In this case, the relation of Equation (2.45) is no longer meaningful, and we can get another solution from (2.39) and (2.40) with the adiabatic condition $p_{\rm g} = K\rho^\gamma$. If we consider efficient cooling flows $\xi \gg 1$, the solution satisfies the Keplerian rotation $v_\phi \simeq v_{\rm K}$ and the relation $v_r \ll c_{\rm s} \ll v_{\rm K}$. Although this solution has similar features to the SSDs, this solution is

different from SSDs because they have different parameter dependences.

In this power-law solution, the Bernoulli constant,

$$\mathrm{Be} = \frac{1}{2}(v_r^2 + v_\phi^2) + \frac{\gamma}{\gamma - 1}c_\mathrm{s}^2 - \Omega_\mathrm{K}^2 r^2, \tag{2.53}$$

is usually positive. After some algebra, the condition $\mathrm{Be} > 0$ is rewritten as

$$f_\mathrm{c} > \frac{5/3 - \gamma}{2(2 - \gamma)} \tag{2.54}$$

If we consider the usual range of specific heat ratio as $1 < \gamma < 5/3$, Be is positive when $f_\mathrm{c} > 1/3$. Positive Be means that the flow has positive energy, implying that the flow is not bounded by the black hole. This leads to a consideration that the hot accretion flows are related to the outflows. Some models including the disk wind are proposed (e.g., Blandford & Begelman 1999), which is another sub-class of RIAFs. However, we note the fact that positive Be does not always imply outflows. For example, Bondi accretion flow, which is a solution of spherically symmetric accretion, also has the positive Be but few consider that the Bondi accretion causes outflows.

We see that the power-law solution is sub-sonic everywhere. In reality, the flows are likely to be supersonic at the vicinity of the black holes because of the strong gravity. In late 1990s, some researchers studied the global structures of the hot accretion flows (e.g., Chen et al. 1997; Manmoto et al. 1997; Nakamura et al. 1997; Narayan et al. 1997), using the pseudo-Newtonian potential (Equation [2.7]). They obtained the transonic solutions and found that the basic pictures of the global solutions are consistent with those of the power-law solution. Narayan et al. (1997) showed that the global solutions match the power-law solution well except for the region close to the inner and outer boundaries. In the global solutions, the parameter dependences of v_r, c_s, v_ϕ, and Σ are also consistent with those of the power-law solution described in Equation (2.48) - (2.51) (see also Chen et al. 1997; Nakamura et al. 1997).

2.4 Timescales of hot accretion flows

There are several timescales to evaluate the physical conditions. Here, we estimate some timescales for the power-law solution with $\xi = 1$, and discuss the physical conditions of RIAFs. For the alpha prescription, the dissipation time is estimated to be

$$t_{\rm dis} \sim \frac{1}{\alpha\Omega} \sim 7.5 \times 10^4 \varpi_1^{3/2} \alpha_{-1}^{-1} M_{\rm BH,7} \ [\rm sec]. \tag{2.55}$$

In the advection dominated accretion flow, infall time is estimated to be

$$t_{\rm fall} \sim \frac{r}{v_r} \sim \frac{2}{\alpha\Omega_{\rm K}} \sim 8.8 \times 10^4 \varpi_1^{3/2} \alpha_{-1}^{-1} M_{\rm BH,7} \ [\rm sec]. \tag{2.56}$$

Thus, the infall time is always the same order with the dissipation time, $t_{\rm fall} \sim t_{\rm dis}$. This means that the thermal energy generated by viscous dissipation can be carried by advection.

If the proton-proton relaxation time $t_{pp,\rm rel}$ in plasma is longer than the dissipation time, non-thermal particles are likely to exist inside the plasma (Takahara & Kusunose 1985; Mahadevan & Quataert 1997). We define the flows that satisfy $t_{pp,\rm rel} > t_{\rm fall}$ as the collisionless flows. The proton-proton relaxation time is estimated to be

$$\begin{aligned} t_{pp,\rm rel} &= \frac{4\sqrt{\pi}}{\ln\Lambda} \frac{1}{n_p \sigma_{\rm T} c} \left(\frac{m_p}{m_e}\right)^2 \left(\frac{k_{\rm B} T_p}{m_p c^2}\right)^{3/2} \\ &\sim 2.2 \times 10^7 \alpha_{-1} M_{\rm BH,7} \dot{m}_{-2}^{-1} \ [\rm sec], \end{aligned} \tag{2.57}$$

where $\ln\Lambda = \ln(4\pi\lambda_{\rm D}^3 n_e/3)$ is the Coulomb logarithm ($\lambda_{\rm D}$ is the Debye length). We use $k_{\rm B} T_p \sim m_p c_{\rm s}^2 \sim m_p v_{\rm K}^2/3$ and $\ln\Lambda = 30$. We find $t_{pp,\rm rel} \gg t_{\rm fall} \sim t_{\rm dis}$ in RIAFs, which means that protons cannot become Maxwellian by Coulomb scattering within the infall time. This motivates us to consider non-thermal particles in RIAFs.

The proton-electron relaxation time is estimated to be (Stepney 1983; Takahara & Kusunose 1985)

$$t_{pe,\rm rel} = \frac{2}{\ln\Lambda} \frac{1}{n_p \sigma_{\rm T} c} \left(\frac{m_p}{m_e}\right) \left(\frac{k_{\rm B} T_e}{m_e c^2}\right), \tag{2.58}$$

where we assume that electrons are relativistic and protons are non-relativistic. This timescale depends on the electron temperature. If we assume $T_e = T_p$, we have $t_{pe,\rm rel} > t_{pp,\rm rel} \gg t_{\rm fall}$, so

that the protons cannot give the energy to electrons through Coulomb interaction. This means the electron temperature is different from the proton temperature. Even for $k_{\rm B}T_e \sim m_e c^2$, we find that $t_{pe,\rm rel} \sim 1.6 \times 10^6$ sec $\gg t_{\rm fall}$. Thus, protons cannot cool down by the Coulomb collisions if electrons are relativistic. Note that when $T_e \ll T_p$, electron heating time by Coulomb collisions, $t_{e,\rm Coul}$, is shorter than the proton-electron relaxation time as $t_{ep,\rm Coul} \sim t_{pe,\rm rel}(T_e/T_p)$. This is because $t_{pe,\rm rel}$ is defined as $t_{pe,\rm rel} = |T_e - T_p|/|dT_e/dt|$ (Stepney 1983; Takahara & Kusunose 1985). When $k_{\rm B}T_e \sim m_e c^2$, $t_{e,\rm Coul} \sim (T_e/T_p)t_{pe,\rm rel} \simeq 5.3 \times 10^4$ sec, which is comparable to the infall time. Thus, it is possible to heat up electrons to the relativistic temperature through Coulomb collisions when $\dot{m} \gtrsim 0.01$, although the radiation from thermal electrons is probably important in this situation.

The electron-electron relaxation time is estimated to be (Stepney 1983; Takahara & Kusunose 1985)

$$t_{ee,\rm rel} = \frac{8}{\ln\Lambda}\frac{1}{n_p\sigma_{\rm T}c}\left(\frac{k_{\rm B}T_e}{m_e c^2}\right)^2 \sim 3.4 \times 10^3 \varpi_1^{3/2}\alpha_{-1}M_{\rm BH,7}\dot{m}_{-2}^{-1}\theta_e^2 \ [\rm sec],$$

where we assume the electrons are relativistic, and $\theta_e = k_{\rm B}T_e/(m_e c^2)$. The electron-electron relaxation time is shorter than $t_{\rm fall}$. Note that synchrotron self absorption mechanism is more efficient than the Coulomb interaction in RIAFs, so that the electrons are likely to be Maxwellian for $\dot{m} \gtrsim 10^{-4}$ (Mahadevan & Quataert 1997).

2.5 Plasma processes in hot accretion flows

In RIAFs, protons are collisionless and there may be non-thermal particles. This means the plasma inside RIAFs are no longer usual fluids. Inefficient Coulomb collision allows protons to have anisotropic pressure, which affects the growth rate of MRI (Quataert et al. 2002; Sharma et al. 2006). Thus, it is not obvious whether MRI works as a mechanism of the angular momentum transport as is the case with usual MHD. MRI in RIAFs is investigated with the anisotropic pressure by the formalism so called the "kinetic MHD," in which pressure is divided into the parallel component ($p_\parallel$) and the perpendicular component ($p_\perp$) with respect

to the magnetic fields. Under this formalism, $p_\perp$ becomes higher as the magnetic fields become stronger owing to the adiabatic invariance of $p_\perp/B$. The high $p_\perp$ makes the magnetic fields stiffer than those in MHD. This makes the shortest wavelength of unstable modes for MRI longer, which leads to stabilizing whole part of the accretion flow against MRI. Sharma et al. (2006) show that the pressure anisotropy suppresses the growth of MRI, using the kinetic MHD simulation with shearing box approximation. Some isotropization mechanism is necessary in order to observe the non-linear growth of MRI under the kinetic MHD.

The strong pressure anisotropy induces another instability, such as the mirror instability (for $p_\perp > p_\parallel$) or the fire-hose instability (for $p_\perp < p_\parallel$). These instabilities generate small scale waves, and these waves make the particle distribution isotropic through the pitch-angle scattering (e.g., Gary et al. 1997). Hoshino (2013) showed that the mirror modes decrease the pressure anisotropy enough to reproduce the non-linear growth of MRI (see Figure 2.1), using particle-in-cell (PIC) simulations with the shearing box approximation (see also Riquelme et al. 2012). Therefore, MRI is likely to play an important role in the angular momentum transport even in the collisionless accretion flows.

The electrons in RIAFs are expected to heat up by plasma processes such as magnetic reconnection or wave-particle interaction. These electron heating mechanisms are related to the dissipation process within the plasma scale, while the magnetic turbulence is induced by the shear motion from the hydrodynamical scale. Both the plasma processes and hydrodynamical processes are important to understand the electron heating in RIAFs. However, we cannot solve these processes simultaneously with realistic parameters because the size of these scales are different by more than 10 orders of magnitude. Although some studied about the electron heating in RIAFs (Quataert & Gruzinov 1999; Sharma et al. 2007; Sironi 2014; Sironi & Narayan 2014), we are far from the understanding of the electron heating. In this thesis, we avoid getting involved this problem and treat $\theta_e = k_{\rm B}T_e/(m_e c^2)$ as a parameter. We consider the range of electron temperature $1 \lesssim \theta_e \lesssim 4$ following Sharma et al. (2007).

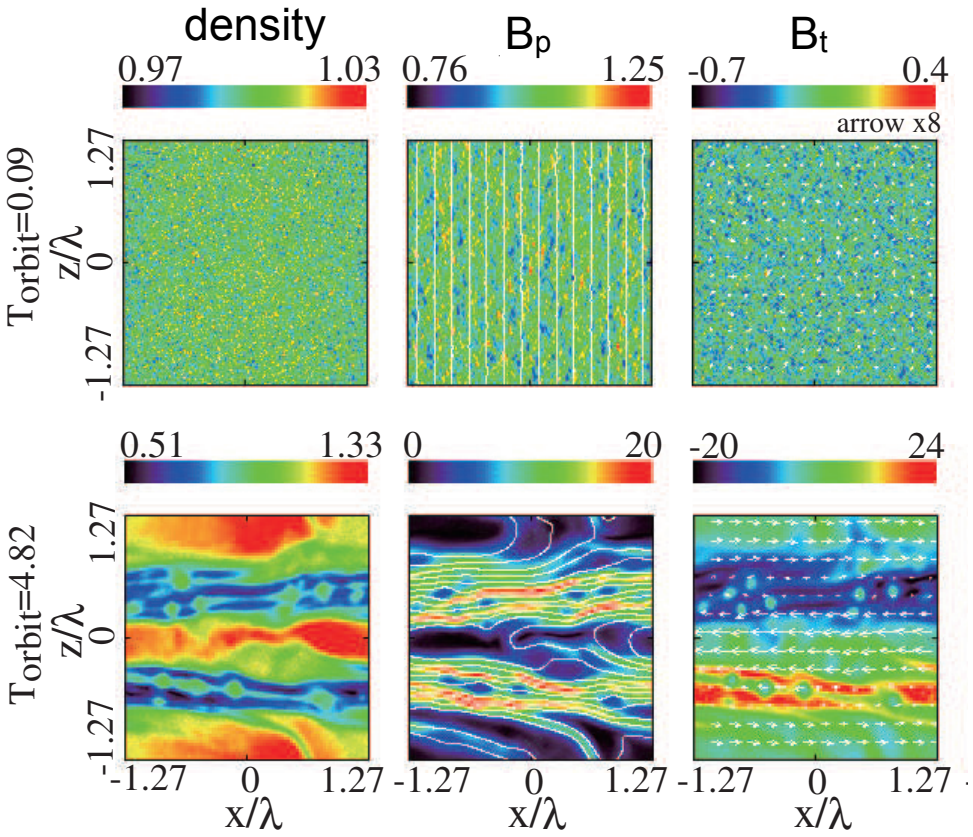

Figure 2.1: The non-linear growth of MRI as a result of 2D PIC simulation in xz plane. This figure is reproduced from Hoshino (2013), by permission of the American Astronomical Society. The upper and lower panels show the initial and non-linear growth phases, respectively. The left, middle right panels are the plasma density, the strength of poloidal magnetic fields, and the strength of toroidal magnetic fields, respectively. The white lines in the middle panels represent the the direction of the poloidal magnetic fields. The white arrows in the right panels represent the plasma velocity projected in xz plane. The coordinates x and z are normalized by $\lambda = 2\pi v_A/\Omega_0$.

2.6 Non-thermal particles in hot accretion flows

Theoretically, it is expected that the magnetic reconnection of turbulent fields generates the non-thermal particles (Riquelme et al. 2012; Hoshino 2013). However, PIC simulations follow the plasma scale that is much smaller than the dynamical scale. The non-thermal particles generated by the magnetic reconnection is expected to experience the stochastic acceleration through the turbulent magnetic fields. This process is likely to produce the non-thermal protons in the bulk of RIAFs (e.g., Lynn et al. 2014). These accelerated protons produce neutrons, neutrinos, electrons, and positrons through interactions with thermal protons and photons (see Chapter 1). These neutrinos are able to escape from the flow. The gamma rays can be absorbed by the background photon fields through the pair production process

$$\gamma + \gamma \rightarrow e^+ + e^-. \tag{2.59}$$

The generated electrons and positrons can cool down rapidly through the synchrotron process. Thus, the accretion flows lose all of the energy expended to produce the pions. The non-thermal protons can also escape from the flow by diffusive motion while thermal protons are confined by the strong turbulent magnetic fields. This is because the mean free path of the protons is longer for a higher protons energy. In addition, the non-thermal neutrons are able to escape owing to their charge neutrality and long lifetime. Therefore, the non-thermal protons seem to act as a coolant of the flow, which may affect the dynamical structure of the accretion flows (see Chapter 3). They emit the high-energy protons, neutrinos, and gamma rays. Thus, RIAFs are a candidate of the source of cosmic rays and neutrinos (see Chapter 4).

There are some observational implications from the existence of non-thermal particles in RIAFs. The center of our Galaxy, Sgr A*, is considered to be a RIAF onto a SMBH, and we observe the photons from radio to X-ray from the galactic center. Figure 2.2 shows that RIAF models with non-thermal electrons (Yuan et al. 2003) can explain the data of Sgr A* better than that without non-thermal electron (Narayan et al. 1995; Manmoto et al. 1997). In addition, GeV - TeV gamma rays are detected from the galactic center (Aharonian et

al. 2009a; Chernyakova et al. 2011). It is natural to consider that particles accelerated at the vicinity of the black hole emit these gamma rays. Both leptonic models (Kusunose & Takahara 2012) and hadronic models (Liu et al. 2006; Chernyakova et al. 2011) can explain the gamma rays, and the origin is still controversial. GeV gamma rays are also detected from a few galactic X-ray binaries (Bodaghee et al. 2013) and LLAGNs (Abdo et al. 2009; Sahakyan et al. 2013). Although many consider that the jets associated with these objects are relevant to these gamma rays (Malyshev et al. 2013), it may be possible that these gamma rays come from the accreting materials (Kadowaki et al. 2014). These gamma rays might be evidence of non-thermal particles in the vicinity of black holes.

2.7 Relativistic jets and hot accretion flows

Radio observations reveal that some AGNs have relativistic jets. These observations suggest that the Lorentz factors of the jets are typically $\Gamma \sim 10 - 100$, and that their luminosities are broadly distributed over $L_{\rm jet} \lesssim \dot{M}c^2$ (Fernandes et al. 2011; Punsly & Zhang 2011).

ADAF is also considered to be related to the formation of outflows and relativistic jets (Narayan & Yi 1994). However, the production mechanism of the jets is not well understood. If the luminosity of the jet, $L_{\rm jet}$, originates from the gravitational energy of the accreting materials, the condition $L_{\rm jet} < \eta \dot{M}c^2$ should be satisfied, where $\dot{M}$ is the mass accretion rate onto a SMBH and η is the energy release efficiency. Since $L_{\rm jet} = \Gamma \dot{M}_{\rm jet} c^2$, where $\Gamma \sim 10 - 100$ is the Lorentz factor of the jet and $\dot{M}_{\rm jet}$ is the mass loading rate of the jet, we have $\dot{M}_{\rm jet} \ll \dot{M}$. This means that some mechanisms concentrating the gravitational energy on a small fraction of the materials are necessary. The escape of the high-energy particles may be one of the mechanisms (e.g., Le & Becker 2004; Becker et al. 2008; Toma & Takahara 2012).

It is likely that the gravitational energy is converted to Poynting and/or kinetic energies and they are injected into the polar region above the SMBH, "the funnel," where the gas is very dilute due to the centrifugal barrier. The most actively discussed model is the magnetically

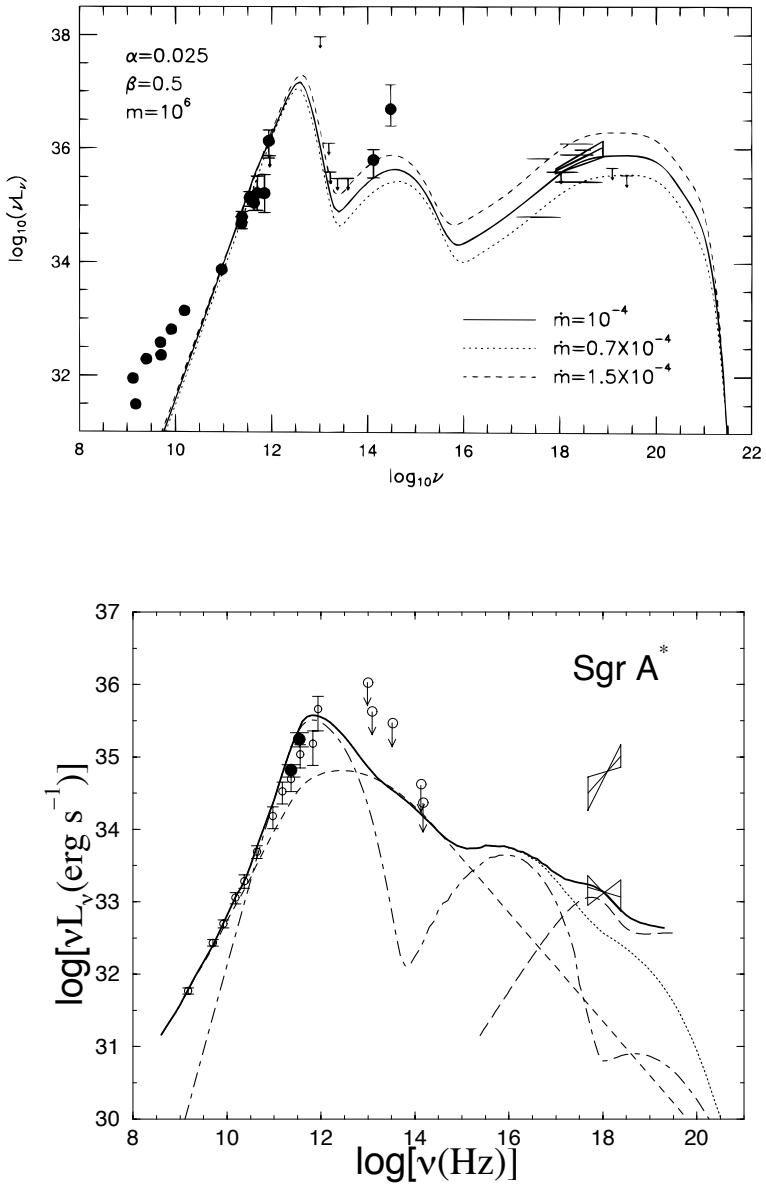

Figure 2.2: The observed SED from Sgr A* and fittings by the hot accretion flow models. *top panel*: The spectrum of a model without non-thermal electrons. This figure is reproduced from Manmoto et al. (1997), by permission of the American Astronomical Society. This model can fit the data well except in the radio band. *bottom panel*: The spectrum of a model with non-thermal electrons. This figure is reproduced from Yuan et al. (2003), by permission of the American Astronomical Society. The data in the radio band can be fitted by the synchrotron emission from non-thermal electrons.

driven jet model investigated by magnetohydrodynamic simulations (McKinney 2006; Komissarov et al. 2007). The electromagnetic force accelerates the flow to relativistic speed, and it is considered that the amount of mass injected in the funnel determines the terminal Lorentz factor. An alternative idea is the kinetically dominated jet model, in which the relativistic thermal energy (i.e., random kinetic energy of particles) is transferred to the acceleration of the bulk flow (Asano & Takahara 2007; Becker et al. 2011). In this model, the terminal Lorentz factor is roughly equal to the average random Lorentz factor of particles. The escaping particles from the accretion flows seem to be related to the energy injection of the kinetically dominated jet model. Thus, it is important to estimate the luminosity of escaping particles from the flow.

Chapter 3

Effects of High-energy Particles on Dynamical Structure

As we see in Chapter 2, hot accretion flows are collisionless ($t_{pp,\mathrm{rel}} \gg t_{\mathrm{fall}}$), in which non-thermal protons may exist. These protons are expected to extract some amount of energy from the flow. They also modify the total pressure because of the different specific heat ratio. Thus, they may affect the dynamical structure of the accretion flows. In this chapter, we see how non-thermal particles affect the dynamical structure of the flow. We formulate the accretion flows including feedback from the non-thermal particles in Section 3.1, and show the steady state solutions and luminosity of escaping particles in Section 3.2. We discuss the implications of escaping particles on relativistic jet production and ignored process in Section 3.3. We summarize the results of this chapter in Section 3.4 This chapter is based on Kimura et al. (2014a).

3.1 Formulation

We consider a steady accretion flow that consists of thermal and non-thermal particles with the assumption that non-thermal particles are high-energy enough to be relativistic. The

thermal particles (TPs) obey the fluid equations, while the high-energy particles (HEPs) are described by the diffusion-convection equation (e.g., Drury 1983; Jones 1990). We assume that the radiation from TPs is inefficient and ignore effects of the electron component. We also assume that the bulk velocity of HEPs is the same with that of TPs due to the coupling between HEPs and TPs through the magnetic fields.

3.1.1 Thermal component

For TPs, we use the same procedure as Chapter 2. Here, we use the pseudo-Newtonian potential represented as

$$\Phi = -\frac{GM}{\sqrt{r^2+z^2}-R_{\rm S}}, \tag{3.1}$$

in which the Keplerian angular velocity is described as

$$\Omega_{\rm K} = \sqrt{\frac{GM}{r}}\frac{1}{r-R_{\rm S}}. \tag{3.2}$$

We write the total pressure $p_{\rm tot} = p_{\rm TP} + p_{\rm HEP} + p_B$, where we introduce the pressure by HEPs $p_{\rm HEP}$ and magnetic pressure p_B.

The basic equations for TPs are represented as

$$\frac{\partial \Sigma}{\partial t} + \frac{1}{r}\frac{\partial}{\partial r}(r\Sigma v_r) = 0, \tag{3.3}$$

$$\frac{\partial}{\partial t}(\Sigma l_z) + \frac{1}{r}\frac{\partial}{\partial r}(r v_r \Sigma l_z) = \frac{1}{r}\frac{\partial}{\partial r}\left(r^3 \Sigma \nu \frac{\partial \Omega}{\partial r}\right), \tag{3.4}$$

$$\frac{\partial}{\partial t}(\Sigma v_r) + \frac{1}{r}\frac{\partial}{\partial r}(r\Sigma v_r^2) = -\frac{\partial P_{\rm tot}}{\partial r} + \Sigma r(\Omega^2 - \Omega_{\rm K}^2) - \Omega_{\rm K}\frac{d\Omega_{\rm K}}{dr}\frac{\Sigma H^2}{3}, \tag{3.5}$$

$$\frac{\partial}{\partial t}(\Sigma E_{\rm TP}) + \frac{1}{r}\frac{\partial}{\partial r}\left(r v_r \Sigma E_{\rm TP}\right) = Q_+, \tag{3.6}$$

$$P_{\rm TP} = (\gamma_{\rm TP} - 1)\Sigma E_{\rm TP}, \tag{3.7}$$

where $P_{\rm tot} = \int p_{\rm tot} dz = P_{\rm TP} + P_{\rm HEP} + P_B$ ($P_{\rm HEP} = \int p_{\rm HEP} dz$ and $P_B = \int p_B dz$), and Q_+ is the total heating rate that includes the viscous dissipation and the compressional heating. The subscript TP indicates the variables for TPs. We assume that the inertia of TPs is much higher

than that of HEPs. This assumption allows us to write Equations (3.3) and (3.4) without any sink terms due to interchange between TP and HEP. We set $\gamma_{\rm TP} = 5/3$ because TPs are assumed to be non-relativistic.

We assume turbulent magnetic fields induced by TPs in the accretion flows. The integrated magnetic pressure P_B is estimated with the assumption that the plasma beta is constant, i.e

$$P_B = P_{\rm TP}/\beta. \tag{3.8}$$

Some previous studies consider that magnetic fields behave as a relativistic gas and include the magnetic component in their energy equation (e.g., Esin et al. 1997). However, since we hardly understand a proper description of magnetic fields, we simply assume that magnetic pressure is proportional to the thermal pressure and do not include the magnetic component in the energy equation. The vertically averaged strength of the magnetic fields B is defined as

$$B = \sqrt{8\pi p_B} = \sqrt{4\pi P_B/H}, \tag{3.9}$$

where we use $P_B = \int p_B dz = 2Hp_B$ and $p_B = B^2/(8\pi)$. Under this assumption, the magnetic fields do not behave as a relativistic gas. We assume B is constant in the vertical direction.

3.1.2 High-energy component

In this chapter, we assume that HEPs are relativistic and regard their energy and momentum are equal. HEPs obey the diffusion convection equation (e.g., Drury 1983; Jones 1990)

$$\frac{\partial F}{\partial t} + \boldsymbol{v}\cdot\boldsymbol{\nabla}F = \boldsymbol{\nabla}\cdot(\kappa_p\boldsymbol{\nabla}F) + \frac{\boldsymbol{\nabla}\cdot\boldsymbol{v}}{3}p\frac{\partial F}{\partial p} + \dot{F}_{\rm inj} - \dot{F}_{\rm sink}, \tag{3.10}$$

where $F(t, \mathbf{r}, p)$ is the distribution function of HEPs, κ_p is the diffusion coefficient, and p is the momentum of HEPs. We add the terms $\dot{F}_{\rm inj}$ and $\dot{F}_{\rm sink}$ that describe the injection and sink, respectively. The sink term, added in this equation symbolically, includes the effects of neutron escape and pion production. We assume that the magnetic reconnection and/or the stochastic acceleration act as the injection term.

As a first step, instead of solving the distribution function F, we only solve the number and energy densities, $N_{\rm HEP}$ and $U_{\rm HEP}$, in this chapter. We define the number density and the energy density of HEPs per unit area as

$$N_{\rm HEP} = 4\pi \int_{-\infty}^{\infty} dz \int_{0}^{\infty} dp p^2 F, \tag{3.11}$$

$$U_{\rm HEP} = 4\pi \int_{-\infty}^{\infty} dz \int_{0}^{\infty} dp p^2 F pc, \tag{3.12}$$

respectively. We can treat the mean Lorentz factor as

$$\gamma_{\rm m} \equiv \frac{U_{\rm HEP}}{m_{\rm p} c^2 N_{\rm HEP}}, \tag{3.13}$$

where $m_{\rm p}$ is the proton mass. Taking the appropriate moments of Equation (3.10) and integrating over the vertical direction, we obtain the equations of number and energy densities of HEPs as

$$\frac{\partial N_{\rm HEP}}{\partial t} + \frac{1}{r}\frac{\partial}{\partial r}(r v_r N_{\rm HEP}) = \frac{1}{r}\frac{\partial}{\partial r}\left(r\kappa \frac{\partial N_{\rm HEP}}{\partial r}\right) - \dot{N}_{\rm diff} + \dot{N}_{\rm inj} - \dot{N}_{\rm sink}, \tag{3.14}$$

$$\frac{\partial U_{\rm HEP}}{\partial t} + \frac{1}{r}\frac{\partial}{\partial r}(r v_r U_{\rm HEP}) = Q_{\rm V,HEP} + \frac{1}{r}\frac{\partial}{\partial r}\left(r\kappa \frac{\partial U_{\rm HEP}}{\partial r}\right) - Q_{\rm diff} + Q_{\rm inj} - Q_{\rm sink}, \tag{3.15}$$

respectively. We have used the averaged diffusion coefficient κ, the injection terms $\dot{N}_{\rm inj}$ and $Q_{\rm inj}$, the sink terms $\dot{N}_{\rm sink}$ and $Q_{\rm sink}$, and the escaping rates of HEPs through vertical diffusion $\dot{N}_{\rm diff} = N_{\rm HEP}/t_{p,\rm esc}$ and $Q_{\rm diff} = U_{\rm HEP}/t_{p,\rm esc}$, where $t_{p,\rm esc} = H^2/\kappa$ is the vertical diffusion time. Equation (3.15) has the compressional heating term

$$Q_{\rm V,HEP} = -\frac{P_{\rm HEP}}{rH}\frac{\partial}{\partial r}(rHv_r), \tag{3.16}$$

where we define the integrated pressure of HEPs as

$$P_{\rm HEP} = 4\pi \int_{-\infty}^{\infty} dz \int_{0}^{\infty} dp p^2 F \frac{cp}{3}. \tag{3.17}$$

We assume that mean velocity of HEPs are the same with that of TPs, so that we can write the compressional heating term as Equation (3.16) (see Equation [2.20]). We also assume that HEPs are relativistic and write the relation between $U_{\rm HEP}$ and $P_{\rm HEP}$ as

$$U_{\rm HEP} = 3P_{\rm HEP}. \tag{3.18}$$

This relation implies that $\gamma_{\rm HEP} = 4/3$, where $\gamma_{\rm HEP}$ is the specific heat ratio of HEPs. We describe κ as

$$\kappa = \frac{1}{3} c\lambda = \frac{C_{\rm diff} c r_{\rm g}}{3}. \tag{3.19}$$

We represent the mean-free path as $\lambda = C_{\rm diff} r_{\rm g}$, where $C_{\rm diff}$ is a parameter that represents difference from the Bohm diffusion, and $r_{\rm g} = \gamma_{\rm m} m_{\rm p} c^2/(eB)$ is the gyro radius. In the actual situation, the diffusion coefficient depends on the Lorentz factor of the particles because the particles with higher energies have longer mean free paths. As a first step study, however, we do not treat the spectrum of HEPs but simplify the situation by taking the moments of the distribution function F. In the same spirit, we use $\gamma_{\rm m}$ when we estimate $r_{\rm g}$.

The electrons have much smaller mean free path than the protons, so that the electrons are unlikely to escape as efficiently as protons. Since the surrounding materials are also ionized, some charged particles may be supplied to the accretion flow to maintain the charge neutrality. We ignore this effect because the number flux of escaping protons are quite low, compared to that of accreting ones.

3.1.3 Energy dissipation and energy loss

HEPs affect the dynamical structure of the flow through the pressure term and energy extraction. In this section, we summarize the internal energy injected into or extracted from the accretion flows. In this chapter, we assume that the rates of injection into HEPs are related to the heating rates of TPs. TPs are heated by the viscous dissipation rates,

$$Q_{\rm vis} = \Sigma \nu \left(r \frac{\partial \Omega}{\partial r} \right)^2, \tag{3.20}$$

and the compressional heating rates,

$$Q_{\rm V,TP} = -\frac{P_{\rm TP}}{rH} \frac{\partial}{\partial r} (rHv_r). \tag{3.21}$$

See Chapter 2 for derivation of Equation (3.21). Since the turbulent viscosity is expected to induce the dissipation in the accretion flows, it is considered that some fraction of the dissipated

power is expended to inject HEPs by the second-order Fermi acceleration. The compression of the turbulent magnetic fields is likely to induce the magnetic reconnection, so that HEPs are expected to be generated by consuming some fraction of the compressional heating energy. Thus, we assume that the fraction $f_{\rm vis}$ of $Q_{\rm vis}$ is injected into HEPs, and the remaining fraction $(1 - f_{\rm vis})$ goes into TPs. Similarly, the fraction $f_{\rm comp}$ of $Q_{\rm V,TP}$ goes into HEPs, and the other $(1 - f_{\rm comp})$ heats up TPs, i.e.,

$$Q_{\rm inj} = f_{\rm vis} Q_{\rm vis} + f_{\rm comp} Q_{\rm V,TP} \tag{3.22}$$

and

$$Q_{+} = (1 - f_{\rm vis}) Q_{\rm vis} + (1 - f_{\rm comp}) Q_{\rm V,TP}. \tag{3.23}$$

As described above, we ignore the spectrum of HEPs and only use the mean Lorentz factor. In the same manner, we assume mono-energetic injection everywhere. Using the Lorentz factor at injection, $\gamma_{\rm inj}$, the injection term for the number density of HEPs is represented as

$$\dot{N}_{\rm inj} = \frac{Q_{\rm inj}}{(\gamma_{\rm inj} - 1) m_{\rm p} c^2}. \tag{3.24}$$

The interactions between HEPs and TPs extract the energy and particles from the flow. Since we ignore the radiation processes of TPs, we do not consider the background photon fields. This treatment allows us to neglect photomeson production, $p\gamma \to p\pi^0$ or $n\pi^+$, and consider only proton-proton inelastic collisions (pp collisions). When the pp collisions (1.2) occur, pions are produced, and high-energy protons or neutrons lose their energies. The pions decay into photons, neutrinos, electrons, and positrons as Equations (1.4) - (1.6) (Begelman et al. 1990). Since we consider tenuous accretion flows with the optical depth for electron scattering $\tau_{\rm es} \lesssim 1$, the neutrinos and photons may escape directly from the flows, and the high-energy electrons and positrons are considered to emit radiation and lose their energy rapidly. Thus, the flows lose their energy by pion production through the pp collisions. Using the inelasticity of this reaction, K_π, we estimate the energy loss rates by pion production as

$$Q_\pi = \int K_\pi \epsilon_{\rm kin} n_{\rm HEP} n_{\rm TP} \sigma_{pp} c dz = \frac{K_\pi \epsilon_{\rm kin} N_{\rm HEP} \Sigma \sigma_{pp} c}{2 m_{\rm p} H}, \tag{3.25}$$

where $n_{\rm HEP} = N_{\rm HEP}/(2H)$ is the number density of HEPs, $n_{\rm TP} = \Sigma/(2m_{\rm p}H)$ is the number density of the TPs, $\epsilon_{\rm kin} = (\gamma_{\rm m} - 1)m_{\rm p}c^2$ is the mean kinetic energy of HEPs, and

$$\sigma_{pp} = 30\left[0.95 + 0.06\ln\left(\frac{\epsilon_{\rm kin}}{1{\rm GeV}}\right)\right]{\rm mb} \tag{3.26}$$

is the cross section for *pp* collisions (Aharonian & Atoyan 2000). We assume that the number density of HEPs is uniform for the vertical direction when estimating the *pp* collision rate.

Neutrons are also produced by *pp* collisions. The formation rates of relativistic neutrons in unit volume are estimated as

$$\dot{n}_{\rm p\to n} = \frac{1}{2}P_{\rm p\to n}n_{\rm HEP}n_{\rm TP}\sigma_{\rm pp}c, \tag{3.27}$$

where $P_{\rm p\to n}$ is the probability of neutron formation per interaction. The factor 1/2 indicates that half of the neutrons are thermal. Neutrons may escape from the flows because of the charge neutrality, whereas neutrons decay into the protons when their lifetime has passed after their formation. For a neutron to escape from the flow, its escape time $t_{n,\rm esc}$ has to be shorter than its lifetime $t_n = 887\gamma_{\rm n}$sec, where $\gamma_{\rm n}$ is the Lorentz factor of the escaping neutron. Ignoring escape of thermal neutrons from the flows since most of thermal neutrons satisfy $t_n \ll t_{n,\rm esc}$, we write the neutron escape rates as

$$\dot{N}_{\rm esc} = \int \dot{n}_{\rm p\to n}\exp\left(-\frac{t_{n,\rm esc}}{t_n}\right)dz. \tag{3.28}$$

With the approximation that all neutrons move along the vertical direction, we write the escaping time as $t_{n,\rm esc} = (H - z)/c$, and the neutron escape rates are evaluated as

$$\dot{N}_{\rm esc} = \dot{n}_{\rm p\to n}ct_n\left\{1 - \exp\left(-\frac{2H}{ct_n}\right)\right\}. \tag{3.29}$$

On neutron production, some fraction of energy is carried away by pions, and the Lorentz factor of escaping neutrons satisfies the condition of

$$(\gamma_{\rm n} - 1)m_{\rm n}c^2 = (1 - K_\pi)(\gamma_{\rm m} - 1)m_{\rm p}c^2, \tag{3.30}$$

where $m_{\rm n}$ is the mass of a neutron. We can neglect the interactions of neutrons with TPs because we consider tenuous flows (Begelman et al. 1990; Toma & Takahara 2012). Using $\gamma_{\rm n}$, we represent the energy loss rates by neutron escape as

$$Q_{\rm esc} = (\gamma_{\rm n} - 1) m_{\rm n} c^2 \dot{N}_{\rm esc}. \tag{3.31}$$

The sink term of Equation (3.14) is equivalent to neutron escape,

$$\dot{N}_{\rm sink} = \dot{N}_{\rm esc}. \tag{3.32}$$

On the other hand, $Q_{\rm sink}$ in Equation (3.15) includes the cooling by pion production in addition to neutron escape,

$$Q_{\rm sink} = Q_{\rm esc} + Q_{\pi}. \tag{3.33}$$

We set $K_{\pi} = 0.5$ and $P_{\rm p\to n} = 0.5$ following Begelman et al. (1990).

3.1.4 Calculation method and conditions

We solve the six differential Equations (3.3), (3.4), (3.5), (3.6), (3.14), and (3.15) for Σ, l_z, v_r, $E_{\rm TP}$, $N_{\rm HEP}$, and $U_{\rm HEP}$. We calculate the time evolution of these equations until a steady state solution is realized rather than solve the equations with steady assumption because the former method has some advantages over the latter. One of the advantages is that we need not treat the singular point arising in the steady state flow equations. Another advantage is that unstable solutions are not realized. In order to solve the fluid equations, we use a method of finite differences with a time-explicit solution procedure similar in methodology to the ZEUS code with the von Neumann & Richtmyer artificial viscosity (von Neumann & Richtmyer 1950; Stone & Norman 1992). See Appendix B for the test calculations of fluid equations. The equations of HEPs are solved by using the fully implicit method (Press et al. 1992). We determine the time step such that the CFL condition is safely satisfied (the safety factor $C_0 = 0.1$). The number of the grid points is $N = 256$, and the grids are uniformly

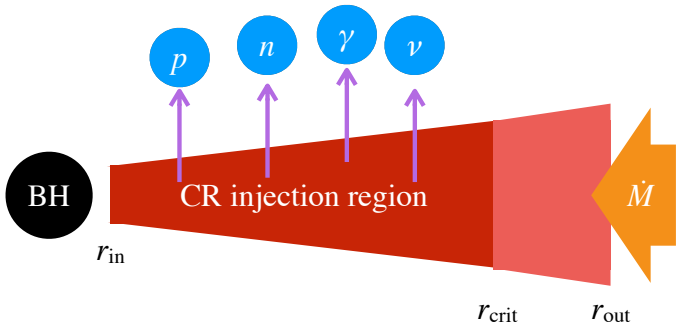

Figure 3.1: The schematic picture of our model. The protons are accelerated in RIAFs within the critical radius, and interact with the thermal protons. Then, the non-thermal neutrons, neutrinos, and gamma rays are generated and escape from the flow. The non-thermal protons can also escape from the flows directly.

divided in the logarithmic space. We calculate some models with $N = 128$ and find that the results are unchanged by the number of grids.

The initial conditions are unimportant because the system forgets them by the time when

a steady state solution is realized. We set the initial conditions as follows:

$$\Sigma = -\frac{\dot{M}}{2\pi r v_r}, \tag{3.34}$$
$$l_z = 0.9\Omega_{\rm K} r^2, \tag{3.35}$$
$$v_r = v_{r,0} r^{-1}, \tag{3.36}$$
$$E_{\rm TP} = -0.5\Phi, \tag{3.37}$$
$$N_{\rm HEP} = 0.0, \tag{3.38}$$
$$U_{\rm HEP} = 0.0, \tag{3.39}$$

where $\dot{M}$ is the mass accretion rates, and $v_{r,0}$ is determined to be smoothly connected at the outer boundary. The boundary conditions do not strongly affect the solutions when we choose sufficiently large $r_{\rm out}$. We assume that there is a rotationally supported flow at the outer boundary $r = r_{\rm out}$, i.e., we set the outer boundary of TPs as

$$\Sigma = -\frac{\dot{M}}{2\pi r v_r}, \tag{3.40}$$
$$l_z = 0.9\Omega_{\rm K} r_{\rm out}^2, \tag{3.41}$$
$$v_r = -\frac{3\nu}{2r_{\rm out}}, \tag{3.42}$$
$$E_{\rm TP} = -0.5\Phi. \tag{3.43}$$

These boundary conditions make the viscous dissipation rates high, which are expected to induce the high injection rates. We confirm that the results are almost unchanged if we set a slowly rotating outer boundary, such as $l_z = 0.3\Omega_{\rm K} r_{\rm out}^2$. For HEPs, we set the outflow boundary condition. Under this condition, the inflow of HEPs at the outer boundary is prohibited such that HEPs that diffuse out from the outer boundary do not return to the calculated region. In this chapter, we assume that HEPs are accelerated only within the critical radius, i.e., the

allocation factors are given as

$$f_{\rm vis} = \begin{cases} f_{\rm v} & (r < r_{\rm crit}) \\ 0 & (r > r_{\rm crit}) \end{cases} , \tag{3.44}$$

$$f_{\rm comp} = \begin{cases} f_{\rm c} & (r < r_{\rm crit}) \\ 0 & (r > r_{\rm crit}) \end{cases} . \tag{3.45}$$

We treat $r_{\rm crit}$, $f_{\rm v}$,and $f_{\rm c}$ as parameters. We set the free boundary conditions for the inner boundary at $r = r_{\rm in}$ because the flow should be supersonic at the vicinity of the black hole. All the variables satisfy the condition $\partial/\partial r = 0$ at $r = r_{\rm in}$.

We summarize our model as a schematic picture in Figure 3.1

3.2 Calculation results

In our formulation, there are several free parameters, such as the diffusion parameter $C_{\rm diff}$, the allocation parameters $f_{\rm v}$ and $f_{\rm c}$, the critical radius $r_{\rm crit}$, and the injection Lorentz factor $\gamma_{\rm inj}$. Since it is too complex to study with all the parameters varying, we fix the parameters $M_{\rm BH}$, $r_{\rm out}$, $r_{\rm in}$, and $r_{\rm crit}$, which are tabulated in Table 3.1. We choose $r_{\rm out} = 150R_{\rm S}$ in order to shorten the calculation time. The effects of HEPs are expected to be large as $r_{\rm crit}$ is large, and we use $r_{\rm crit} = 100R_{\rm S}$. We calculate with the other parameters tabulated in Table 3.2. Group A consists of the models without HEPs ($f_{\rm v} = f_{\rm c} = 0$). We compare the results of group A with the previous global solutions of ADAF in order to confirm validity and consistency of our formulation and method. By comparing the results among groups B-D, we investigate the effects of the ways of injecting HEPs. Injection rates in group B-D are proportional to the viscous dissipation rates, the compressional heating rates, and the total heating rates, respectively. We consider a model E1 in which HEPs take away almost all energy. The dynamical structure of this model is very different from the structures without HEPs.

Table 3.1: Fixed parameters

$M_{\rm BH}/M_\odot$	$r_{\rm out}/R_{\rm S}$	$r_{\rm in}/R_{\rm S}$	$r_{\rm crit}/R_{\rm S}$
10^8	150	1.5	100

Table 3.2: Models and their parameters

models	α	β	$\dot{M}/\dot{M}_{\rm Edd}$	$f_{\rm v}$	$f_{\rm c}$	$\gamma_{\rm inj}$	$C_{\rm diff}$
A1	0.1	10	0.01	0.0	0.0	–	–
A2	0.1	3	0.01	0.0	0.0	–	–
A3	0.1	10	0.001	0.0	0.0	–	–
A4	0.003	10	0.01	0.0	0.0	–	–
B1	0.1	10	0.01	0.3	0.0	10^3	10^4
B2	0.1	10	0.01	0.9	0.0	10^3	10^4
C1	0.1	10	0.01	0.0	0.3	10^3	10^4
C2	0.1	10	0.01	0.0	0.9	10^3	10^4
D1	0.1	10	0.01	0.3	0.3	10^3	10^4
D2	0.1	10	0.01	0.6	0.6	10^3	10^4
D3	0.1	10	0.01	0.9	0.9	10^3	10^4
E1	0.1	10	0.01	0.9	0.9	10^3	10^6

3.2.1 Dynamical structure of flows without high-energy particles

We show the results of group A for which there are no HEP. These results correspond to ADAF models with no radiative cooling. A1 is a reference model, A2 is a model with strong magnetic fields, A3 with a low mass accretion rate, and A4 with a low α parameter. Figure 3.2 shows the radial distributions of (a) the surface density Σ, (b) the specific angular momentum l_z, (c) the radial velocity v_r and effective sound speed $c_{\rm s}$, and (d) the integrated total pressure $P_{\rm tot}$ for group A. From panel (c), we find that transonic solutions are realized in all models

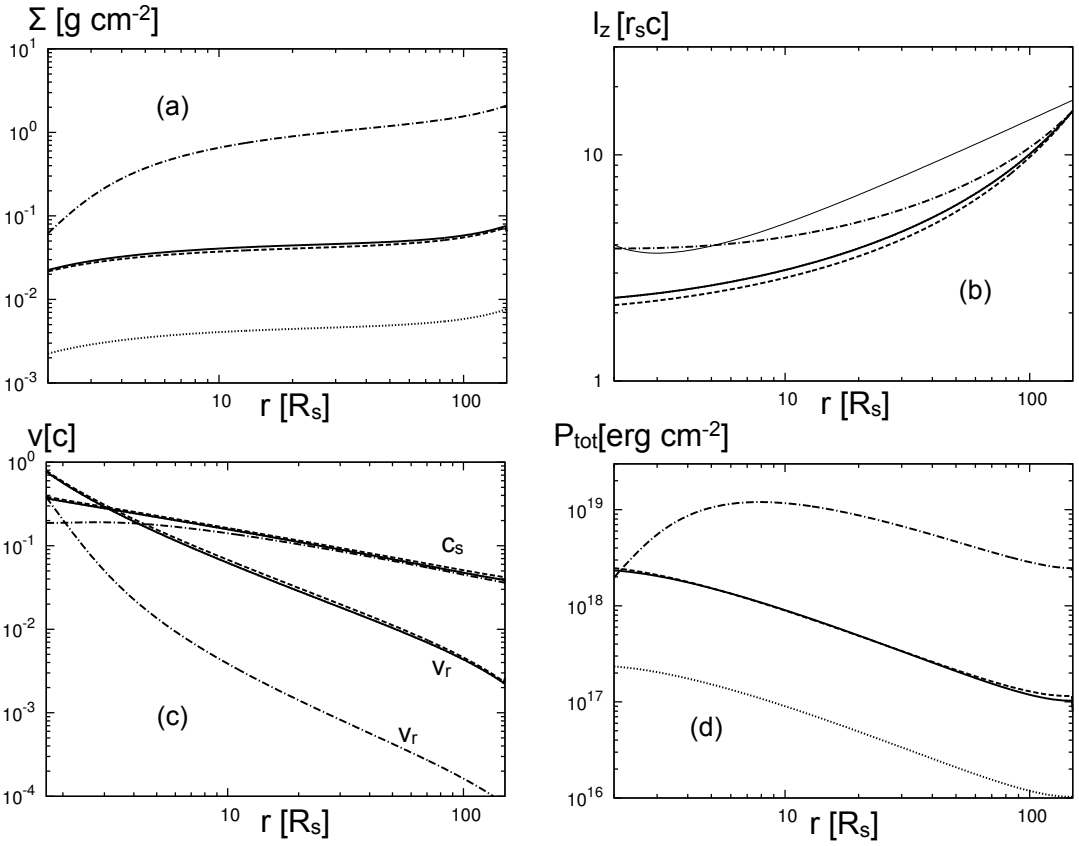

Figure 3.2: Radial distributions of (a) the surface density Σ, (b) the specific angular momentum l_z, (c) the radial velocity v_r and the effective sound speed $c_{\rm s}$, and (d) the integrated total pressure $P_{\rm tot}$ for group A. The solid, dashed, dotted, and dot-dashed lines are for models A1 (reference), A2 (low β), A3 (low $\dot{M}$), and A4 (low α), respectively. The thin solid line in (b) represents the Keplerian angular momentum. This figure is reproduced from Kimura et al. (2014a), by permission of the American Astronomical Society.

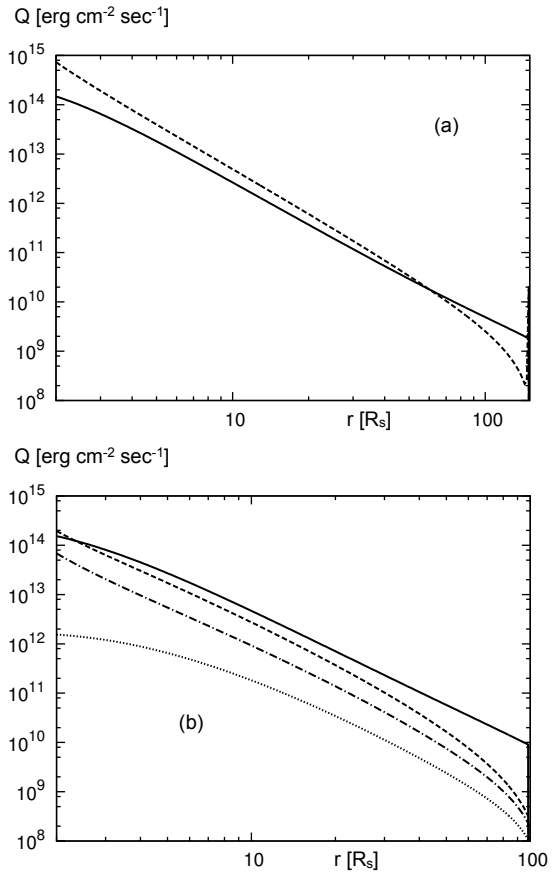

Figure 3.3: (a) Radial distributions of heating rates for A1. The solid and dashed lines show the viscous heating rate and the compressional heating rate, respectively. (b) Radial distributions of the heating and cooling rates for HEPs in D3. The solid, dashed, dotted, and dot-dashed lines show the injection rate, the compressional heating rate, the cooling rate by *pp* collisions, and the proton escaping rate, respectively. This figure is reproduced from Kimura et al. (2014a), by permission of the American Astronomical Society.

by solving time evolution of a system of fluid equations. The sonic radii of our solutions are between $2R_{\rm S}$ and $4R_{\rm S}$, which are consistent with previous global solutions of ADAF (Chen et al. 1997; Nakamura et al. 1997; Narayan et al. 1997).

Comparing A1 ($\beta = 10$, solid lines) with A2 ($\beta = 3$, dashed lines), we found that the strength of the magnetic pressure scarcely affects the dynamical structure. The dashed lines in Figure 3.2 almost overlap with the solid lines. This feature is consistent with the previous solutions (Nakamura et al. 1997). The mass accretion rate affects the surface density and the total pressure. The surface density is proportional to $\dot{M}$, and the total pressure $P_{\rm tot} \propto \Sigma \propto \dot{M}$. We can see this feature in panels (a) and (d) by comparing A3 ($\dot{M} = 0.001$, dotted lines) with A1 ($\dot{M} = 0.01$). However, the mass accretion rate has very little influence on the structure of l_z, v_r, and $c_{\rm s}$. In panels (b) and (c), the dotted lines completely overlap with the solid lines. These dependences on the mass accretion rate are common features of ADAF solutions (Narayan & Yi 1994; Kato et al. 2008).

The α parameter strongly affects the dynamical structure of the flows. For A4 ($\alpha = 0.003$), v_r and Σ are low and high, respectively, while $c_{\rm s}$ is not very different, compared with the reference model A1 ($\alpha = 0.1$). This makes the sonic radius smaller. The low α parameter makes the transport of the angular momentum inefficient, and the flow rotates super Keplerian in $r \simeq 3-4R_{\rm S}$. To realize a transonic solution, the radial velocity rapidly increases as $r \to R_{\rm S}$. This makes the surface density rapidly decrease while $c_{\rm s}$ is almost constant at the inner region $r \lesssim 7R_{\rm S}$. This causes the integrated pressure to decrease rapidly there. Thus, the integrated pressure has the maximum at $r \simeq 7R_{\rm S}$. These features are also seen in previous solutions (Chen et al. 1997; Nakamura et al. 1997; Narayan et al. 1997). Therefore, our solutions are consistent with numerical solutions found in other studies.

We check the energy balance of the flow. Figure 3.3 (a) represents the heating rates for A1. The solid and dashed lines show the viscous dissipation and compressional heating rates, respectively. It is seen that the compressional heating is dominant in the inner region ($r \lesssim 60R_{\rm S}$) while the viscous dissipation is higher than the compressional heating in the outer

region ($r \gtrsim 60R_{\rm S}$). However, the compressional heating rate is at most eight times higher than the viscous dissipation rate at the innermost region. Both the compressional heating and the viscous dissipation are important to heat up TPs in this model. In previous papers, the energy balance was discussed by using the entropy. In that viewpoint, the compressional heating is included in the advection term of the entropy (cf., Narayan & Yi 1994; Narayan et al. 1997), and what determines the internal energy has not been explicitly discussed.

3.2.2 Dynamical structure of flows with high-energy particles

In this section, we show the results of models including HEPs. First, we compare the results with different injection models. Group B consists of the models with $f_{\rm v} \neq 0$ and $f_{\rm c} = 0$, in which injection rates are related only to the viscous dissipation. Figure 3.4 shows the radial distributions of (a) the surface density Σ, (b) the specific angular momentum l_z, and (c) the radial velocity v_r and the effective sound speed $c_{\rm s}$. From panels (a) and (b), the surface density and angular momentum distributions of B1 ($f_{\rm v} = 0.3$) are almost same as A1 ($f_{\rm v} = f_{\rm c} = 0$). The surface density and the specific angular momentum of B2 ($f_{\rm v} = 0.9$) are a few tens of percent higher than those of A1. Similarly, v_r and $c_{\rm s}$ of B2 are a few tens of percent lower than those of A1. Panel (d) shows the radial distributions of the integrated pressure for B2, from which we found that $P_{\rm TP}$ is about twice higher than $P_{\rm HEP}$. Even with $f_{\rm v} = 0.9$, $P_{\rm TP}$ always dominates over $P_{\rm HEP}$. This is due to the efficient compressional heating, which dominates over the viscous dissipation in the inner region. It is found that HEPs have little influence on the dynamical structure for the models in group B because the total injected energy is not so high compared with the total energy that heats up TPs. The thermal pressure for B2 is nearly half of that for A1. This is because some fraction of the dissipation energy is expended for injection of HEPs. Note that the compressional heating rate of B2 is about twice lower than that of A1 since the compressional heating rates are proportional to $P_{\rm TP}$.

Since the compressional heating dominates over the viscous dissipation at the inner region, it is worth investigating the effects of injection related only to the compressional heating.

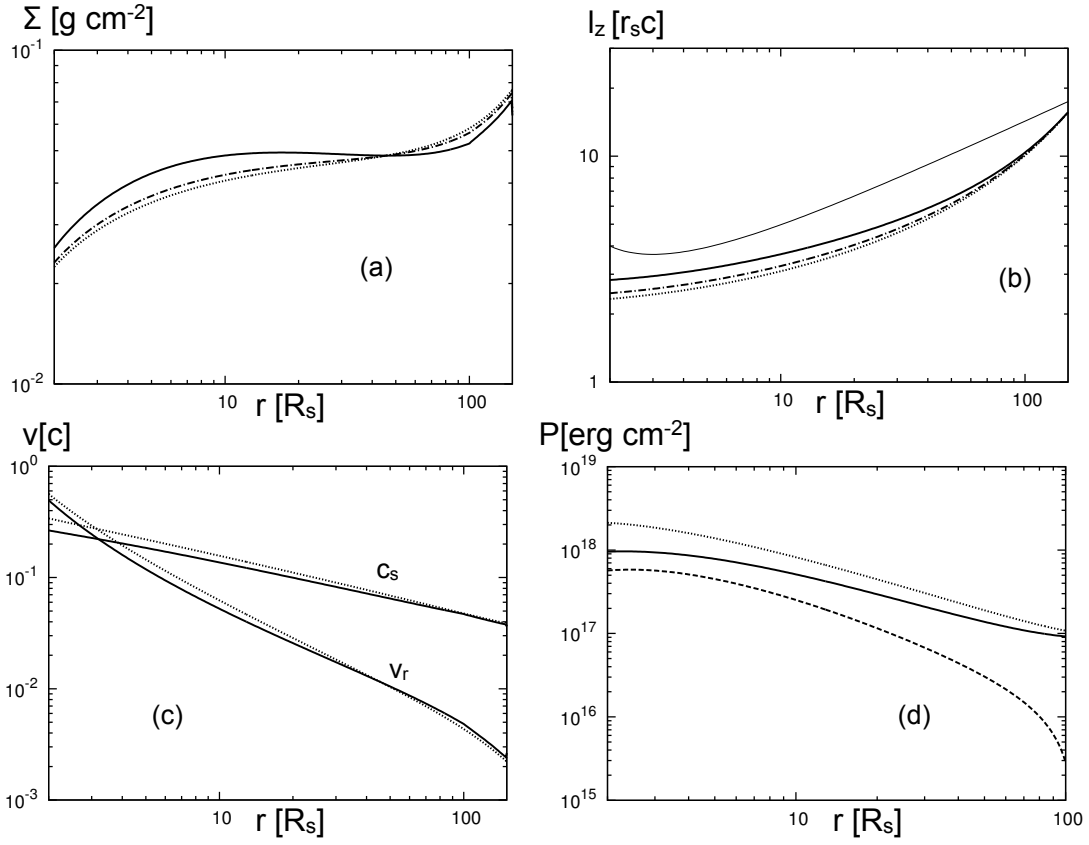

Figure 3.4: Radial distributions of (a) the surface density Σ, (b) the specific angular momentum l_z, (c) the radial velocity v_r and the effective sound speed $c_{\rm s}$, for group B. The solid, dot-dashed, and dotted lines are for B2 ($f_{\rm v} = 0.9$), B1 ($f_{\rm v} = 0.3$), and A1 (no HEPs for reference), respectively. The thin solid line in (b) represents the Keplerian angular momentum. (d) Radial distributions of the integrated pressure for B2. The solid and dashed lines represent $P_{\rm TP}$ and $P_{\rm HEP}$, respectively. The dotted line depicts $P_{\rm TP}$ for A1 (no HEPs) for reference. This figure is reproduced from Kimura et al. (2014a), by permission of the American Astronomical Society.

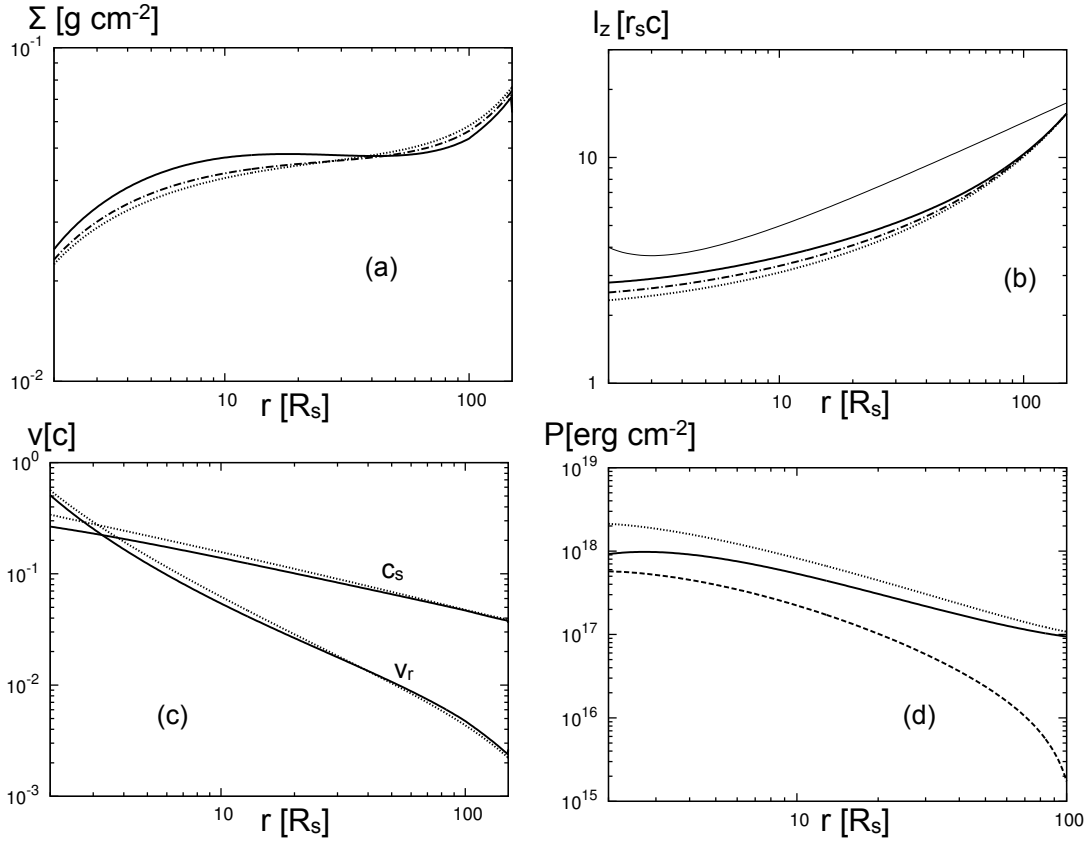

Figure 3.5: Radial distributions of (a) the surface density Σ, (b) the specific angular momentum l_z, (c) the radial velocity v_r and the effective sound speed $c_{\rm s}$, for group C. The solid, dot-dashed, and dotted lines are for C2 ($f_{\rm c} = 0.9$), C1 ($f_{\rm c} = 0.3$), and A1 (no HEPs for reference), respectively. The thin solid line in (b) represents the Keplerian angular momentum. (d) Radial distributions of the integrated pressure for C2. The solid and dashed lines represent $P_{\rm TP}$ and $P_{\rm HEP}$, respectively. The dotted line depicts $P_{\rm TP}$ for A1 (no HEPs) for reference. This figure is reproduced from Kimura et al. (2014a), by permission of the American Astronomical Society.

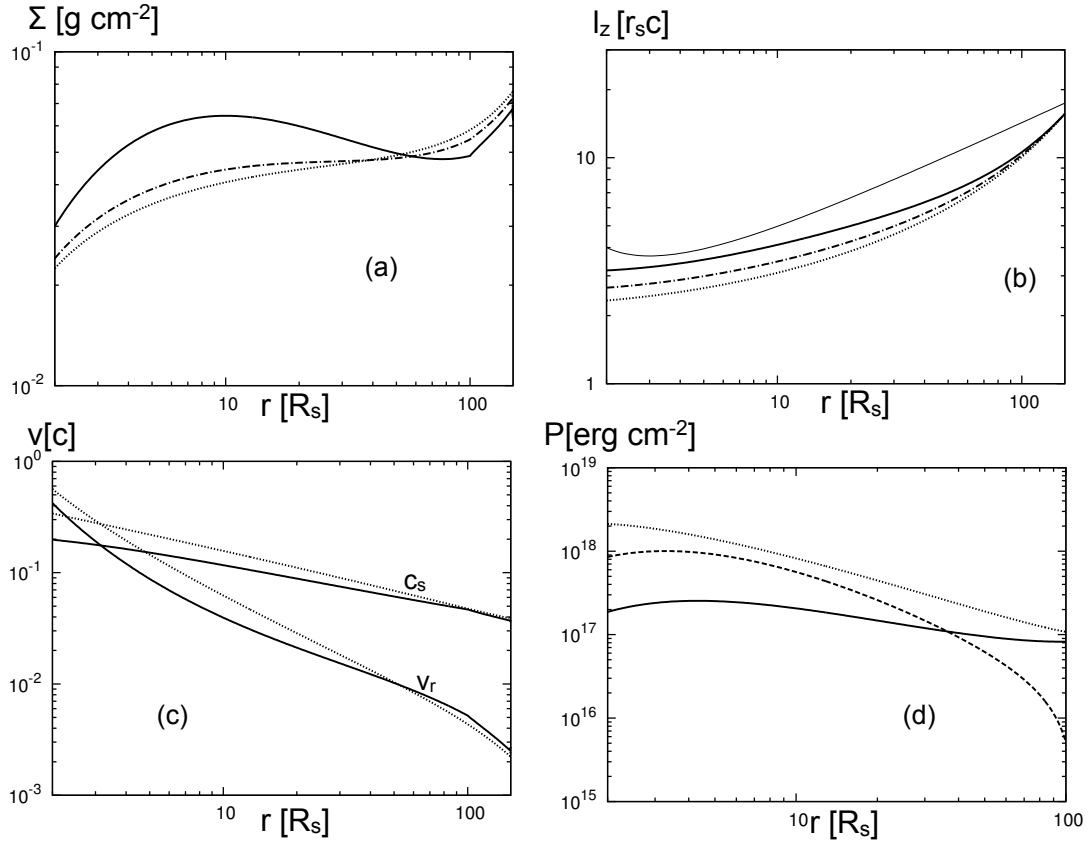

Figure 3.6: Radial distributions of (a) the surface density Σ, (b) the specific angular momentum l_z, (c) the radial velocity v_r and the effective sound speed $c_{\rm s}$, for group D. The solid, dot-dashed, and dotted lines are for D3 ($f_{\rm v} = f_{\rm c} = 0.9$), D1 ($f_{\rm v} = f_{\rm c} = 0.3$), and A1 (no HEPs for reference), respectively. The thin solid line in (b) represents the Keplerian angular momentum. (d) Radial distributions of the integrated pressure for D3. The solid and dashed lines represent $P_{\rm TP}$ and $P_{\rm HEP}$, respectively. The dotted line depicts $P_{\rm TP}$ for A1 (no HEPs) for reference. This figure is reproduced from Kimura et al. (2014a), by permission of the American Astronomical Society.

Group C consists of the models with $f_{\rm v} = 0$ and $f_{\rm c} \neq 0$, in which the injection rates are related only to the compressional heating. Figure 3.5 shows the radial structures of the solutions of group C. They are quite similar to those of group B. From panels (a) and (b) of Figure 3.5, it is seen that the radial structure of C1 ($f_{\rm c} = 0.3$) is nearly the same as that of A1 ($f_{\rm v} = f_{\rm c} = 0$). We found that HEPs scarcely affect the dynamical structure and that $P_{\rm TP} > P_{\rm HEP}$ everywhere even for model C2 ($f_{\rm c} = 0.9$). At $r = r_{\rm crit}$, the viscous dissipation rate is higher than the compressional heating rate, so that $P_{\rm HEP}$ in the outer region is slightly lower than that for group B. The compressional heating is expended to inject HEPs rather than to heat up TPs. This causes the specific internal energy of TPs to be low, and the angular momentum of C2 is slightly higher than that of A1 owing to inefficient transport of the angular momentum. This makes the viscous dissipation rate slightly higher, and the injection rate is lower than the dissipation rate except for the innermost region $r \lesssim 3R_{\rm S}$. Thus, the injection only from the compressional heating cannot energize HEPs enough to satisfy $P_{\rm HEP} > P_{\rm TP}$. Although the compression does not heat up TPs in group C, the slightly high dissipation rate causes the total heating rate for TPs in C2 to be nearly the same as that in B2. This is why the results of group C are quite similar to those of group B.

The pressure of HEPs does not dominate over the thermal pressure in groups B and C. This motivates us to investigate the models in which the injection rates are proportional to the total heating rates. Group D consists of such models with $f_{\rm v} = f_{\rm c} \neq 0$. Figure 3.6 shows the radial structures of the solutions of models D1 and D3. From panels (a) and (b) of Figure 3.6, we can see that the profiles of Σ and l_z of D1 ($f_{\rm v} = f_{\rm c} = 0.3$) are nearly the same as those of A1. For this model, the allocation factors $f_{\rm c}$ and $f_{\rm v}$ are so low that $P_{\rm HEP} < P_{\rm TP}$ is satisfied everywhere. From panel (d) of Figure 3.6, we see that $P_{\rm TP} < P_{\rm HEP}$ in $r \lesssim 40R_{\rm S}$ for D3 ($f_{\rm v} = f_{\rm c} = 0.9$). Since almost all energy released is spent to inject HEPs, the temperature of thermal particles ($k_{\rm B}T = P_{\rm TP}/\Sigma$) of D3 is about 20 times lower than that for A1 in $r \lesssim 10R_{\rm S}$, This may affect the electron temperature, although we ignore the electron component in this chapter. On the other hand, $P_{\rm tot}$ of D3 is not different from that of A1 by an order of magnitude due to large

$P_{\rm HEP}$. Although $P_{\rm TP} < P_{\rm HEP}$ is realized for model D3, other variables for D3 are at most a few times higher or lower than A1. Even if $P_{\rm HEP} > P_{\rm TP}$, HEPs do not strongly affect the radial profiles of $v_r,\ c_{\rm s},\ l_z$, and Σ.

We explain how HEPs affect the dynamical structure of the accretion flows. The solutions with higher $f_{\rm v}$ and/or $f_{\rm c}$ have slightly higher Σ, higher l_z, lower v_r, lower $c_{\rm s}$, and lower $P_{\rm tot}$. As HEPs gain a large fraction of released energy, the specific heat ratio of accreting materials is lower. This makes $P_{\rm tot}$ low, and the angular momentum transport is inefficient. This causes the angular momentum to be high, and the strong centrifugal force makes v_r low. The low v_r causes Σ to be high such that the mass accretion rate is constant. However, the effects of the specific heat ratio cannot change the dynamical structure by an order of magnitude even if $P_{\rm TP} < P_{\rm HEP}$ is satisfied. The flow structures are the advection-dominated flows for the models in groups B, C, and D.

This ADAF structures can be changed by HEPs when they extract almost all energy released. We calculate the model E1 ($f_{\rm v} = f_{\rm c} = 0.9,\ C_{\rm diff} = 10^6$) in which the accretion flow loses most of the energy by proton escape. Figure 3.7 shows the results of E1. In this model, the integrated pressure of HEPs is much lower than $P_{\rm TP}$ because the escaping protons take away almost all the injected energy. This makes $c_{\rm s}$ low, which causes l_z to be high. From panel (b), we can see that in $r \lesssim 8R_{\rm S}$, the flow has the Keplerian angular momentum. Since the centrifugal force is strong owing to the high l_z, v_r is low and thereby Σ is high. Although HEPs extract almost all energy, $P_{\rm TP}$ for E1 is not so different from that for A1 except in $r \lesssim 5R_{\rm S}$. This is because the increment of Σ balances the decrement of $c_{\rm s}$. To realize a transonic solution, the radial velocity is rapidly increasing in the inner region ($r \lesssim 5R_{\rm S}$). This causes the surface density to be rapidly decreasing, so that the integrated pressure has maximum at $r \sim 5R_{\rm S}$. This result indicates that an ADAF solution changes to a Keplerian thin disk when almost all energy is taken away from the accretion flow by HEPs, which is consistent with the self-similar solution obtained by Narayan & Yi (1994). However, this drastic change seem to make the radiative cooling of electrons important (see Section 3.3.2).

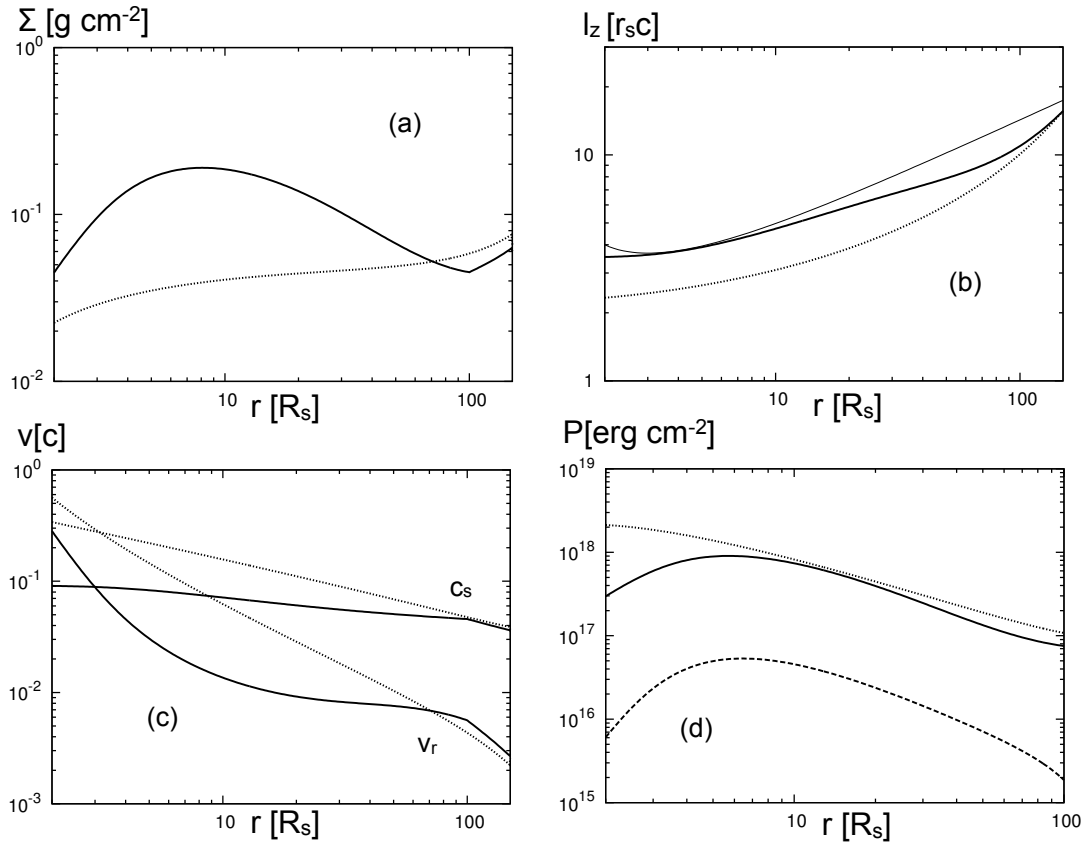

Figure 3.7: Radial distributions of (a) the surface density Σ, (b) the specific angular momentum l_z, (c) the radial velocity v_r and the effective sound speed $c_{\rm s}$, for model E1. The solid and dotted lines are for E1 ($f_{\rm v} = f_{\rm c} = 0.9$) and A1 (no HEPs for reference), respectively. The thin solid line in (b) represents the Keplerian angular momentum. (d) Radial distributions of the integrated pressure for E1. The solid and dashed lines represent $P_{\rm TP}$ and $P_{\rm HEP}$, respectively. The dotted line depicts $P_{\rm TP}$ for A1 (no HEPs) for reference. This figure is reproduced from Kimura et al. (2014a), by permission of the American Astronomical Society.

Next, we discuss what determines the number and energy densities of HEPs. Figure 3.3 (b) indicates the heating rates and cooling rates of HEPs for D3. We can see that the injection rate $Q_{\rm inj}$ and the compressional heating rate $Q_{\rm V,HEP}$ are higher than the cooling rate by pp collisions $Q_{\rm sink}$ and the diffusive escaping rate $Q_{\rm diff}$ everywhere. We find that $Q_{\rm V,HEP} \lesssim Q_{\rm inj}$ and that $Q_{\rm V,HEP}$ is not so high as to make $\gamma_{\rm m}$ much higher than $\gamma_{\rm inj}$. Thus, the mean Lorentz factor is nearly the same value as the injected value,

$$\gamma_{\rm m} \sim \gamma_{\rm inj}. \tag{3.46}$$

This condition is satisfied within a factor of two. This result implies that the balance between $Q_{\rm inj}$ and the advection term, which is the second term of the left side of Equation (3.15), determines $U_{\rm HEP}$ and $N_{\rm HEP}$. Note that the dominant process energizing the HEPs is different among D1, D2, and D3. For D3 ($f_{\rm v} = f_{\rm c} = 0.9$), the injection from the viscous dissipation mainly energizes HEPs because $P_{\rm TP}$ is so low that the injection from the compressional heating is inefficient. On the other hand, the injection from the compressional heating is dominant for D1 ($f_{\rm v} = f_{\rm c} = 0.3$) because $P_{\rm TP}$ is high enough to satisfy $Q_{\rm vis} < Q_{\rm V,TP}$. Both the viscous dissipation and the compressional heating make nearly the same contribution to the injection for D2 ($f_{\rm v} = f_{\rm c} = 0.6$).

3.2.3 Luminosities of escaping particles

We also calculate luminosities of escaping gamma rays, neutrinos, neutrons, and protons. We define the luminosities as

$$L_i = \int_{r_{\rm in}}^{r_{\rm out}} 2\pi r Q_i dr, \tag{3.47}$$

where i refers to the kind of escaping particles and Q_i is the energy flux. We use $Q_{\rm n} = Q_{\rm esc}$ for the neutron luminosity and $Q_{\rm p} = Q_{\rm diff}$ for the proton luminosity. For estimating the luminosity of gamma rays and neutrinos, we assume that all kinds of pions produced by pp collisions have the same energy, $Q_{\pi^j} = Q_\pi/3$, where $j = +,\ -$, or 0. Neutral pions decay into gamma rays following Equation (1.4), and charged pions decay into neutrinos, electrons, and

positrons following Equations (1.5) and (1.6). The electrons and the positrons are considered to lose most of their energies rapidly by emitting gamma rays, and thus, we assume that their energies are converted to the energy of gamma rays. Roughly speaking, the pion energy is equally divided among the final products (Begelman et al. 1990). Under these assumptions and assuming that all photons and neutrinos can escape, Q_ν and Q_γ are represented as

$$Q_\nu = \frac{3}{4}Q_{\pi^+} + \frac{3}{4}Q_{\pi^-} = \frac{1}{2}Q_\pi, \tag{3.48}$$

$$Q_\gamma = Q_{\pi^0} + \frac{1}{4}Q_{\pi^+} + \frac{1}{4}Q_{\pi^-} = \frac{1}{2}Q_\pi. \tag{3.49}$$

In this treatment, $Q_\gamma = Q_\nu$ is always satisfied, which leads to $L_\gamma = L_\nu$. When all the neutrons escape, the ratio of $L_{\rm n}$ to $L_\gamma (= L_\nu)$ is determined exclusively by $P_{\rm p\to n}$ and K_π as

$$L_{\rm n}/L_\gamma = [P_{\rm p\to n}(1 - K_\pi)]/K_\pi. \tag{3.50}$$

In this model, we use $P_{\rm p\to n} = 1/2$ and $K_\pi = 1/2$, so that $L_{\rm n}/L_\gamma = 1/2$.

We see the parameter dependences of the luminosities of the escaping particles. We choose model D1 as a reference model. The parameters of the models calculated additionally are tabulated in Table 3.3. We calculate various values of $f_{\rm v} = f_{\rm c}$ (for groups D and F), $\dot{M}$ (for group G), $C_{\rm diff}$ (for groups H and I), and $\gamma_{\rm inj}$ (for groups J and K). Figure 3.8 shows the luminosities of protons, neutrons, and gamma rays, $L_{\rm p}$, $L_{\rm n}$, and L_γ. Panel (a) shows the luminosities as a function of the allocation parameters under the condition $f_{\rm v} = f_{\rm c}$, where we show the results of groups D and F. We calculate the models in group F in order to show the effects of β. The luminosity of the protons is the largest of the three and reaches about $2 \times 10^{-2}\dot{M}c^2$. The gamma-ray or neutrino luminosity is lower than $L_{\rm p}$ by about an order of magnitude, $L_\gamma = L_\nu \lesssim 10^{-3}\dot{M}c^2$. In these groups, most of the generated neutrons can escape owing to high $\gamma_{\rm inj}$, so that $L_{\rm n}/L_\gamma = 1/2$. High $f_{\rm v}$ makes the thermal pressure low and thereby weakens the magnetic fields, which makes the diffusion coefficient higher. Thus, the dependence of $L_{\rm p}$ on $f_{\rm v}$ is slightly stronger as $f_{\rm v}$ is closer to unity. The proton luminosity is low for low β because the strong magnetic fields prevent the protons from escaping. On the other hand, $L_{\rm n}$ and L_γ are nearly independent of β owing to their charge neutrality.

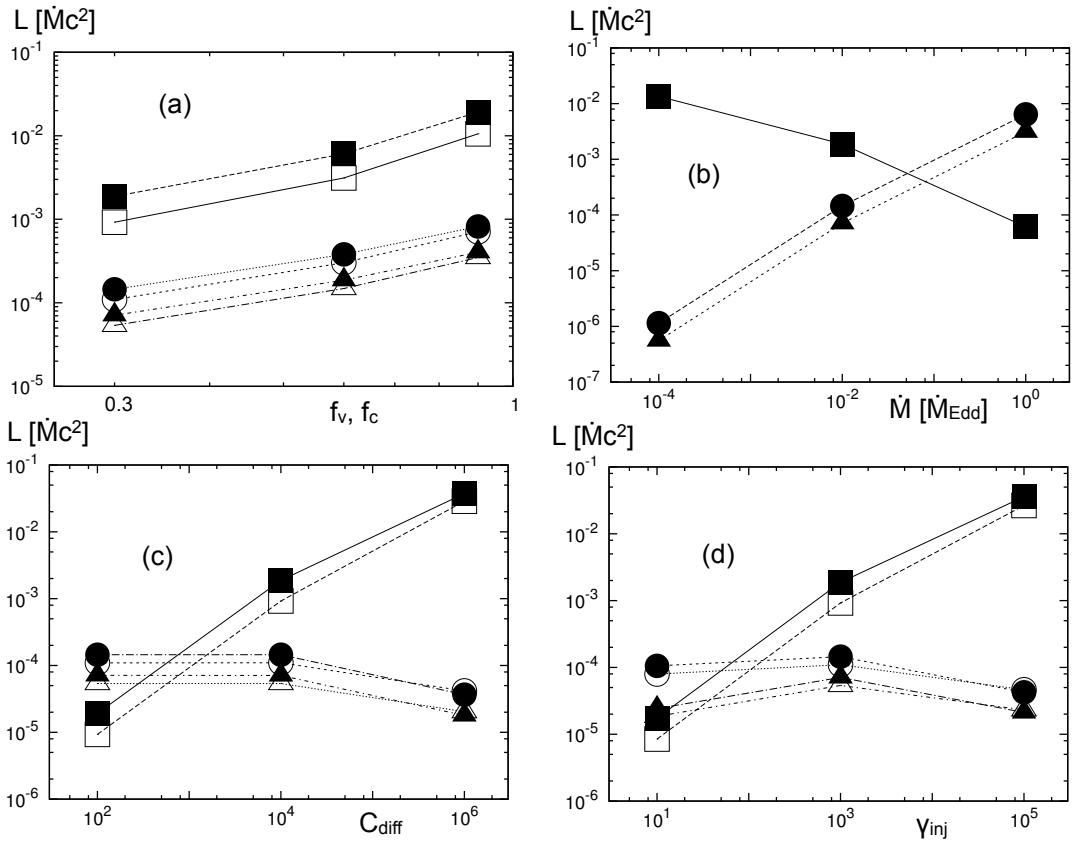

Figure 3.8: Luminosities of the escaping particles as the functions of parameters. The squares, circles, and triangles denote $L_{\rm p}$, $L_\gamma = L_\nu$, and $L_{\rm n}$, respectively. The open and filled symbols are $\beta = 3$ and $\beta = 10$, respectively. (a) Dependence on $f_{\rm v} = f_{\rm c}$. This panel shows the results for D1, D2, D3, F1, F2, and F3. (b) Dependence on $\dot{M}$. This panel shows the results for D1, G1 and G2. (c) Dependence on $C_{\rm diff}$. This panel shows the results for D1, H1, H2, I1, I2, and I3. (d) Dependence on $\gamma_{\rm inj}$. This panel shows the results for D1, J1, J2, K1, K2, and K3. This figure is reproduced from Kimura et al. (2014a), by permission of the American Astronomical Society.

Table 3.3: Models and their parameters

models	α	β	$\dot{M}/\dot{M}_{\rm Edd}$	$f_{\rm v}$	$f_{\rm c}$	$\gamma_{\rm inj}$	$C_{\rm diff}$
F1	0.1	3	0.01	0.3	0.3	10^3	10^4
F2	0.1	3	0.01	0.6	0.6	10^3	10^4
F3	0.1	3	0.01	0.9	0.9	10^3	10^4
G1	0.1	10	0.0001	0.3	0.3	10^3	10^4
G2	0.1	10	1.0	0.3	0.3	10^3	10^4
H1	0.1	10	0.01	0.3	0.3	10^3	10^2
H2	0.1	10	0.01	0.3	0.3	10^3	10^6
I1	0.1	3	0.01	0.3	0.3	10^3	10^2
I2	0.1	3	0.01	0.3	0.3	10^3	10^4
I3	0.1	3	0.01	0.3	0.3	10^3	10^6
J1	0.1	10	0.01	0.3	0.3	10^1	10^4
J2	0.1	10	0.01	0.3	0.3	10^5	10^4
K1	0.1	3	0.01	0.3	0.3	10^1	10^4
K2	0.1	3	0.01	0.3	0.3	10^3	10^4
K3	0.1	3	0.01	0.3	0.3	10^5	10^4

Panel (b) represents the $\dot{M}$ dependence, where we show the results for D3, G1, and G2. For the low mass accretion rate $\dot{M} = 10^{-4}\dot{M}_{\rm Edd}$, $L_{\rm p} \sim 10^{-2}\dot{M}c^2$ and $L_{\rm n} \sim 10^{-6}\dot{M}c^2$ while $L_{\rm p} \sim 10^{-4}\dot{M}c^2$ and $L_{\rm n} \sim 3 \times 10^{-3}\dot{M}c^2$ for the high mass accretion rate $\dot{M} = \dot{M}_{\rm Edd}$. The high mass accretion rates strengthen the magnetic fields and thereby decrease the diffusion coefficient as $\kappa \propto B^{-1} \propto \dot{M}^{-1/2}$. The high mass accretion rates also strengthen the injection rates, which makes the energy density of HEPs higher as $U_{\rm HEP} \propto Q_{\rm inj} \propto P_{\rm tot} \propto \dot{M}$. Thus, roughly speaking, $L_{\rm p} \propto \kappa U_{\rm HEP} \propto BP_{\rm tot} \propto \dot{M}^{1/2}$. Note that if we normalize $L_{\rm p}$ by the accretion luminosity $\dot{M}c^2$, it is a decreasing function of mass accretion rates as $L_{\rm p}/(\dot{M}c^2) \propto \dot{M}^{-1/2}$. The

neutrons and γ-ray luminosities are nearly proportional to $\dot{M}^2$ since $L \propto \Sigma N_{\rm HEP} \propto \dot{M}^2$. We can see that $L_{\rm p} > L_{\rm n}$ for $\dot{M} \lesssim 10^{-1}\dot{M}_{\rm Edd}$ and vice versa.

Panel (c) expresses the dependence on $C_{\rm diff}$, where we show the results for D3 and the models in groups H and I. The models in group I are different from those in group H in the value of β. For $C_{\rm diff} \lesssim 10^4$, the diffusive escaping rate is not so high that the balance of advection and injection determines the energy density of HEPs. In this situation, $L_{\rm p} \propto \kappa \propto C_{\rm diff}B \propto C_{\rm diff}\beta^{1/2}$, and $L_{\rm n}$ and L_γ are not affected by the diffusion phenomena and are thereby nearly independent of $C_{\rm diff}$ and β. However, for very high $C_{\rm diff}$, the escaping rate is high enough to balance the injection rate, so that $L_{\rm p}$ is limited at $L_{\rm p} \sim 0.1 f_{\rm v}\dot{M}c^2$. Since the injection rates are nearly independent of β, $L_{\rm p}$ for I2 ($\beta = 10$, $C_{\rm diff} = 10^6$) is nearly equal to that for J3 ($\beta = 3$, $C_{\rm diff} = 10^6$). Efficient proton escape makes $N_{\rm HEP}$ low, which decreases the collision rate. Thus, $L_{\rm n}$ and L_γ with $C_{\rm diff} = 10^6$ are several times lower than those in $C_{\rm diff} = 10^4$.

Panel (d) depicts the $\gamma_{\rm inj}$ dependence of luminosities, where we show the results for D3 and the models in groups J and K. The models in group K are different from those in group J in the value of β. The $L_{\rm p}$ and L_γ in panel (d) are quite similar to those in panel (c). For $\gamma_{\rm inj} \lesssim 10^3$, the proton luminosity is proportional to $\gamma_{\rm inj}$ since $L_{\rm p} \propto \kappa \propto \gamma_{\rm inj}$. The gamma-ray luminosity is nearly independent of $\gamma_{\rm inj}$. The number density of HEPs is inversely proportional to $\gamma_{\rm inj}$, while the energy per interaction is proportional to $\gamma_{\rm inj}$. Since these effects balance, L_γ is nearly independent of $\gamma_{\rm inj}$. On the other hand, the neutron luminosity with $\gamma_{\rm inj} = 10$ is a few times lower than that with $\gamma_{\rm inj} = 10^3$. This is because the neutrons cannot escape from the outer region ($r \sim 100R_{\rm S}$) with low $\gamma_{\rm inj}$ while they can escape with high $\gamma_{\rm inj}$. For very high $\gamma_{\rm inj} \sim 10^5$, the proton escaping rate is so high that escaping protons can extract almost all injected energy. This is the same situation as the case with very high $C_{\rm diff}$. The proton luminosity is nearly equal to the total injection luminosity $0.1 f_{\rm v}\dot{M}c^2$, and $L_{\rm n}$ and L_γ with $\gamma_{\rm inj} = 10^5$ are several times lower than those with $\gamma_{\rm inj} = 10^3$.

The proton luminosity strongly depends on many uncertain parameters such as $\gamma_{\rm inj}$ and $C_{\rm diff}$. This is due to the uncertainty of diffusion and acceleration of HEPs in the accretion

flows. On the other hand, the gamma-ray, neutrino, and neutron luminosities do not have strong dependence on such parameters. These luminosities strongly depend only on the mass accretion rates. For widely acceptable ADAF mass accretion rates ($\dot{M} \lesssim 10^{-2}\dot{M}_{\rm Edd}$), these luminosities are less than about $10^{-4}\dot{M}c^2$. This value is negligibly low to change the dynamical structure from ADAF to the standard disk-like structure.

We also estimate the mass-escaping rates defined as

$$\dot{M}_i = \int_{r_{\rm in}}^{r_{\rm out}} 2\pi r m_i \dot{N}_i dr, \tag{3.51}$$

where i =p or n. We use $\dot{N}_{\rm p} = \dot{N}_{\rm diff}$ and $\dot{N}_{\rm n} = \dot{N}_{\rm sink}$. Escaping protons have the Lorentz factor $\gamma_{\rm esc} \sim \gamma_{\rm inj}$, and we can write the mass-escaping rates as

$$\dot{M}_{\rm p} \sim \frac{L_{\rm p}}{\gamma_{\rm inj} c^2}. \tag{3.52}$$

The Lorentz factor of escaping neutrons is nearly half of $\gamma_{\rm inj}$. The mass-escaping rates of escaping neutrons are represented as

$$\dot{M}_{\rm n} \sim \frac{2L_{\rm n}}{\gamma_{\rm inj} c^2}. \tag{3.53}$$

Since $L_{\rm p} \propto \gamma_{\rm inj}$ in usual, $\dot{M}_{\rm p}$ is independent of $\gamma_{\rm inj}$. On the other hand, $\dot{M}_{\rm n}$ is lower as $\gamma_{\rm inj}$ is lower because $L_{\rm n}$ has a weak dependence on $\gamma_{\rm inj}$. We find that $\dot{M}_{\rm p} \lesssim 10^{-4}\dot{M}$ and $\dot{M}_{\rm n} \lesssim 10^{-3}\dot{M}$ in our calculation. Since both $\dot{M}_{\rm n}$ and $\dot{M}_{\rm p}$ are sufficiently less than $\dot{M}$, the assumption that we neglect the sink term in Equations (3.3) and (3.4) is valid.

3.3 Discussion

3.3.1 Implications for jet production

As we have seen in Chapter 2, HEPs escaping from the accretion flows are expected to be related to the jet production. They are likely to inject some amount of kinetic energy and mass in the funnel, which is available to launch the kinetically dominated jet. Although the escaping

particles are considered to be isotropic, we discuss the case with the most efficient injection in which all the escaping particles are injected in the funnel. If the accretion rate is high, the neutron luminosity is higher than the proton luminosity, and it amounts to $L_{\rm n} \sim 10^{-2}\dot{M}c^2$ for G2. We note that what occurs in the high mass accretion rate is controversial because the electron component is not expected to be negligible (see Section 3.3.2). For the lower mass accretion rates, $L_{\rm n}$ is lower since the neutron production is ineffective. In such situation, $L_{\rm p}$ is higher than $L_{\rm n}$ if $\gamma_{\rm inj}$ is high, and the proton luminosity attains $L_{\rm p} \sim 10^{-2}\dot{M}c^2$ for the efficient escaping models H2, I3, J2, and K3 ($C_{\rm diff} = 10^6$ or $\gamma_{\rm inj} = 10^5$). Therefore, for AGN jets with $L_{\rm jet} \lesssim 10^{-2}\dot{M}c^2$, the energy injection by escaping particles is one of the viable mechanisms for launching a relativistic jet over a broad range of mass accretion rates. In this model, the terminal Lorentz factor is roughly equal to the average random Lorentz factor of particles. If there is no other mass injection except for the escape of HEPs, the terminal Lorentz factor of the jet is estimated as $\Gamma \sim \gamma_{\rm inj}$. For $\gamma_{\rm inj} = 1000$, this value is too high in comparison to observed values.

For bright AGN jets that have $L_{\rm jet} \gtrsim 10^{-2}\dot{M}c^2$, the energy injection rates by escaping HEPs are not sufficient. The magnetically dominated jet models are feasible for these jets. Although HEPs are expected to act as the source of mass injection, they cannot inject sufficient amount of mass in our model. Mass injection rates to jets are $\dot{M}_{\rm n} \lesssim 10^{-3}\dot{M}$ for neutrons and $\dot{M}_{\rm p} \lesssim 10^{-4}$ for protons. This seems to be too low to explain the bright AGN jets $L_{\rm jet} \sim L_{\rm Edd}$ with $\Gamma = 10 - 100$.

Toma & Takahara (2012) first calculated the injection rates of mass and energy in the funnel by escaping neutrons. They used a power-law energy spectrum of the isotropically escaping neutrons and calculated the injection rates only for the neutrons that decay in the funnel, although they did not solve the structure of the accretion flow. They estimate $L_{\rm n} \lesssim 2 \times 10^{-3}\dot{M}c^2$ and $\dot{M}_{\rm n} \lesssim 6 \times 10^{-4}\dot{M}$. The total rates, including the neutrons that do not decay in the funnel, i.e., the isotropic escaping rates, are around $L_{\rm n} \sim 0.03\dot{M}c^2$, which is slightly higher than those in our models. This is because they assume the high heating rate and the

short infall timescale $t_{\rm fall} \equiv r/v_r$ at the vicinity of a SMBH. On the other hand, our model does not include the spectrum of HEPs that is considered to affect the escaping rates of HEPs. In order to clarify injection rates of mass and kinetic energy, we should construct a more realistic model (see Section 3.3.2).

3.3.2 Effects of ignored processes

In this chapter, we ignore the effects of the electron component and radiation from the thermal component. If electrons obtain a large amount of thermal energy, they radiate the energy away by synchrotron emission and bremsstrahlung. Under the assumption that electrons obtain thermal energy from protons by Coulomb collisions and that electrons are non-relativistic, the timescale of energy transport from protons to electrons is estimated as (cf., Spitzer 1962; Takahara & Kusunose 1985)

$$t_{\rm p-e} = \sqrt{\frac{\pi}{2}} \frac{m_{\rm p}}{m_{\rm e}} \frac{1}{n\sigma_{\rm T} c \ln\Lambda} \left(\frac{kT_{\rm p}}{m_{\rm p}c^2} + \frac{kT_{\rm e}}{m_{\rm e}c^2} \right)^{3/2}, \tag{3.54}$$

where we use the Coulomb logarithm $\ln\Lambda$, the Boltzmann constant k, the proton temperature $T_{\rm p}$, the electron temperature $T_{\rm e}$, and the electron mass $m_{\rm e}$. We estimate $t_{\rm p-e}$ under the assumption that $T_{\rm e}/m_{\rm e} = T_{\rm p}/m_{\rm p}$. If the energy transport time $t_{\rm p-e}$ is less than the infall time $t_{\rm fall}$, the effects of the electron component should be relevant. At $r \sim 10R_{\rm S}$, the ratio of these two timescales is roughly $t_{\rm p-e}/t_{\rm fall} \sim 10$ for $\dot{M} = 0.01\dot{M}_{\rm Edd}$ and $t_{\rm p-e}/t_{\rm fall} \sim 0.1$ for $\dot{M} = \dot{M}_{\rm Edd}$. Thus, for low mass accretion rates like $\dot{M} = 0.01\dot{M}_{\rm Edd}$, the electrons do not affect the dynamics of the flow whereas the effects of electrons should not be ignored for high mass accretion rates as $\dot{M} \simeq \dot{M}_{\rm Edd}$. The solutions realized in such situations are not well understood, and thus we are not concerned with this problem. If we consider high $f_{\rm v}$ and $f_{\rm c}$, the density is high, and $c_{\rm s}$ and v_r are low. This makes it difficult to satisfy $t_{\rm p-e} > t_{\rm fall}$. For model D3 $t_{\rm p-e}/t_{\rm fall} \sim 0.3$ at $r \sim 10R_{\rm S}$, and for model E1, $t_{\rm p-e}/t_{\rm fall} \sim 0.03$ at $r \sim 10R_{\rm S}$ even if $\dot{M} = 0.01\dot{M}_{\rm Edd}$. Thus, when HEPs affect the dynamical structure, the electrons are also expected to play important roles on the dynamical structure.

When $P_{\rm HEP} > P_{\rm TP}$, the temperature of thermal protons are significantly lower than that without HEPs. This makes it inefficient for protons to transfer thermal energy to the electrons by Coulomb scattering. Thus, the electron temperature is likely to be lower, which causes the radiation spectrum from RIAFs to change significantly. However, since there are other mechanisms of electron heating in RIAFs (see Chapter 2), it is unclear whether the electron temperature becomes lower as the proton temperature becomes lower. We should formulate the accretion flows with the electron component to study this effect in detail.

The ADAF solution is considered to produce not only jets but also disk winds (see Narayan & Yi 1994; Blandford & Begelman 1999). Many studies on accretion flows with the multi-dimensional simulations show that the disk winds are very common phenomena (e.g., McKinney 2006; Ohsuga & Mineshige. 2011). The disk winds affect the mass accretion rates, angular momentum transport, and internal energy. Though it is important to include effects of the disk winds, modeling those effects in the one-dimensional model is not simple. A multi-dimensional study is necessary in order to understand the effects of the disk winds, and it remains to be addressed as a future work.

Turbulent magnetic fields in the accretion flow are related to the acceleration and diffusion process of HEPs. According to the quasi-linear theory of the wave-particle interaction, $C_{\rm diff}$ is related to the strength of the turbulent magnetic fields at the scale of the resonant wavelength. In accretion flows, turbulent magnetic fields are expected to be induced by MRI. Typically, the injection scale of the turbulent magnetic fields, which is around the scale height of the accretion flow, is about 10 orders of magnitude larger than the gyration scale of HEPs (Dermer et al. 1996). This difference between the two scales is expected to make the turbulent fields very weak at the gyration scale of HEPs. Thus, the Bohm limit that corresponds to $C_{\rm diff} = 1$ is unlikely to be suitable in the accretion flows, and we have used $C_{\rm diff} = 10^2,\ 10^4,$ and 10^6. We note that the acceleration of HEPs is inefficient for high $C_{\rm diff}$ because high $C_{\rm diff}$ means that HEPs rarely interact with the turbulent magnetic fields. From the point of view of particle acceleration, it seems difficult to produce a large amount of HEPs by stochastic acceleration

for the models with $C_{\rm diff} = 10^6$.

We assume monoenergetic HEPs in order to use the moment equations of the diffusion convection equation. Actually, HEPs have energy spectra that are determined by acceleration, escape, and cooling processes (e.g., Dermer et al. 1996). Owing to the energy dependence of the diffusion coefficient, particles with higher energy are considered to escape from the flow faster than those with lower energy. This feature likely affect the luminosity and mass-escaping rates of protons. In order to discuss the diffusive phenomena more precisely, we should model and solve the acceleration process with including the momentum dependence of HEPs.

3.4 Summary

We study the effects of HEPs on the accretion flow onto a SMBH. We also calculate the luminosities of escaping particles such as protons, neutrons, gamma rays, and neutrinos.

We formulate a one-dimensional model of the two-component accretion flow consisting of TPs and HEPs. The thermal component is governed by fluid dynamics, where we ignore the effects of radiative cooling. For HEPs, the moment equations of the diffusion-convection equation are solved with accounting for coolings by pion production, neutron escape, and proton escape. We assume that the injection rates of HEPs are related to the heating rates of TPs. We obtain steady state solutions by solving the time evolution of these equations. Without HEPs, we obtain advection-dominated solutions that have features consistent with those obtained by previous studies. Including HEPs, we also obtain advection-dominated flows, and the effects of HEPs on the flow structure turn out to be small even if the pressure of HEPs dominates over the thermal pressure. In this case, the temperature of thermal particles are much lower than that without non-thermal particles. This may have some influence on the electron temperature, although we ignore the effect in this chapter. For a model in which the escape of high-energy protons takes away almost all energy, the accretion flow has the Keplerian angular momentum, a slow infall velocity, and a high surface density. However, this

solution is incomplete in the sense that it ignores the electron component because electrons are expected to be important for the accretion flow with high surface density.

We calculate the luminosities of escaping particles for these steady solutions. For low mass accretion rates and high injection Lorentz factors of HEPs with high diffusion coefficients, the luminosity of diffusively escaping protons amounts to $L_{\rm p} \sim 10^{-2}\dot{M}c^2$. In contrast, for high mass accretion rates, the luminosity of escaping neutrons, $L_{\rm n}$, is higher than $L_{\rm p}$, and its maximum value is nearly the same as that of the protons $L_{\rm n} \sim 10^{-2}\dot{M}c^2$. The luminosities of gamma rays and neutrinos are a few times higher than $L_{\rm n}$. We note that radiative processes are expected to be important for high mass accretion rates. Though HEPs have little influence on dynamical structures, it is possible to extract some amount of energy through HEPs. They are considered to play some roles for the production of relativistic jets in terms of mass and energy injections.

Chapter 4

Neutrino and Cosmic-ray proton Emission from Hot Accretion Flows

The accretion flows onto SMBH can emit cosmic ray (CR) protons, neutrinos, and gamma rays. The IceCube collaboration reported the detection of extraterrestrial neutrinos (Aartsen et al. 2013a, 2014), and they are likely to originate from high-energy astrophysical sources. Although many models are proposed to explain the IceCube neutrinos, the origin is still controversial. In this chapter, we propose the LLAGN model as a candidate for the IceCube neutrino sources, and discuss the emission of protons and gamma rays from LLAGNs. Note that we use a different formulation of RIAF model from that described in Chapter 3. Here, we ignore the spacial distribution of accretion flow. Instead, we take the momentum distribution of non-thermal protons into account. We set up the physical quantities of RIAFs using one-zone approximation in Section 4.1. We take a momentum space into account and show the calculated neutrino and CR proton spectra from typical RIAFs in Section 4.2. The diffuse intensity of the neutrinos and CR protons are shown in Section 4.3. We discuss gamma-ray emission from LLAGNS and other AGN models in Section 4.4, and summarize the results of this chapter in Section 4.5. This chapter is based on Kimura et al. (2014b).

4.1 Physical setup

Here, we model the emission from RIAFs with a one-zone approximation, where it is assumed that particles are accelerated only within some radius R. When one considers the structure of accretion disks, the multi-dimensionality is important in general. But we consider that our approach is enough as the first step to consider high-energy neutrino emission from RIAFs. We show the schematic image of the one-zone RIAF model in Figure 4.1.Protons are accelerated through the interaction with turbulent magnetic fields in RIAFs. These protons generate pions via pp and $p\gamma$ reactions and/or escape from the flow by diffusive motion. The pions decay to gamma rays, neutrinos, electrons, and positrons. The neutrinos easily escape from the flow, while the gamma rays are likely to be absorbed through the pair production process. The electrons and positrons can also emit gamma rays, and synchrotron cascades seem to occur. We focus on the neutrinos and CR protons, and do not discuss the detail of gamma-ray spectrum in this chapter.

4.1.1 Physical quantities of RIAFs

RIAFs are the hot and rapid infall accretion flows. We set the radial velocity v_r, thermal proton density n_p, thermal pressure $P_{\rm TP}$, and strength of magnetic fields B of our RIAF model as follows,

$$v_r = \alpha v_{\rm K}, \tag{4.1}$$

$$n_p = \frac{\dot{M}}{2\pi R^2 v_r m_p}, \tag{4.2}$$

$$P_{\rm TP} = n_p \frac{GM_{\rm BH}}{3R} m_p, \tag{4.3}$$

$$B = \sqrt{\frac{8\pi P_{\rm TP}}{\beta}}, \tag{4.4}$$

where α is the alpha parameter (Shakura & Sunyaev 1973), $v_{\rm K} = \sqrt{GM_{\rm BH}/R}$ is the Keplerian velocity, $\dot{M}$ is the mass accretion rate, $M_{\rm BH}$ is the mass of the super massive black hole (SMBH),

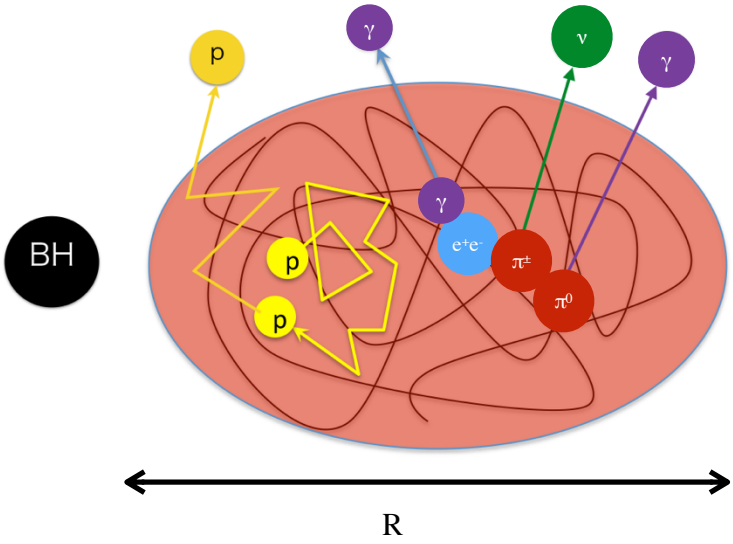

Figure 4.1: The schematic picture of our one-zone RIAF model. The protons are accelerated inside RIAFs. They generate pions through pp and $p\gamma$ reactions and/or escape from the flow by diffusive motion. The non-thermal neutrinos are produced by pion decay, and escape from the flows. The gamma rays are also produced by pion decay and synchrotron from electrons and positrons.

and β is the plasma beta parameter. We assume the scale height of the flow $H \sim R$. We normalize the radius and mass accretion rate as $\varpi = R/R_{\rm S}$ and $\dot{m} = \dot{M}/\dot{M}_{\rm Edd}$, respectively, where we use the Schwarzschild radius $R_{\rm S} = 2GM_{\rm BH}/c^2$ and the Eddington accretion rate $\dot{M}_{\rm Edd} = L_{\rm Edd}/c^2$. This makes

$$R = 2.95 \times 10^{13}\ \varpi_1 M_{\rm BH,7}\ [\rm cm], \tag{4.5}$$

$$v_r = 6.7 \times 10^{8}\ \varpi_1^{-1/2} \alpha_{-1}\ [\rm cm\ sec^{-1}], \tag{4.6}$$

$$n_p = 1.1 \times 10^{9}\ \varpi_1^{-3/2} \alpha_{-1}^{-1} M_{\rm BH,7}^{-1} \dot{m}_{-2}\ [\rm cm^{-3}], \tag{4.7}$$

$$B = 4.9 \times 10^{2}\ \varpi_1^{-5/4} \alpha_{-1}^{-1/2} \beta_3^{-1/2} M_{\rm BH,7}^{-1/2} \dot{m}_{-2}^{1/2}\ [\rm Gauss], \tag{4.8}$$

where $A_n = A/10^n$, except $M_{\rm BH,n} = M_{\rm BH}/(10^n M_\odot)$ and $\beta_3 = \beta/3$. If we consider small $\varpi \lesssim 5$, v_r and n_p is quite different from above expression because the flow becomes supersonic and particles go into the SMBH quickly (Narayan et al. 1997; Kimura et al. 2014a). In this chapter, we fix the parameters $\alpha = 0.1$, $\beta = 3$, and $\varpi = 10$ for demonstration. Note that the physical quantities of RIAFs in this chapter are slightly different from those in Chapter 2.

4.1.2 Thermal electrons and target photon fields

The photomeson production is an important process of the neutrino and/or gamma-ray production. To estimate this, we need to obtain target photon spectra.

First, one needs to know the electron temperature. Since the relaxation time between electrons and protons in RIAFs is longer than the infall time $t_{\rm fall}$ (see Section 4.2), electrons would have different temperature from that of the protons (Takahara & Kusunose 1985). The mechanism of electron heating in RIAFs is determined by details of dissipation in collisionless plasma (Quataert & Gruzinov 1999; Sharma et al. 2007; Howes 2010), but the accurate prescription for the turbulent heating is not well understood. According to Sharma et al. (2007), the electron temperature in RIAFs with $\dot{m} = 0.01$ is $\sim 5 \times 10^9$ K and little depends on the heating prescription. The dependence of electron temperature on $\dot{m}$ is not so strong, $T_e \sim 2 \times 10^{10}$ K at $\dot{m} = 10^{-4}$. In this work, for simplicity, we treat $\theta_e \equiv k_{\rm B} T_e/(m_e c^2)$ as a parameter, and consider the range of $1 \lesssim \theta_e \lesssim 4$. Then, when electrons are thermalized (Mahadevan & Quataert 1997), they obey the relativistic Maxwellian distribution,

$$N_e(\gamma_e) = n_e \frac{\gamma_e^2 \beta_e \exp(-\gamma_e/\theta_e)}{\theta_e K_2(1/\theta_e)}, \tag{4.9}$$

where n_e is the electron number density, β_e and γ_e are the velocity and the Lorentz factor of the thermal electrons, respectively, and $K_2(x)$ is the second modified Bessel function. We ignore effects of the pair production on the thermal component for simplicity, which gives $n_p = n_e$.

It has been suggested that in LLAGNs, emission comes from a jet, an outer thin disk, and a RIAF (Nemmen et al. 2006, 2014). In this chapter, we consider only radiation from

the RIAF because the radiation from the jet and the thin disk would be sub-dominant. We use one-zone approximation and calculate the photon spectrum within the acceleration radius R. Thermal electrons in the RIAF emit radiation through the synchrotron, bremsstrahlung, and inverse Compton scattering. We use fitting formulae of the emissivity of bremsstrahlung and synchrotron (Narayan & Yi 1995). Assuming the local thermodynamic equilibrium with Eddington approximation (Rybicki & Lightman 1979), we can get the photon fields from the synchrotron and bremsstrahlung. This treatment consistently includes the synchrotron self absorption (Manmoto et al. 1997). Using this photon fields as the seed photons, spectra of inverse Compton scattering are calculated. See Appendix C for details of the calculation of the target photon fields.

Figure 4.2 shows target photon spectra in RIAFs for models A1, A2, and A3, whose parameters are tabulated in Table 4.1 (where the parameter ζ will be introduced in Section 4.2). We fix the parameters $\alpha = 0.1$, $\beta = 3$, $\varpi = 10$, and $\theta_e = 2.0$. For the reference model A1, the synchrotron component has a peak at $E_\gamma \sim 0.03$ eV. The thermal electrons scatter seed synchrotron photons efficiently, and make a few peaks from the infrared to soft X-ray range. Multiple-scattered photons may make almost flat spectrum for hard X-ray range. The spectrum has a cutoff corresponding to the electron temperature. The inverse Compton scattering dominates over the bremsstrahlung in all the frequency range for A1.

The efficiency of the inverse Compton scattering depends on y parameter, $y \sim n_e \sigma_{\rm T} R \theta_e^2 \propto \dot{m} \varpi^{-1/2} \alpha^{-1} \theta_e^2$, where $\sigma_{\rm T}$ is the Thomson cross section. Low $\dot{m}$ makes the y parameter low, so that the spectrum by the inverse Compton scattering is soft. This causes that bremsstrahlung is dominant at hard X-ray range. For A2, y parameter is less than unity, and the bremsstrahlung dominates over the inverse Compton in $E_\gamma \gtrsim 2 \times 10^4$ eV. The y parameter is independent of $M_{\rm BH}$ in our formulation. The high $M_{\rm BH}$ makes luminosity higher due to large R and high $\dot{M}$. It also makes the synchrotron peak frequency low because of weak B. The profile of the spectrum for A3 is similar to that for A1 but the luminosity for A3 is about ten times higher than that for A1.

Table 4.1: Model parameters for the spectrum from a LLAGN

model	$\dot{m}$	$M_{\rm BH}[M_\odot]$	ζ
A1 (reference)	10^{-2}	10^7	0.1
A2	10^{-3}	10^7	0.1
A3	10^{-2}	10^8	0.1
A4	10^{-2}	10^7	0.3

4.2 Spectra of non-thermal particles in a typical RIAF

4.2.1 Plasma in accretion flows

If the infall time $t_{\rm fall}$ is shorter than the relaxation time due to the Coulomb scattering $t_{\rm rel}$, it allows the existence of non-thermal particles. The infall time for RIAFs is estimated to be

$$t_{\rm fall} \simeq \frac{R}{v_r} \sim 4.4 \times 10^4 \varpi_1^{3/2} \alpha_{-1}^{-1} M_{\rm BH,7}\ [\rm s], \tag{4.10}$$

whereas the relaxation time is estimated as

$$\begin{aligned} t_{\rm rel} &= \frac{4\sqrt{\pi}}{\ln\Lambda} \frac{1}{n_p \sigma_{\rm T} c} \left(\frac{m_p}{m_e}\right)^2 \left(\frac{k_{\rm B} T_p}{m_p c^2}\right)^{3/2} \\ &\sim 2.1 \times 10^7 \alpha_{-1} M_{\rm BH,7} \dot{m}_{-2}^{-1}\ [\rm sec] \end{aligned} \tag{4.11}$$

where $\ln\Lambda$ is the Coulomb logarithm (e.g., Spitzer 1962). Thus, RIAFs satisfy $t_{\rm rel} \gg t_{\rm fall}$, which allows $F(p)$ to be non-thermal (cf., Takahara & Kusunose 1985; Mahadevan & Quataert 1997). For RIAFs, $t_{\rm fall}$ has the same order as the dissipation time via the α viscosity $t_{\rm dis}$ (e.g., Pringle 1981). Thus, the proton distribution function in RIAFs may not be Maxwellian within the dissipation time.

The protons inside RIAFs are scattered by turbulent magnetic fields. This process changes a momentum of each proton whose distribution function may be different from Maxwellian. In this chapter, we consider relativistic protons in RIAFs, assuming that they are governed by

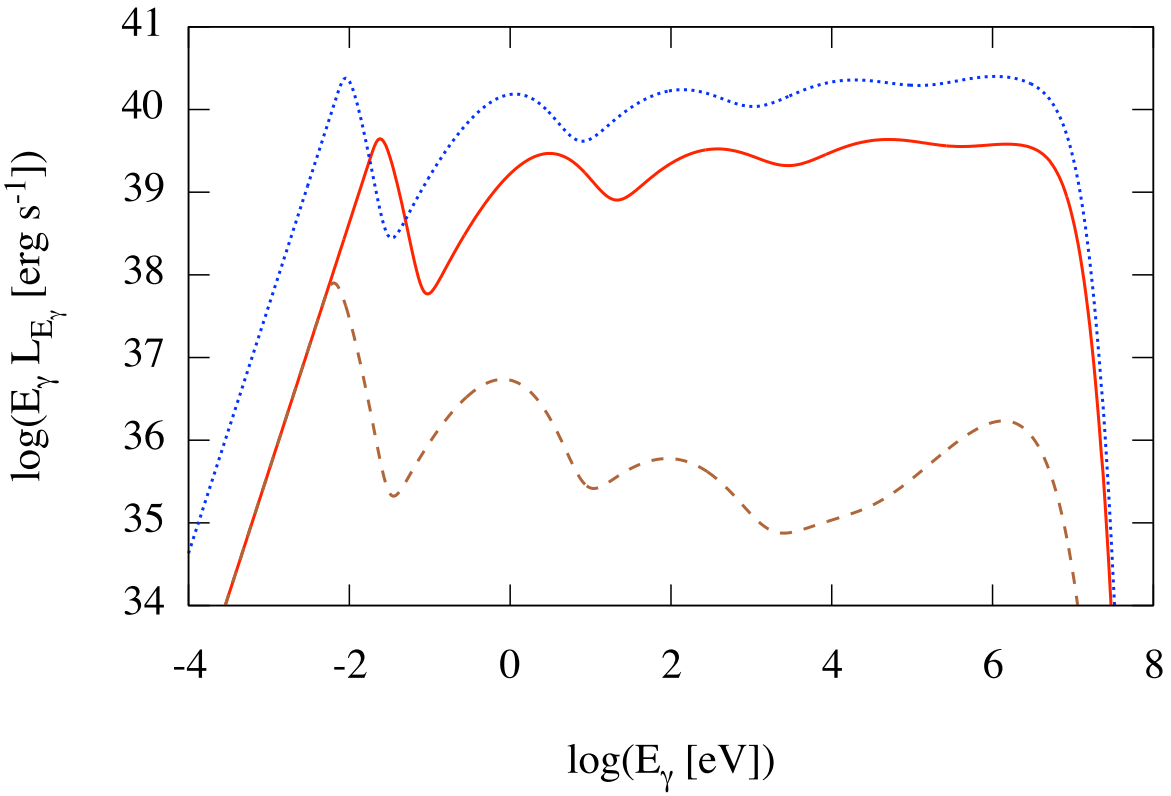

Figure 4.2: Target photon spectra emitted by thermal electrons in RIAFs. The red-solid, the brown-dashed, and blue-dotted lines show models A1 (reference), A2 (low $\dot{m}$), A3 (high $M_{\rm BH}$), respectively. The target photon spectrum for model A4 is the same with that for A1. This figure is reproduced from Kimura et al. (2014b), by permission of the American Astronomical Society.

the Fokker-Planck equation (e.g., Stawarz & Petrosian 2008)

$$\frac{\partial}{\partial t}F(p) = \frac{1}{p^2}\frac{\partial}{\partial p}\left[p^2\left(D_p\frac{\partial}{\partial p}F(p) + \frac{p}{t_{\rm cool}}F(p)\right)\right] - \frac{F(p)}{t_{\rm esc}} + \dot{F}_{\rm inj}, \tag{4.12}$$

where $F(p)$ is the distribution function of the non-thermal protons, p is the momentum of the protons, D_p is the diffusion coefficient for the momentum space, $\dot{F}_{\rm inj}$ is the injection term, $t_{\rm cool}$ is the cooling time, and $t_{\rm esc}$ is the escaping time. The escaping time consists of both diffusive escape and infall to the black hole. We do not consider non-thermal electrons because electrons

have much shorter relaxation time than protons. They become thermalized within infall time when $\dot{m} \gtrsim 10^{-4}$ (Mahadevan & Quataert 1997).

It is considered that quasars have standard disks, in which the physical quantities are much different from those in RIAFs. For the Shakura-Sunyaev disks in the gas pressure dominant regime (gas-SSD, Shakura & Sunyaev 1973), we have longer $t_{\rm fall}$ ($t_{\rm fall} = R/v_r \simeq R/(\alpha v_{\rm K})(R/H)^2 \sim 3 \times 10^8$ sec), and shorter $t_{\rm rel}$ ($\sim 3 \times 10^{-9}$ sec $\ll t_{\rm dis}$) than those of RIAFs. The dissipation time $t_{\rm dis}$ is the same as that of RIAFs (see Equation [4.10]). Thus, $t_{\rm rel} \ll t_{\rm dis} \ll t_{\rm fall}$ is satisfied in gas-SSDs. The distribution function $F(p)$ is expected to be Maxwellian due to the efficient Coulomb scattering.

Note that if we consider relativistic particles, we should compare the Coulomb loss time for relativistic particles $t_{\rm Coul}$ to $t_{\rm dis}$. The Coulomb loss time is estimated to be (e.g., Dermer et al. 1996)

$$t_{\rm Coul} \sim 1225 \frac{(\gamma_p - 1)(3.8\theta_e^{3/2} + 1.0)}{\tau_{\rm T} \ln \Lambda} \frac{R}{c}, \tag{4.13}$$

where γ_p is the Lorentz factor of the proton and $\tau_{\rm T}$ is the optical depth to Thomson scattering. Since $\tau_{\rm T} < 0.1$ for RIAFs, $t_{\rm Coul} > t_{\rm dis}$ is satisfied for $\gamma_p \gtrsim 2$. Thus, the Coulomb loss is unimportant in RIAFs. On the other hand, for gas-SSDs, the Coulomb loss time is much shorter than the dissipation time for $\gamma_p \lesssim 10^3$ because they have $\tau_{\rm T} \sim 10^4$. Therefore, it seems difficult to accelerate the particles in gas-SSDs. For other solutions, such as standard disks in the radiation pressure dominant regime (Shakura & Sunyaev 1973) and magnetically arrested disks (Bisnovatyi-Kogan & Ruzmaikin 1974), the Thomson optical depth may not be as high as gas-SSDs, and it might be possible to satisfy $t_{\rm dis} < t_{\rm Coul}$.

4.2.2 Timescales

Equation (4.12) involves three important timescales, the acceleration time $t_{\rm accel} \equiv p^2/D_p$, the escape time $t_{\rm esc}$, and the cooling time $t_{\rm cool}$.

In this chapter, we assume a power spectrum $P(k) \propto k^{-q}$, and fix the index of the power

spectrum $q = 5/3$ for simplicity. This value is motivated by the Alfvénic turbulence (Goldreich & Sridhar 1995), although other modes may also play an important role on particle acceleration. According to the quasi-linear theorem, the diffusion coefficient is (e.g., Dermer et al. 1996)

$$D_p \simeq (m_p c)^2 (c k_{\rm min}) \left(\frac{v_{\rm A}}{c}\right)^2 \zeta (r_L k_{\rm min})^{q-2} \gamma_p^q, \tag{4.14}$$

where $k_{\rm min} \sim R^{-1}$ is the minimum wave number of the turbulence, $v_{\rm A} = B/\sqrt{4\pi m_p n_p}$ is the Alfven speed, $r_L = m_p c^2/(eB)$, γ_p is the Lorentz factor of protons, and $\zeta = 8\pi \int P(k) dk / B_0^2$ is the ratio of the strength of turbulent fields to that of the non-turbulent fields. Then, the acceleration time is

$$\begin{aligned} t_{\rm accel} &\simeq \frac{p^2}{D_p} \simeq \frac{1}{\zeta} \left(\frac{v_{\rm A}}{c}\right)^{-2} \frac{R}{c} \left(\frac{r_L}{R}\right)^{2-q} \gamma_p^{2-q} \\ &\sim 1.1 \times 10^3 \varpi_1^{25/12} \alpha_{-1}^{1/6} \beta_3^{7/6} M_{\rm BH,7}^{5/6} \dot{m}_{-2}^{-1/6} \zeta_{-1}^{-1} \gamma_{p,1}^{1/3} \ [\rm sec]. \end{aligned} \tag{4.15}$$

We consider diffusion and infall as the escape from the given zone, and write the escaping rate as

$$t_{\rm esc}^{-1} = t_{\rm fall}^{-1} + t_{\rm diff}^{-1}, \tag{4.16}$$

The particles fall to the SMBH in the infall time, given by Equation (4.10). For isotropically turbulent magnetic fields, the diffusion time is (e.g., Stawarz & Petrosian 2008)

$$\begin{aligned} t_{\rm diff} &\simeq \frac{9R}{c} \zeta \left(\frac{r_L}{R}\right)^{q-2} \gamma_p^{q-2} \\ &\sim 6.7 \times 10^5 \varpi_1^{11/12} \alpha_{-1}^{-1/6} \beta_3^{-1/6} M_{\rm BH,7}^{7/6} \dot{m}_{-2}^{1/6} \zeta_{-1}^{1} \times \gamma_{p,1}^{-1/3} \ [\rm sec]. \end{aligned} \tag{4.17}$$

In this chapter, we neglect escape of neutrons and reaction of the neutrons because they are sub-dominant in our models.

For the cooling time, we consider inelastic pp and $p\gamma$ reactions, and the proton synchrotron emission process. The total cooling rate is given as

$$t_{\rm cool}^{-1} = t_{pp}^{-1} + t_{p\gamma}^{-1} + t_{\rm sync}^{-1}, \tag{4.18}$$

where t_{pp}, $t_{p\gamma}$, and $t_{\rm sync}$ are cooling time scales for each process. We neglect the inverse Compton scattering by protons and the Bethe-Heitler process because they are typically sub-dominant. The synchrotron cooling rate is

$$t_{\rm sync}^{-1} = \frac{4}{3}\left(\frac{m_e}{m_p}\right)^3 \frac{c\sigma_{\rm T}U_B}{m_e c^2}\gamma_p, \tag{4.19}$$

where $U_B = B^2/(8\pi)$ is the energy density of the magnetic fields. The pp cooling rate is

$$t_{pp}^{-1} = n_p \sigma_{pp} c K_{pp}, \tag{4.20}$$

where $K_{pp} \sim 0.5$ is the proton inelasticity of the process. The total cross section of this process σ_{pp} is represented as a function of the proton energy E_p,

$$\sigma_{pp} \simeq (34.3 + 1.88L + 0.25L^2)\left[1 - \left(\frac{E_{pp,\rm thr}}{E_p}\right)^4\right]^2 [\rm mb]$$

for $E_p \geq E_{pp,\rm thr}$, where $L = \log(E_p/1{\rm TeV})$ and $E_{pp,\rm thr}$ =1.22 GeV (Kelner et al. 2006). The $p\gamma$ cooling rate is

$$t_{p\gamma}^{-1} = \frac{c}{2\gamma_p^2}\int_{\bar{\varepsilon}_{\rm thr}}^{\infty} d\bar{\varepsilon}\sigma_{p\gamma}(\bar{\varepsilon})K_{p\gamma}(\bar{\varepsilon})\bar{\varepsilon}\int_{\bar{\varepsilon}/(2\gamma_p)}^{\infty} dE_\gamma \frac{N_\gamma(E_\gamma)}{E_\gamma^2}, \tag{4.21}$$

where $\bar{\varepsilon}$ and E_γ are the photon energy in the proton rest frame and the black hole frame, respectively, $N_\gamma(E_\gamma)$ is the photon occupation number, and $\bar{\varepsilon}_{\rm thr}$ =145 MeV. We use the rectangular approximation for this process (Stecker 1968). Assuming $\sigma_{p\gamma}(\bar{\varepsilon})K_{p\gamma}(\bar{\varepsilon}) = \delta(\bar{\varepsilon}-\bar{\epsilon}_{\rm pk})\sigma_{\rm pk}K_{\rm pk}\Delta\bar{\epsilon}_{\rm pk}$, we write $t_{p\gamma}$ as

$$t_{p\gamma}^{-1} = \frac{c}{2\gamma_p^2}\bar{\epsilon}_{\rm pk}\Delta\bar{\epsilon}_{\rm pk}\sigma_{\rm pk}K_{\rm pk}\int_{\bar{\epsilon}_{\rm pk}/(2\gamma_p)}^{\infty} dE_\gamma \frac{N_\gamma(E_\gamma)}{E_\gamma^2}, \tag{4.22}$$

where $\bar{\epsilon}_{\rm pk} \sim 0.3$ GeV, $\sigma_{\rm pk} \sim 5\times10^{-28}$ cm^2, $K_{\rm pk} \sim 0.2$, $\Delta\bar{\epsilon}_{\rm pk} \sim 0.2$ GeV.

Figure 4.3 shows the timescales for models A1, A2, A3, and A4, whose parameters are tabulated in Table 4.1. For low values of E_p, $t_{\rm accel}$ is the shortest for all the models. At some energy $E_{p,\rm eq}$, $t_{\rm accel} = t_{\rm esc}$ is satisfied. Above the energy, where $t_{\rm esc} < t_{\rm accel}$, the acceleration

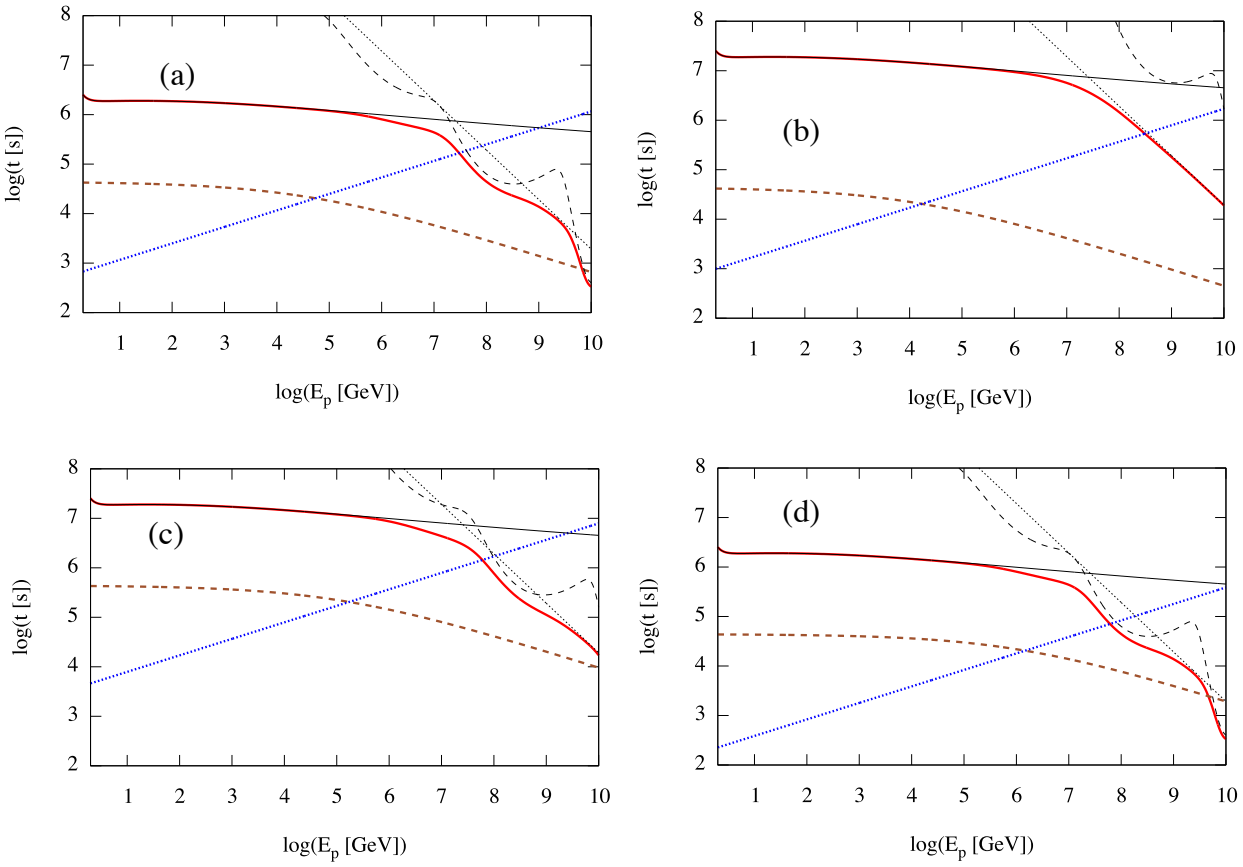

Figure 4.3: Energy dependence of the timescales. We plot the cooling time (thick-red-solid), the escape time (thick-brown-dashed), and the acceleration time (thick-blue-dotted). The thin-solid, thin-dashed, and thin-dotted lines show the t_{pp} ,$t_{p\gamma}$, and $t_{\rm sync}$, respectively. Panels (a), (b), (c), (d) show the cases for models A1 (reference), A2 (low $\dot{m}$), A3 (high $M_{\rm BH}$), and A4 (high ζ), respectively. This figure is reproduced from Kimura et al. (2014b), by permission of the American Astronomical Society.

is limited by escape. Since $t_{\rm diff}$ is shorter than $t_{\rm fall}$ at $E_{p,\rm eq}$, we can roughly estimate it by

equating $t_{\rm diff}$ and $t_{\rm accel}$,

$$\begin{aligned}\gamma_{p,\rm eq} &\sim \left(\frac{3\zeta v_{\rm A}}{c}\right)^3 \left(\frac{R}{r_L}\right) \\ &\sim 1.4\times10^5 \dot{m}_{-2}^{1/2} M_{\rm BH,7}^{1/2} \alpha_{-1}^{1/2} \zeta_{-1}^3 \beta_3^{-2} \varpi_1^{-7/4}. \end{aligned} \tag{4.23}$$

This characteristic energy strongly depends on ζ. The higher $\dot{m}$ or lower β makes the magnetic fields stronger, so that the $\gamma_{p,\rm eq}$ is higher. The larger ϖ weakens B, which leads to lower $\gamma_{p,\rm eq}$. The estimation in Equation (4.23), where the infall time is neglected, gives 2-3 times higher value than $E_{p,\rm eq}$ (which can be seen in Figure 4.3), but the parameter dependence in Equation (4.23) is correct as long as we choose $\beta \lesssim 5$. We note that $E_{p,\rm eq}$ does not correspond to the peak energy of the $E_p L_{E_p}$ spectrum (see the next subsection). When diffusive escape limits acceleration, the distribution function declines gradually above $E_{p,\rm eq}$ and asymptotes to $F(p) \propto E_p^{1/2} \exp(-(27E_p/E_{p,\rm eq})^{1/3})$ for $q = 5/3$ (Becker et al. 2006). This allows the protons to have about 10 times higher energy than the estimate in Equation (4.23). Thus, LLAGNs can have the protons up to $E_p \gtrsim 10^{16}$ eV when $\zeta \gtrsim 0.2$.

For all the models, at low energies, *pp* inelastic collisions dominate over synchrotron and the photomeson production processes. At high energies, the photomeson production is dominant for A1, A3, and A4 (high $\dot{m}$), whereas the synchrotron cooling is the most efficient for A2 (low $\dot{m}$). This is simply because the number density of target photons strongly depend on $\dot{m}$. Other parameters do not strongly affect this qualitative feature of cooling time scales.

4.2.3 Spectra of non-thermal particles

When we solve Equation (4.12), we treat the injection term as a delta-function $\dot{F}_{\rm inj} = F_0 \delta(p - p_{\rm inj})$, where $p_{\rm inj}$ is the injection proton momentum and F_0 is the normalization factor of injection. We fix $p_{\rm inj} = 2m_p c$ because $p_{\rm inj}$ little affects the profile of distribution function as long as we choose $p_{\rm inj} c \ll E_{p,\rm eq}$. We assume that the total luminosity expended to inject and accelerate relativistic protons is proportional to the released luminosity by accretion, $L_{\rm accrt} \sim \dot{M}c^2$. As seen in the previous subsection, the proton acceleration is limited by escape. We determine

the normalization of relativistic protons such that the luminosity of injection and acceleration balances with the escape luminosity, i.e.,

$$\eta_{\rm cr}\dot{M}c^2 = \int dV \int dp \frac{4\pi p^2 F(p) E_p}{t_{\rm esc}}, \tag{4.24}$$

where $\eta_{\rm cr}$ is a parameter of injection efficiency. This parameter determines the normalization of the non-thermal protons, not affecting the shapes of the spectra. Kimura et al. (2014a) shows that the non-thermal particles do not affect the dynamical structure if $\eta_{\rm cr} \lesssim 0.1$. We use $\eta_{\rm cr} = 0.01$ as a fiducial value.

We solve Equation (4.12) until steady solutions are realized by using the Chang-Cooper method (Chang & Cooper 1970). See Appendix D for the test calculation of the Fokker-Planck equation. We set the computational region from $E_p = 1.5$ GeV to 10^{10} GeV and divide the grids such that they are uniform in the logarithmic space. The number of the grid points is $N = 500$. We calculate some models with $N = 1000$ and find that the results are unchanged by the number of grids.

Since the peak energy is determined by CR escape for all the models, the profiles of the distribution functions are quite similar to each other. They show a power law $F(p) \propto E_p^{-(1+q)}$ for low E_p. For $E_p > E_{p,\rm eq}$, they deviate from the power-law and decrease gradually, compared to the exponential cutoff. After obtaining $F(p)$, we estimate the differential luminosity spectra of the escaping protons to be

$$E_p L_{E_p} = \int dV \frac{4\pi p^3 F(p) E_p}{t_{\rm diff}} = \frac{4\pi^2 c R^3 p^4 F(p)}{t_{\rm diff}}. \tag{4.25}$$

We plot $E_p L_{E_p}$ in Figure 4.4. We tabulate parameter sets in Table 4.1, fixing the parameters $\alpha = 0.1$, $\beta = 3$, $r = 10$, $\theta_e = 2.0$, $q = 5/3$, and $\eta_{\rm cr} = 0.01$. For A1, the luminosity reaches $\sim 3\times10^{40}$ erg s^{-1}. Since the total luminosity of escaping protons is proportional to the released energy $\dot{M}c^2$, the peak luminosity of escaping protons is almost proportional to $\dot{m}$ and $M_{\rm BH}$ (see A2 and A3 in Figure 4.4), while it is almost independent of other parameters. All the models have a power law, $E_p L_{E_p} \propto E_p^{5-2q}$, for $E_p < E_{p,\rm eq}$. For $E_p > E_{p,\rm eq}$, the spectra deviate from the

power law, and asymptote to $\propto E_p^{17/6}\exp(-(27E_p/E_{p,\rm eq})^{1/3})$ (Becker et al. 2006). This makes a peak at the energy $E_{p,\rm pk}\sim 30E_{p,\rm eq}$. The parameter dependence of $E_{p,\rm pk}$ is consistent with the estimation by Equation (4.23).

The neutrino spectrum is estimated to be

$$E_\nu L_{E_\nu} = \left(\frac{1}{2t_{pp}}+\frac{3}{8t_{p\gamma}}\right)4\pi p^3 E_p F(p), \tag{4.26}$$

where $E_\nu = 0.05E_p$ is the neutrino energy. As long as the pp reaction is the dominant process of neutrino production, this treatment becomes invalid for spectra that are harder than $F(p)\propto p^{-2.5}-p^{-2.7}$ (e.g., Kelner et al. 2006). Since we expect hard proton spectra $F(p)\propto p^{-(1+q)}$ with $q=5/3$, our analytical method to calculate neutrino spectra will not be accurate at low energies. Thus, we show neutrino spectra only at $E_\nu > 1$ TeV energies.

Figure 4.5 depicts spectra of neutrinos. The neutrinos are mainly made via the pp collisions for A1, A2, A3, because $t_{pp} < t_{p\gamma}$ for $E_p \lesssim E_{p,\rm pk}$. The pp cooling rate is almost independent of the proton energy. Thus, neutrino spectra are similar to those of protons unless proton spectra are too hard. The neutrino luminosity at the peak is estimated to be $E_\nu L_{E_\nu}|_{E_{\nu,\rm pk}}\propto \eta_{\rm cr}\dot{m}^2 M_{\rm BH}\alpha^{-1}\beta^{1/2}$, where $E_{\nu,\rm pk}=0.05E_{p,\rm pk}$ is the peak neutrino energy. We can see this feature in Figure 4.5 by comparing the dotted lines. On the other hand, both the pp and $p\gamma$ processes are important for A4. The photomeson production is dominant for $E_\nu \gtrsim 10^6$ GeV in A4. This makes another peak in the spectra for A4 because the $p\gamma$ neutrino spectrum reflects the target photon spectrum. For example, in A4, the target photon field has a bump made by the inverse Compton scattering at $E_\gamma\sim 2$ eV, which leads to a peak in the neutrino spectrum at $E_\nu\sim 3\times 10^6$ GeV.

Since proton acceleration is limited by escape in our models, the total injection luminosity is almost the same as the CR escape luminosity. This allows us to write the efficiency of pion production as

$$f_\pi \approx t_{\rm esc}\left(t_{pp}^{-1}+t_{p\gamma}^{-1}\right). \tag{4.27}$$

If $t_{pp} < t_{p\gamma}$ and $t_{\rm diff} < t_{\rm fall}$ at $E_{p,\rm eq}$, we can write the parameter dependence of pion production

efficiency at $E_{p,\mathrm{eq}}$ as $f_\pi \propto \dot{m}\alpha^{-1}\beta^{1/2}$. Thus, LLAGNs with high $\dot{m}$ can emit neutrinos more efficiently than those with low $\dot{m}$. On the other hand, we cannot simply write down the parameter dependence of neutrino luminosity for $p\gamma$ dominant cases because it depends on the target photon spectrum. The efficiency of pion production is $f_\pi \sim 0.02$ for A1 (pp dominant) while $f_\pi \sim 0.08$ for A4 ($p\gamma$ dominant). These values mean that most of the high-energy protons escape from RIAFs without losing their energies.

If we consider models that have high θ_e, ζ, and $\dot{m}$, compared to A1, CR acceleration is limited by the photomeson production because high ζ increases t_{diff}, and high $\dot{m}$ or θ_e decreases $t_{p\gamma}$. In this case, the scaling of the peak energy is different from the one obtained with Equation (4.23), and proton spectra could change (see, e.g., Stawarz & Petrosian 2008). However, this parameter range looks extreme in our model. High $\dot{m}$ and θ_e lead to high photon luminosities $\int L_\gamma dE_\gamma \sim L_{\mathrm{Edd}}$, which are inconsistent with the concept of RIAFs. In addition, ζ should be sufficiently less than unity for the validity of the quasi-linear theory. Thus, we can focus on the escape limit cases.

4.3 Diffuse intensities of neutrinos and cosmic-ray protons

The diffuse neutrino intensity from extragalactic sources is given by (e.g., Alvarez-Muniz & Mészáros 2004; Murase et al. 2014)

$$\Phi_\nu = \frac{c}{4\pi H_0}\int_0^{z_{\max}} \frac{dz}{\sqrt{\Omega_M(1+z)^3+\Omega_\Lambda}} \times \int_{L_{\min}}^{L_{\max}} dL_X \varphi(L_X,\ z)\frac{L_{E'_\nu}(L_X)}{E'_\nu}, \tag{4.28}$$

where $\varphi(L_X, z)$ is the luminosity function, $E'_\nu = (1+z)E_\nu$ is the neutrino energy at the rest flame of LLAGNs. We assume that LLAGNs exist from $z = 0$ to $z = z_{\max}$ and from $L_{\min}$ to $L_{\max}$.

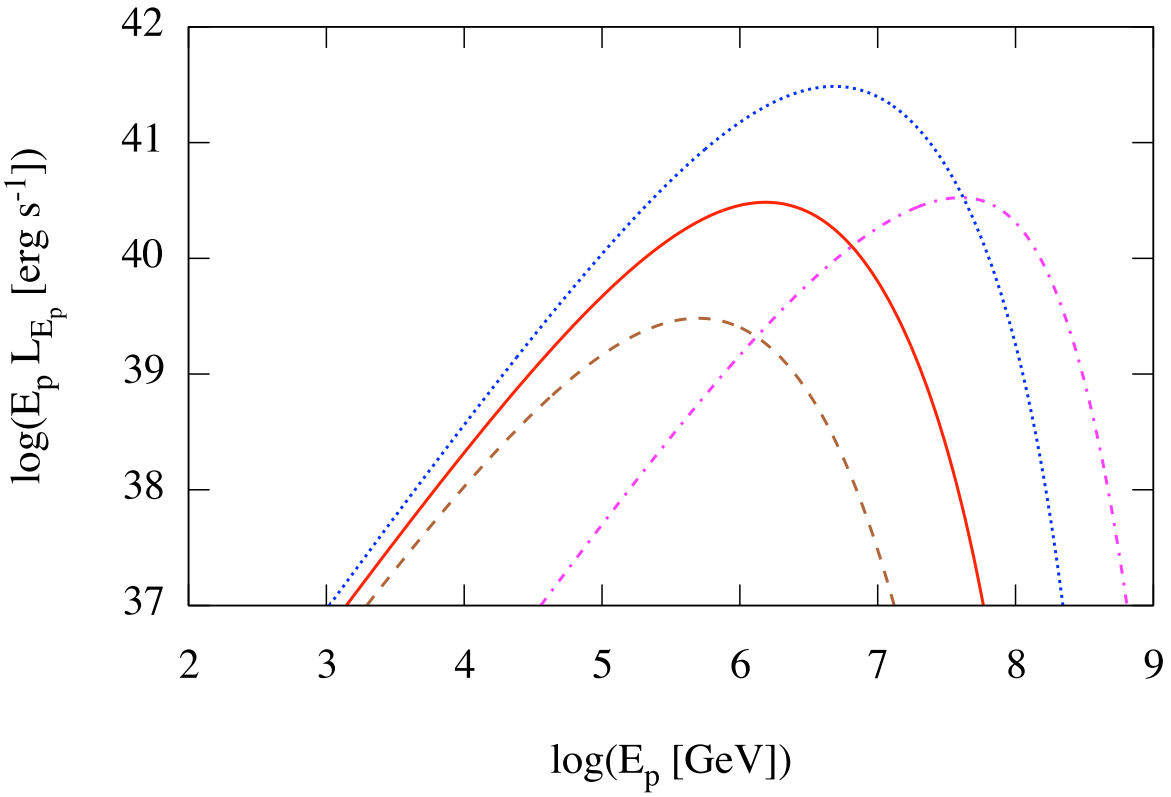

Figure 4.4: Differential luminosity spectra of escaping protons for models A1 (red-solid), A2 (brown-dashed), A3 (blue-dotted), and A4 (magenta-dot-dashed), respectively. This figure is reproduced from Kimura et al. (2014b), by permission of the American Astronomical Society.

The luminosity function of H_α from nearby LLAGNs is plotted in Ho (2008). Here we assume a broken power law shape,

$$\varphi_0(L_{H_\alpha}) = \frac{n_*/L_*}{(L_{H_\alpha}/L_*)^{s_1} + (L_{H_\alpha}/L_*)^{s_2}}. \tag{4.29}$$

From Figure 8 of Ho (2008), we find $L_* = 10^{38}$ erg s^{-1}, $n_* \sim 1.3\times10^{-2}$Mpc^{-3}, $s_1 \sim 1.64$, $s_2 \sim 1$ between 3×10^{36} erg s^{-1} $< L_{H_\alpha} < 3\times10^{41}$ erg s^{-1}. For LLAGNs, L_{H_α} is related to L_X in 2-10 keV as $L_X \sim 5L_{H_\alpha}$ (Ho 2008). Since the redshift evolution is poorly known, we assume no evolution of the luminosity function $\varphi(L_X, z) = \varphi_0(L_X)$. This is because LLAGNs are similar

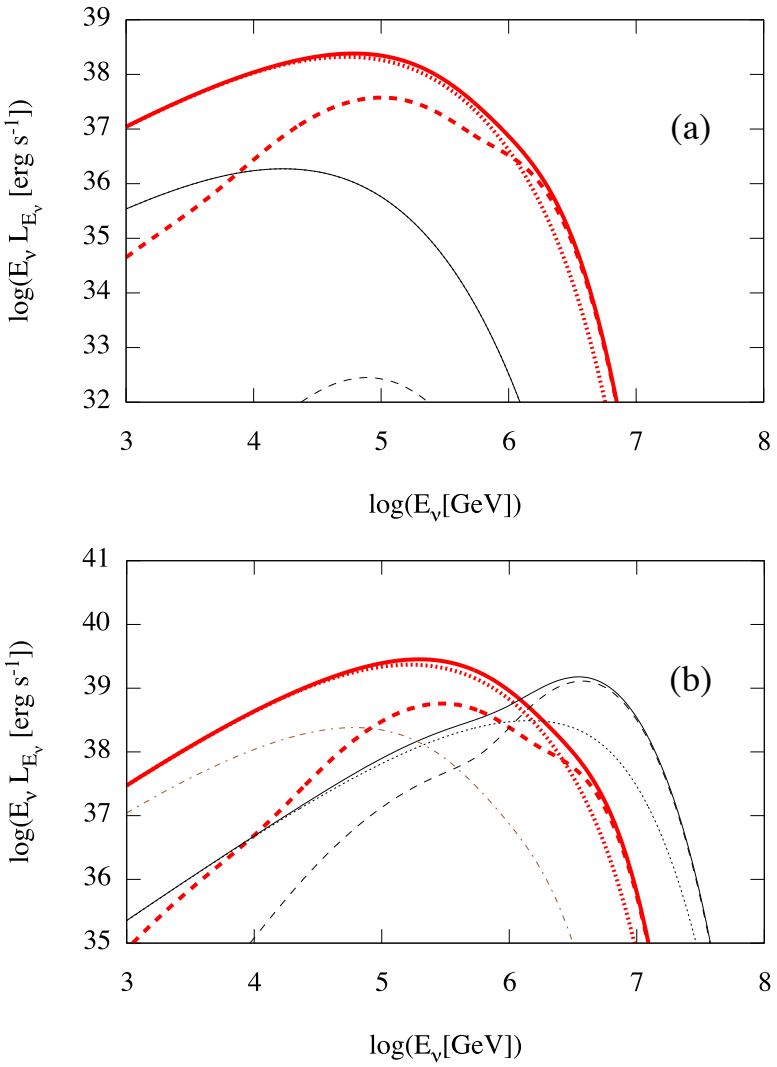

Figure 4.5: Differential luminosity spectra of neutrinos. The solid lines represent the total neutrino spectra. The dotted and dashed lines show the neutrino spectra from pp and $p\gamma$ interactions, respectively. Panel (a) shows the models A1 (red-thick lines) and A2 (black-thin lines). Panel (b) shows the models A3 (red-thick lines) and A4 (black-thin lines). The thin-dot-dashed line (total spectra for A1) is also plotted for comparison in Panel (b). This figure is reproduced from Kimura et al. (2014b), by permission of the American Astronomical Society.

to the BL Lac objects in the sense that they have a faint disk component. The luminosity function of BL Lac objects is nearly consistent with no evolution (Ajello et al. 2014).

In our RIAF model, we can obtain photon spectra from the thermal electrons, and thereby calculate L_X for given $M_{\rm BH}$, θ_e, and $\dot{m}$, as described in Section 4.1. We assume that LLAGNs have the same values of $M_{\rm BH}$ and θ_e, and then we can relate $\dot{m}$ to L_X. Then, we can integrate Equation (4.28), using the relationship. We adopt $\dot{m}_{\rm min} = 10^{-4}$ but the detailed value of $\dot{m}_{\rm min}$ little affects the results. Since $\varphi_0(H_\alpha)$ has a cutoff at $L \sim 3 \times 10^{41}$ erg s^{-1} (Hao et al. 2005; Ho 2008), we set $L_{\rm max} \sim 1.5 \times 10^{42}$ erg s^{-1}. We calculate the diffuse spectra with some values of $z_{\rm max}$ and confirm that $z_{\rm max}$ does not affect the results if we use sufficiently high value, such as $z_{\rm max} \gtrsim 4$. Recent studies show that the number density of $M_{\rm BH}$ is high at $M_{\rm BH} \sim 10^7 M_\odot$ and monotonically decreases with $M_{\rm BH}$ (e.g., Li et al. 2011). On the other hand, it seems that the average of $M_{\rm BH}$ of nearby LLAGNs whose multi-band spectra are observed is $\sim 10^8 M_\odot$ (Eracleous et al. 2010). This suggests that the average mass of SMBHs in LLAGNs is not so clear. We calculate two cases for $M_{\rm BH} = 10^7 M_\odot$ and $M_{\rm BH} = 10^8 M_\odot$. We fix $q = 5/3$, $\alpha = 0.1$, $\beta = 3$, and $\varpi = 10$, and search suitable θ_e, ζ, and $\eta_{\rm cr}$ to see if the calculated spectra explain the observed neutrino spectrum.

4.3.1 Diffuse intensity of neutrinos

In this subsection, we show that our models can fit spectra of PeV neutrinos observed by IceCube (Aartsen et al. 2014). Recently, IceCube reported neutrino spectra around 10 TeV (Aartsen et al. 2015). The flux around 10 TeV is higher than that at PeV energies. Although it may be premature to discuss the origin of this low-energy excess, we show that it is possible for LLAGNs to explain this low-energy excess.

The results are plotted in Figure 4.6, whose parameter sets are tabulated in Table 4.2. It is possible to fit the diffuse neutrino flux with reasonable parameters. In view of the PeV neutrino observation, protons must be accelerated up to around several tens of PeV energies, and their spectra cannot be extended to higher energies. This is feasible unless ζ is somehow very low.

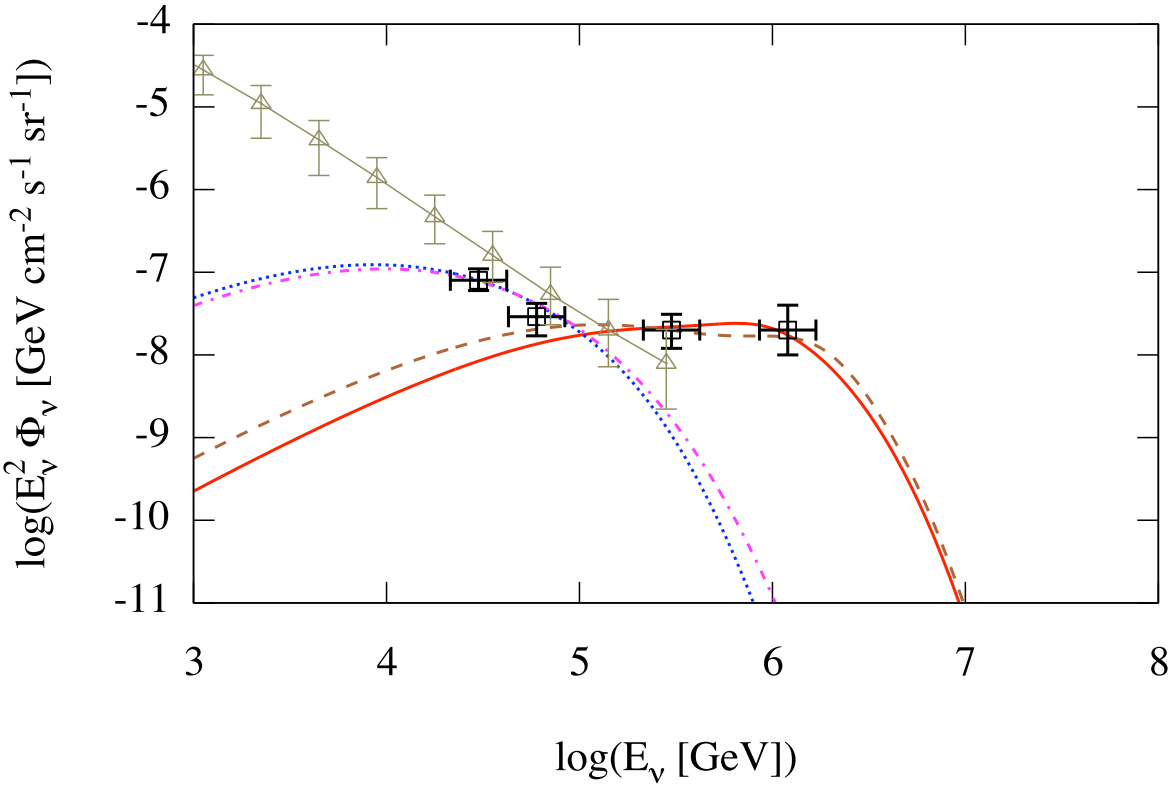

Figure 4.6: The diffuse neutrino intensity (per flavor) from RIAFs in the LLAGN model. The red-solid, brown-dashed, blue-dotted, and magenta-dot-dashed lines show the diffuse neutrino flux for B1, B2, B3, and B4, respectively. The green triangles represent the atmospheric muon neutrino background produced by CRs from Table II of Abbasi et al. (2011). The black squares show the observed data of neutrino signals from Figure 12 of Aartsen et al. (2015). This figure is reproduced from Kimura et al. (2014b), by permission of the American Astronomical Society.

The spectral shape is affected by θ_e and ζ, because these two parameters determine whether the photomeson production is important or not. The injection efficiency $\eta_{\rm cr}$ just determines the normalization of the diffuse neutrino flux, and we found that $\eta_{\rm cr} \sim 0.01$ is needed. The spectra for B1 and B2 can fit the data at 100-1000 TeV energies, although we have difficulty in explaining the 10-100 TeV neutrino flux at the same time. They are almost flat for 100 TeV $\lesssim E_\nu \lesssim$ 1000 TeV and have a cutoff at $E_\nu \sim 1000$ TeV. We can also fit the data of 10 TeV neutrinos with lower values of ζ (B3 and B4). They have a peak at $E_\nu \sim 10$ TeV and gradually decrease for $E_\nu > 10$ TeV. The photomeson production is ineffective in these cases because of the lack of target photons.

The diffuse neutrino flux is dominated by LLAGNs with high $\dot{m}$ in our model. The neutrino luminosity is higher as $\dot{m}$ higher, while the number density of LLAGNs is lower as $\dot{m}$ higher. The former is more efficient than the latter for the neutrino luminosity. We show the contribution to the total intensity from different luminosity bins in Figure 4.7. We set the luminosity bins as a faint part $L_{\rm min} < L_X < L_*$, a middle part $L_* < L_X < L_{\rm mid}$, and a luminous part $L_{\rm mid} < L_X < L_{\rm max}$, where $L_{\rm mid} = \sqrt{L_{\rm max} L_*} \sim 2.7 \times 10^{40}$. The luminous part emits most of the 100 - 1000 TeV neutrinos for B1 and B2 because the $p\gamma$ reaction makes the pion production efficiency high at high E_ν. On the other hand, for B3 and B4, the middle part contributes as much as the luminous part. The faint part little contributes to the diffuse neutrino flux for all the models. The required injection efficiency $\eta_{\rm cr} \sim 0.01$ is low, compared to the other AGN models (cf., Alvarez-Muniz & Mészáros 2004; Murase et al. 2014), although 10-100 TeV neutrinos need slightly higher $\eta_{\rm cr}$ than 100-1000 TeV ones.

Although each model cannot fit both 10-100 TeV and 100-1000 TeV data simultaneously, it is possible to explain all the data when we a consider two-component model of LLAGNs. For example, suppose that 80% of LLAGNs have the parameters of model B3, and the others have those of model B1 except $\eta_{\rm cr} = 2.4 \times 10^{-2}$. Then, the resultant spectrum can fit all the four data points. Even if each LLAGN is much fainter than quasars, the number density of LLAGNs is so high that they can significantly contribute the diffuse neutrino flux in principle.

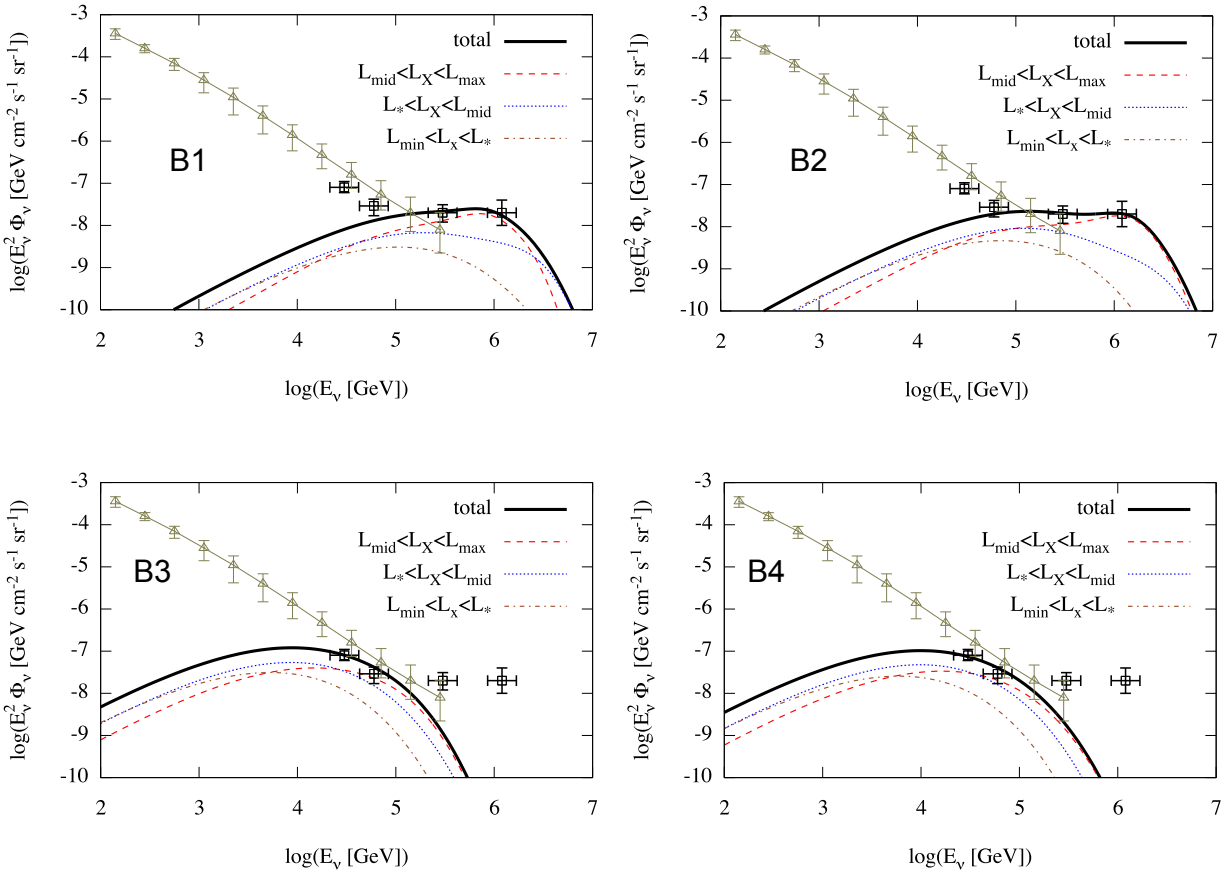

Figure 4.7: The contribution to the total intensity (thick lines) from different luminosity bins (thin lines). The red-dashed, blue-dotted, and brown-dot-dashed lines show the luminous, middle and faint parts, respectively. The green triangles represent the atmospheric muon neutrino background produced by CRs. The black squares show the observed data of neutrino signals.

Table 4.2: Model parameters for diffuse neutrino flux

model	$M_{\rm BH}[M_\odot]$	θ_e	ζ	$\eta_{\rm cr}$
B1	10^7	2.0	0.18	6×10^{-3}
B2	10^8	3.0	0.13	9×10^{-3}
B3	10^7	1.5	0.06	2.5×10^{-2}
B4	10^8	2.0	0.05	1.5×10^{-2}

4.3.2 Diffuse intensity of cosmic-ray protons

In our model, most of the injected protons escape from the accretion flow without depletion due to the low efficiency of pion production $f_\pi \lesssim 0.08$. Here, we discuss the effects of escaping protons.

Assuming that the Universe is filled with CR protons, we can estimate the CR flux as in the neutrino flux. Figure 4.8 shows the estimated flux of CR protons for models B1, B2, B3, and B4. This flux of the escaping protons is lower than observed CR flux for $10^{15.5}{\rm eV} < E_p < 10^{18}$ eV for all the models. In contrast to the neutrino spectra, the faint LLAGNs mainly contribute to CR flux at $E_p < 10^{16}$ eV. This is because the escaping proton luminosity has weak dependence on $\dot{m}$, compared to the neutrino luminosity. As described in Chapter 1, CR composition around the knee are probably heavy-nuclei dominant. The result of model B2 seems to conflict with that. However, it is unclear that CRs of $E_p \sim 10^{16}$ are able to arrive at the Earth from LLAGNs. In fact, the magnetic fields in the intergalactic medium (IGM) prevent the protons from traveling straightly, so that the distant sources cannot contribute to the CR flux. The diffusion length of CR protons during the cosmic time is estimated to be $\sim 12.3 B_{10}^{-1/2} E_{p,16}^{1/2}$ [Mpc], where $B_{10} = B/(10^{-10}{\rm Gauss})$ (cf., Berezinsky 2008). We use the Bohm limit and ignore the cosmic expansion. In addition, our Galaxy is located in the local group, where the magnetic fields are probably stronger than the usual IGM. These magnetic fields can potentially reduce the UHECR flux of $E_p \sim 10^{19}$ arriving at the Earth (Takami et al. 2014). We should take the

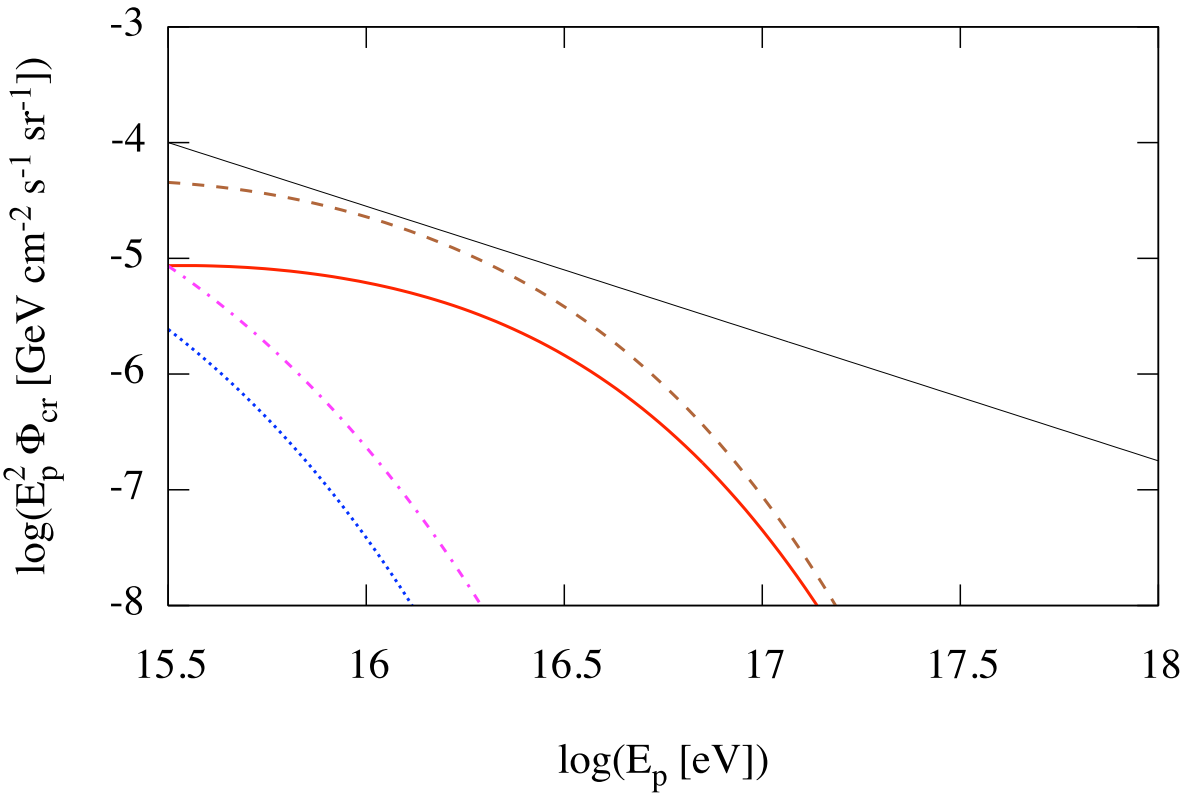

Figure 4.8: The maximum flux of the diffuse CR protons. The thick lines show the CR flux for B1 (red-solid), B2 (brown-dashed), B3 (blue-dotted), and B4 (magenta-dot-dashed). The thin-black-solid line shows the observed CR flux (e.g., Becker 2008). This figure is reproduced from Kimura et al. (2014b), by permission of the American Astronomical Society.

effects of these magnetic fields into account to discuss the arrival CR flux in detail.

The escaping protons would diffuse in host galaxies of LLAGNs, and interact with gas in the interstellar medium (ISM) inside the galaxies. The pion production efficiency of pp inelastic collisions in the ISM is estimated to be $f_{\pi,\rm gal} \simeq K_{pp} n_{p,\rm gal} \sigma_{pp} c t_{\rm trap} \sim 8 \times 10^{-4} E_{p,16}^{-0.3}$, where $E_{p,16} = E_p/(10\ \rm PeV)$, $n_{p,\rm gal} \sim 1\ \rm cm^{-3}$ is the mean nucleon density in the host galaxy, $t_{\rm trap} = h^2/4\kappa$ is the trapping time in the galaxy. We use the scale height $h \sim 1$ kpc and the

diffusion coefficient estimated in our Galaxy, $\kappa \sim 3 \times 10^{28} (E_p/1\mathrm{GeV})^{0.3}$ cm^2 s^{-1}. The escaping protons are expected to be confined in IGM. These protons are likely to interact with the protons or photons. The efficiency of pion production in IGM is not low, typically $\sim 10^{-2}$ below 100 PeV (Murase et al. 2013), which is likely to be more important than the reactions in ISM. Since most of the escaping protons are emitted from the faint LLAGNs, these processes might affect the diffuse neutrino flux.

4.3.3 Constraints on neutron loading in the jet

Toma & Takahara (2012) proposed a mass loading model to relativistic jets by relativistic neutrons made in the accretion flows. They consider that the relativistic neutrons whose Lorentz factor $\gamma_n \sim 3$ decaying at the polar region of SMBH are able to provide the jets with some amount of mass and energy. They estimated that the relativistic neutrons can inject the energy about $L_{\rm jet} \lesssim 2 \times 10^{-3} \dot{M} c^2$ and the mass $\dot{M}_{\rm jet} \lesssim 4 \times 10^{-4} \dot{M}$. This estimate results from the assumption of the total neutron luminosity from the accretion flow $L_n \sim 0.03 \dot{M} c^2$. The total luminosity of injected neutrons is estimated as

$$L_n \sim f_n \eta_{\rm cr} \dot{M} c^2, \tag{4.30}$$

where f_n is the neutron generation efficiency. The neutron generation efficiency is the same order of the pion production efficiency, $f_n \sim f_\pi \lesssim 0.08$. From the fitting of the diffuse neutrino flux, we obtain $\eta_{\rm cr} \sim 0.01$. These results restrict $L_n \lesssim 8 \times 10^{-4} \dot{M} c^2$, which is much lower than their assumption. In addition, resultant spectra of relativistic protons that are accelerated via stochastic acceleration are quite hard. This causes the differential luminosity and mass of the neutrons with $\gamma_n \sim 3$ to be much lower than the above restriction. Therefore, the neutron mass-loading model is disfavored when high-energy neutrinos are produced and limited by the observed neutrino data.

If LLAGNs cannot accelerate the CR protons up to sufficiently high energy, the neutron injection model is not restricted from the neutrino observation. For example, for the models

with $\zeta \leq 0.03$ and $q = 5/3$, LLAGNs cannot emit the neutrinos of $E_\nu \gtrsim 30$ TeV. However, it is still not easy to achieve the required value of $f_n \eta_{\rm cr} \sim 0.03$. One reason is that $\eta_{\rm cr}$ should be less than 0.1 in order to keep the structure of the RIAFs (Kimura et al. 2014a). Another reason is that the nature of collisionless plasma requires that the density should be low and limit $f_n \lesssim 0.3$. Thus, we need an optimized situation for neutron generation in order that the neutron injection model works as a jet mass-loading mechanism.

4.4 Discussion

4.4.1 Comparison to other AGN models

In this work, we consider one of the AGN core models, in which CR acceleration and neutrino production occur in the vicinity of the SMBH. Contrary to this work, in the previous literature, CR acceleration around the standard thin disk is assumed. However, since the disk plasma is typically collisional, faster dissipation is needed. The shock in accretion flows (e.g., Protheroe & Kazanas 1983; Stecker et al. 1991) or between blobs (Alvarez-Muniz & Mészáros 2004), and electric field acceleration (Kalashev et al. 2014) have been speculated as underlying acceleration mechanisms. The acceleration mechanism at such inner regions is very uncertain. For the efficient shock acceleration mechanism to work, $\tau_T \lesssim 1$ is required to have collisionless shocks unmediated by radiation (e.g., Murase & Ioka 2013), but the condition depends on the radius and accretion rate. It is highly uncertain if electric field acceleration occurs since the gap formation may be prohibited by a copious plasma supplied from the disk to the SMBH. In any case, if one allows acceleration of CRs in the vicinity of the disk, they should interact with ultraviolet photons supplied by multi-color blackbody emission from the standard disk (Shakura & Sunyaev 1973). Then, using the disk temperature around the innermost stable orbit $T_{\rm max}$, the typical neutrino energy is estimated to be

$$E_\nu \approx 0.05 \frac{0.5 m_p c^2 \bar{\epsilon}_{\rm pk}}{k_{\rm B} T_{\rm max}} \sim 400 \text{ TeV} \left(\frac{k_{\rm B} T_{\rm max}}{20 \text{ eV}} \right)^{-1}. \tag{4.31}$$

Hence, for an average accretion disk spectrum observed in quasars, a suppression around sub-PeV energies is expected (Dermer et al. 2014). In principle, it is possible to have lower-energy neutrinos by assuming high-temperature disks ad hoc. However, in such models, all the relevant parameters (the CR normalization, spectral index, maximum energy and disk temperature) are essentially free parameters. Also, since gamma rays should not escape because of high $\gamma\gamma$ optical depths, these models should be regraded as *hidden neutrino source models*. Note that the neutrino luminosity will be higher for AGNs with higher disk luminosities. Then, the well-observed X-ray luminosity function (Ueda et al. 2003) suggests that neutrino emission is dominated by AGNs with $L_X \gtrsim 10^{44}$ erg s^{-1} (Murase et al. 2014).

In the vicinity of the standard disk, $p\gamma$ interactions are usually the most important process (e.g., Szabo & Protheroe 1994; Alvarez-Muniz & Mészáros 2004). Also, the heavy jet has a problem in its energetics (Atoyan & Dermer 2003; Murase et al. 2014). On the other hand, there are some discussions on *pp* scenarios in radio galaxies (Becker Tjus et al. 2014), assuming the existence of dense knots with $N_H \sim 10^{24}$ cm^{-2}. If CRs are supplied by jets, the efficient neutrino production would significantly be diluted by their volume filling factor. Also, note that steep spectra $s_\nu \gtrsim 2.2$ are already ruled out by the multi-messenger data (Murase et al. 2013). In principle, this can be avoided by requiring that GeV-TeV gamma rays are attenuated, where this model should be regarded as one of the hidden neutrino source models that are difficult to test.

The most popular possibility is neutrino production in inner jets (e.g., Mannheim 1995; Atoyan & Dermer 2001; Mücke & Protheroe 2001). If one adopts the simple one-zone model, most important contributions come from quasar-hosted blazars, and external radiation fields are the most important (Murase et al. 2014; Dermer et al. 2014). Whereas it is possible to explain ultra-high-energy CRs with heavy nuclei, a power-law CR spectrum is inconsistent with the absence of $\gg 2$ PeV neutrinos. To explain the IceCube data around PeV energies, the maximum energy of CRs has to be lower than ultra-high energies and another component is needed at low energies. On the other hand, Tavecchio et al. (2014) showed that, if a two-

component model is invoked, BL Lac objects can be efficient emitters of PeV neutrinos without contradicting the observations of CRs. This is because the relative velocity between the spine and sheath allows us to have suitable target photon energies. However, it is not clear how BL Lacs can make a dominant contribution to the diffuse neutrino efficiency, compared to that from quasar-hosted blazars.

Among large scale jets, jets of Fanaroff-Riley II galaxies produce a non-relativistic cocoon shock and hot spot, and the latter is often bright at radio bands. The intergalactic density is usually too low to expect many neutrinos. However, since most AGNs are expected to be located in galaxy clusters and groups, their contributions may be relevant (e.g., Murase et al. 2008; Kotera et al. 2009). This possibility can be regarded as one of the *pp* scenarios, which has been constrained by multi-messenger data (Murase et al. 2013).

4.4.2 gamma rays from RIAFs

If neutrinos are produced by pion decay, gamma rays are also inevitably produced. The generated spectrum and luminosity of these gamma rays are similar to those of the neutrinos. However, high-energy gamma rays are absorbed by soft photons through $\gamma + \gamma \to e^+ + e^-$, so that the observed spectra of the gamma rays can be different from those of the neutrinos. In our model, internal absorption inside sources is relevant, and electromagnetic cascades are initiated. The emergent spectra are expected to have a break at the energy where the optical depth of pair production $\tau_{\gamma\gamma} = 1$. We estimate the optical depth by

$$\tau_{\gamma\gamma}(E_\gamma) \sim 0.2\sigma_{\rm T} R N_\gamma\left(\epsilon_t\right)\epsilon_t, \tag{4.32}$$

where $\epsilon_t \simeq (m_e c^2)^2/E_\gamma$ is the energy of the soft photons (e.g., Coppi & Blandford 1990). In our model, bright LLAGNs, such as the A3 model, have the cutoff energy $E_{\gamma,\rm cut} \sim 11$ GeV, while faint ones, such as the A2 model, have $E_{\gamma,\rm cut} \sim 15$ TeV. This means that bright LLAGNs emit only multi-GeV photons and cannot emit TeV photons. In this subsection, although we defer detailed studies of cascade emission, we here give the order-of-magnitude estimate on

expected gamma-ray signatures, which may serve as tests of the LLAGN model.

Recent observations by *Fermi* show that the diffuse isotropic γ-ray background (IGB) intensity is $\sim 5\times10^{-7}$ GeV cm^{-2} s^{-1} sr^{-1} at $E_\gamma \sim 1$ GeV, and $\sim 7\times10^{-8}$ GeV cm^{-2} s^{-1} sr^{-1} at $E_\gamma \sim 100$ GeV (Ackermann et al. 2014). This sets model-independent strong bounds on *pp* scenarios (Murase et al. 2013), and spectral indices should be harder than $s_\nu \sim 2.2$. The LLAGN model can avoid these constraints due to two reasons. First, the neutrino spectrum is harder than $s_\nu \sim 2.0$ since stochastic acceleration or magnetic reconnection mechanisms predict hard spectra compared to the diffusive shock acceleration mechanism, so that direct gamma rays do not contribute to the IGB. Second, GeV-TeV gamma rays may not escape, and LLAGNs can be regarded as hidden neutrino sources. In reality, the situation depends on $\dot{m}$, and GeV-TeV gamma rays can be produced via cascades. The maximum GeV-TeV flux can be estimated by assuming that all gamma rays escape and get cascaded in intergalactic space. Even in this case, noting that the gamma-ray flux is comparable to the neutrino flux, the estimated IGB flux is expected to be $\lesssim 10^{-7}$ GeV cm^{-2} s^{-1} sr^{-1} for B3 and B4, and $\lesssim 3\times10^{-8}$ GeV cm^{-2} s^{-1} sr^{-1} for B1 and B2. However, in RIAFs, pairs produced via $\gamma+\gamma\to e^+ + e^-$ would lose mainly via synchrotron emission rather than inverse-Compton emission, so the IGB at sub-TeV energies is expected to be sufficiently lower than the observed intensity. More accurate calculation and examine the contribution to the IGB remains as a future work.

How to test the LLAGN model presented here? Unfortunately, the average neutrino luminosity per source is too dim to detect individual sources. Gamma-ray detections are also difficult although we expect that faint LLAGNs can emit TeV photons. One of the examples of LLAGNs with RIAFs is Sgr A* at the Galactic Center. According to Yuan et al. (2003), thermal electrons at the inner part of RIAFs have the temperature $\theta_e \sim 8$, and emit the radio band photons of $L_\gamma \sim 10^{36}$ erg s^{-1} at $E_\gamma \sim 4\times10^{-3}$ eV. We calculate the inner part of the accretion flow of Sgr A* such that our model accounts for the observed radio luminosity. We use the same parameters with the reference model A1 except for $M_{\rm BH} = 4\times10^6 M_\odot$, $\dot{m} = 6\times10^{-6}$,

$\theta_e = 8.0$. Then, we find that protons are accelerated up to 20 TeV. The differential proton luminosity in this model is $E_p L_{E_p} \sim 7 \times 10^{36}$ erg s^{-1} at $E_p \sim 20$ TeV and $E_p L_{E_p} \sim 7 \times 10^{32}$ erg s^{-1} at $E_p \sim 10$ GeV. These escaping protons are expected to emit GeV - TeV gamma rays via pp reaction with surrounding materials, but this luminosity seems too low to explain the observed GeV - TeV gamma-ray fluxes (Liu et al. 2006; Chernyakova et al. 2011). These protons do not contribute to the observed flux of CR protons either. The neutrino flux from Sgr A* in this model is $E_\nu F_{E_\nu} \sim 3 \times 10^{-15}$ erg cm^{-2} s^{-1} with peak energy $E_\nu \sim 0.8$ TeV, which is too faint to be observed. This accretion flow is so faint that gamma rays from neural pion decay can escape from the flow directly. The gamma-ray flux is the same order of magnitude with that of neutrinos with peak energy $E_\gamma \sim$1.6 TeV, which is much lower than the gamma-ray flux at the Galactic Center observed by High Energy Stereoscopic System (HESS) (Aharonian et al. 2009a). Thus, this model does not contradict the observation of the Galactic Center and CR experiments.

Possibly, relatively brighter LLAGNs might be able to be observed at GeV gamma rays. The cores of Cen A and M87 are candidates, and both GeV and TeV gamma rays are detected (Abdo et al. 2009; Aharonian et al. 2006, 2009b; Sahakyan et al. 2013). For Cen A, the GeV gamma-ray spectrum cannot be smoothly connected to the TeV spectrum, and a break around 3 GeV has been suggested. This could indicate the existence of two components. Whereas some contributions could come from RIAFs, emission from jets are prominent (Takami 2010), and it would not be easy to identify the RIAF component in observed spectra. It would be better to look for radio-quiet AGNs with RIAFs, which do not have strong jets. The relatively bright LLAGNs, such as NGC 3031 (M81) and NGC 4579 (M58), have $L_X \sim 2 \times 10^{40}$ erg s^{-1} with $M_{\rm BH} \sim 6 \times 10^7 M_\odot$ (Eracleous et al. 2010). This luminosity can be obtained by our model with reference parameters except $M_{\rm BH} = 6.3 \times 10^7 M_\odot$. The peak neutrino luminosity in this model is $E_\nu L_{E_\nu} \sim 2 \times 10^{39}$ erg s^{-1}, which is too dim to detect. The pair-production cutoff energy is $E_{\gamma,\rm cut} \sim 12$ GeV, so that multi-GeV gamma rays are expected to escape. The estimated gamma-ray flux is $\sim 1 \times 10^{-12}$ erg cm^{-2} s^{-1} for M81 and $\sim 5 \times 10^{-14}$ erg cm^{-2} s^{-1}

for M58, assuming the distances $d \sim 3.6$ Mpc for M81 and $d \sim 17$ Mpc for M58, respectively (Eracleous et al. 2010). Thus, M81 could be detectable by *Fermi* or Cherenkov telescopes with low thresholds such as Major Atmospheric Gamma-ray Imaging Cherenkov Telescope (MAGIC) and Cherenkov Telescope Array (CTA). Multi-messenger studies are relevant to test the model and more precise calculations of photon spectra will be presented as future work.

4.5 Summary

We study particle acceleration and associated neutrino emission from RIAFs of LLAGNs. Various acceleration mechanisms have been suggested. In this work, for demonstration, we consider stochastic acceleration, for which we can calculate spectra of escaping particles by solving the Fokker-Planck equation. We model target photon fields in RIAFs by calculating inverse Compton emission, based on the one-zone approximation. Then we compare acceleration, escape, and cooling time scales, and find that in LLAGNs, proton acceleration is typically limited by diffusive escape rather than cooling processes. We also find that LLAGNs can have the protons up to more than 10 PeV for reasonable ranges of $\dot{m}$, $M_{\rm BH}$, ζ and q. Then, the pp or $p\gamma$ production may lead to PeV neutrinos. Note that production of ultra-high-energy CRs is not expected in this model. The CR acceleration efficiency is highly uncertain, so we treat it as a free parameter assuming that the luminosity of escaping CRs is equal to $\eta_{\rm cr}\dot{M}c^2$, including both diffusive and advection escape. Then, the luminosity of CRs escape via diffusion is estimated to be around 3×10^{40} erg s^{-1} in our reference model. We calculate associated neutrino emission, and find that high-energy neutrino production occurs mainly via pp interactions, and the meson production efficiency is typically on the order of 1%. The neutrino spectrum is hard since CRs are assumed to be accelerated via the stochastic acceleration mechanism.

We also calculated the diffuse neutrino intensity by using the H_α luminosity function of LLAGNs and assuming no redshift evolution. Interestingly, we find that the observed IceCube

data can be fitted for reasonable parameters if $\sim 1\%$ of the accretion luminosity is carried by CRs. This fraction guarantees our assumption that the CRs do not affect the dynamical structure of RIAFs (Kimura et al. 2014a). The number density of LLAGNs is about $\sim 10^{-3} - 10^{-2}$ Mpc^{-3}, which is much greater than those of radio-loud AGNs including blazars. Since the spectrum is hard, this result does not contradict the diffuse gamma-ray bound (Murase et al. 2013).

Whereas RIAFs of LLAGNs can provide interesting targets of high-energy neutrino and gamma-ray observations, unfortunately, there are many uncertainties in the model. First, parameters related to acceleration are uncertain, although values we adopt are often used for other sources such as gamma-ray bursts. However, although we consider stochastic acceleration, one should keep in mind that our neutrino flux calculations can be applied to different cases such as acceleration via magnetic reconnections. For more reliable predictions, we need better knowledge on the distribution of non-thermal particles, which could be achieved by future particle-in-cell simulations. Second, the luminosity function of LLAGNs is quite uncertain due to their faintness. Obviously, to estimate the diffuse neutrino intensity, more observational data on the shape of the luminosity function in the faint end and their redshift evolution are needed, as well as the mass function of SMBHs hosted by LLAGNs. In addition, contributions from RIAFs with the critical mass accretion rate, at which RIAFs change to the standard disk, may also be relevant. This implies the importance of understanding the physical relationship between LLAGNs and Seyferts.

One of the potentially interesting points of the LLAGN model is that one can explain the latest IceCube data around 10 TeV. The latest data suggest steeper indices of $s_\nu \sim 2.3 - 2.5$, which seems challenging for many models. Galactic sources may be responsible for $\lesssim 100$ TeV neutrinos, but it is premature to discuss such a two-component scenario due to the lack of compelling anisotropy. It could be explained by an exponential cutoff or spectral break of starburst galaxies, but hard indices of $s_\nu \sim 2$ are needed. Alternatively, hidden neutrino sources can provide viable possibilities. Such a speculation includes not only the AGN core

models including the LLAGN model but also orphan neutrino production in low-power gamma-ray burst jets (Murase & Ioka 2013).

As a final remark, we stress that the neutrino observations may be powerful for probing physics of accretion disks and jets. In this work, we calculated the neutron generation rate in RIAF (see also Kimura et al. 2014a), and argue that an optimized parameter values are required for RIAFs to have as high neutron generation rate as suggested by Toma & Takahara (2012). As long as CR spectral indices are hard as expected in stochastic acceleration or magnetic reconnection, the model of jet mass-loading mediated by neutrons is strongly restricted by neutrino observations unless ζ is very low.

Chapter 5

Summary & Future work

We study the effects of high-energy particles on dynamical structure of hot accretion flows and emission of cosmic-ray protons and neutrinos from hot accretion flows. The hot accretion flows have quite different structure from those of the standard disks. They are so hot and tenuous that non-thermal particles can exist. The non-thermal particles seem to affect the dynamical structure of the flow because they extract some amount of energy through the escape of particles. However, they do not affect the dynamical structure very much, because the energy loss rate by non-thermal particle is not enough to form a Keplerian disk for usual parameters. The neutrinos are naturally generated in the hot accretion flows with non-thermal particles, and thus, LLAGNs are a source of astrophysical neutrinos. They can fit the neutrino flux of the IceCube data for reasonable parameters owing to their high number density. In this chapter, we describe the findings and remaining problems of this study.

5.1 Effects on dynamical structure

The non-thermal protons inside RIAFs are likely to interact with thermal protons and photons. These reactions generate pions, and decay products of these pions can escape from RIAFs. The non-thermal protons can escape directly from RIAFs owing to their long mean free path. Thus,

the non-thermal particles may act as a coolant of the flow. The non-thermal particles also change the pressure of the accretion flow because they have different specific heat ratio from thermal particles. Therefore, the non-thermal particles can potentially affect the dynamical structure.

We formulate a set of one-dimensional equations that consist of thermal and non-thermal particles. The thermal particles obey the fluid equations, and non-thermal particles obey the diffusion-convection equations. We use the moment equations of the diffusion-convection equation for simplicity. We solve time evolution of the basic equations, and obtain steady state solutions. Our results without non-thermal particles are consistent with the previous studies of global structure of ADAFs.

From the solutions with non-thermal particles, it is found that the non-thermal particles do not affect the dynamical structure very much when their energy density is less than that of thermal particles. The non-thermal particles dominate over the thermal particles when 90% of the total heating rate is injected into the non-thermal particles. For this extreme case, the temperature of thermal particles are sufficiently lower than that without non-thermal particles, which may affect the electron temperature in RIAFs. However, the dynamical structures are still advection-dominated flows, and the non-thermal particles cannot change the physical quantities except temperature by more than an order of magnitude.

The energy extraction rate is the key quantity to change the dynamical structure drastically. For the cases with the high diffusion parameter, escaping protons carry away most of the injected energy. If the energy extraction rate is comparable to the total heating rate, $\sim 0.1\dot{M}c^2$, the flow has a slow radial velocity, high density, and almost Keplerian angular momentum. These features are similar to those of the standard disks. However, this situation is quite extreme. Therefore, we conclude that it is difficult that the non-thermal particles affect the dynamical structure of hot accretion flows.

Although the non-thermal particles are unlikely to affect the dynamical structure, they can produce some amount of neutrinos, cosmic-ray protons, and gamma rays in RIAFs. We

estimate the luminosity of escaping particles for the steady state solutions. For low mass accretion rates with high diffusion coefficients, the luminosity of diffusively escaping protons amounts to $L_{\rm p} \sim 10^{-2}\dot{M}c^2$. In contrast, for high mass accretion rates, the luminosity of escaping neutrons, $L_{\rm n}$, is greater than $L_{\rm p}$, and its maximum value is nearly the same as that of the protons $L_{\rm n} \sim 10^{-2}\dot{M}c^2$. The luminosities of gamma rays and neutrinos are a few times greater than $L_{\rm n}$. We note that radiative processes by thermal electrons are expected to be important for high mass accretion rates. These luminosities of escaping particles are enough to explain relatively dim jets. However, the mass injection rate is so low that the resultant terminal Lorentz factor is too high, compared to the observed jets. It is difficult to explain the observed jets by the escape of the non-thermal particles.

5.2 Neutrino and cosmic ray emission

RIAFs can emit some amount of high-energy neutrinos, and LLAGNs seem to include RIAFs. Thus, LLAGNs are potential sources of the high-energy neutrinos. We calculate the neutrino flux from RIAFs in LLAGNs. The extraterrestrial neutrinos detected by IceCube are likely to originate from astrophysical objects. This motivates us to examine whether the LLAGN model can explain the IceCube neutrinos.

We estimate the physical quantities of RIAFs in LLAGNs using one-zone approximation. The energy spectra of relativistic protons in the RIAFs are calculated by solving the Fokker-Planck equation, where the timescales of acceleration, escape, and cooling are important to determine the proton spectra. We consider *pp* inelastic collisions, photomeson production, and proton synchrotron for the cooling time, and both infall and diffusive escape are taken into account as the escape time. We find that in a typical LLAGN, the acceleration of protons is limited by the diffusive escape around $E_p \sim 2\times10^{15}$. Since the efficiency of proton acceleration is uncertain, we treat it as a parameter $\eta_{\rm cr}$, assuming that the luminosity of escaping protons equals to $\eta_{\rm cr}\dot{M}c^2$. Then, the luminosity of escaping protons amounts to $L_p \sim 3\times10^{40}$ erg s^{-1}

for our reference model. We calculate the neutrino spectrum from LLAGNs, and find that *pp* reactions mainly produce neutrinos for $E_\nu \lesssim 1$ PeV while $p\gamma$ reactions are more efficient for $E_\nu \gtrsim 1$ PeV. The efficiency of meson production is typically the order of 1% for *pp* reaction dominant cases and at most 10% for $p\gamma$ dominant cases. They have hard spectra because the protons are accelerated via the stochastic acceleration.

We calculate the diffuse neutrino intensity using the H_α luminosity function of LLAGNs, assuming no redshift evolution. We found that the observed IceCube data can be fitted for reasonable parameters if non-thermal protons gain $\sim 1\%$ of the accretion luminosity. This fraction guarantees our assumption that the non-thermal protons do not affect the dynamical structure of RIAFs (see Chapter 3). For 100 - 1000 TeV neutrinos, the luminous part of LLAGNs mainly emit the neutrinos owing to the efficient $p\gamma$ reaction. For 10 - 100 TeV neutrinos, *pp* reaction mainly produce the neutrinos, and a wide range of LLAGNs contribute to the neutrino except the faint part of LLAGNs. The number density of LLAGNs is about $10^{-2} - 10^{-3}$ Mpc^{-3}, which is much greater than that of radio-loud AGNs including blazars. This is why LLAGNs are able to contribute to the diffuse neutrino flux even if they are much fainter than the quasars.

The LLAGN model does not contradict the diffuse gamma-ray bound observed by *Fermi*. Since the energy spectrum of protons is hard, the energy density of protons below 10 TeV is low enough to avoid the contradiction. The LLAGN model may neither contradict the observed cosmic-ray flux because cosmic rays for $E_p \lesssim 10^{17}$ eV seem to be confined in intergalactic medium, and LLAGN cannot accelerate the cosmic rays up to ultra high-energy. The fitting of neutrinos restricts the neutron loading model of the relativistic jet production. Our models predict that the total luminosity of injection into the relativistic protons are around 1% of the accretion luminosity $\dot{M}c^2$. For such a low value of the injection luminosity, the generation rate of neutrons is so low that they cannot inject a sufficient amount of mass at the jet launching region.

5.3 Future work

We study the dynamics of accretion flows and the cosmic-ray neutrinos. To study the spatial structure of accretion flows, we often perform the numerical simulations. On the other hand, we often use the analytical order-estimation to discuss the detectability of cosmic-ray neutrinos. This thesis consists of both studies. Combining these two studies, we could calculate the neutrino spectrum for a spatially one-dimensional model with an energy spectrum, including the radiation from thermal electrons with a simple treatment. However, this is beyond the scope of this thesis.

There are many ignored processes and uncertain parameters in this thesis. For the study of dynamical structure, the effect of a disk wind is one of the most important processes in hot accretion flows, but it is not included in Chapter 3. The numerical simulation shows that the hot accretion flow naturally blows a disk wind, and the mass loss rate by the wind is comparable to the mass accretion rate at $\varpi \gtrsim 30R_{\rm S}$ (Yuan et al. 2012; Sadowski et al. 2013). Thus, the disk dynamical structure with a disk wind is different from that without a disk wind. Since the multi-dimensional effect and magnetic fields are essential for the disk wind, we need a multi-dimensional magnetohydrodynamic simulation to properly address the impact of a disk wind.

The electrons are also important, but it is neglected in Chapter 3. As the mass accretion rate becomes higher, the cooling rate by electrons becomes higher. Since most of the photons are generated by the electrons in usual accretion flows, treating the electron component is essential to compare the theoretical models to observations. The role of electron cooling is expected to be related to the problems of state transition.

To obtain the electron temperature, we need to know the heating mechanisms in a collisionless plasma. However, it is really difficult to investigate the electron heating mechanism in a hot accretion flow because of the vast scale difference between plasma and hydrodynamical phenomena. What we can do now is including some phenomenological heating rate when

we estimate the electron temperature. The comparison between observations and theoretical predictions seems to give us the electron temperature in RIAFs (Nemmen et al. 2014). However, we cannot obtain the electron temperature with high accuracy due to both theoretical uncertainties of models and the lack of observational data of LLAGN.

The electron temperature is important also for the study of neutrino emission, which is just given as a parameter in this thesis. This strongly affects the photon spectrum from a RIAF. This spectrum has an influence on both the neutrino generation rate by $p\gamma$ reactions and the X-ray luminosity of LLAGNs that is important for the diffuse neutrino flux. The mass function of SMBHs in LLAGNs should also be taken into account because the X-ray luminosity of LLAGN also depends on the SMBH mass. A deeper survey is necessary to clarify the mass function and luminosity function of LLAGNs.

We introduce many uncertain parameters on the property of high-energy particles, such as the injection efficiency. The detailed comparison to the observations seems to constrain the parameters. Our model produces not only neutrinos but also gamma rays. The gamma rays from nearby LLAGNs may be detectable by *Fermi* and/or CTA, although it is challenging. Since the gamma-ray luminosity depends on the injection efficiency of non-thermal protons, this observation may constrain the injection efficiency even if they just set an upper limit. The numerical simulations also seem useful to determine the uncertain parameters. There are some MHD simulations that give us the information of turbulent magnetic fields of accretion flows. Solving the particle motion in the fields with MHD simulations, we can examine both the spatial diffusion and stochastic acceleration processes of relativistic particles inside the accretion flows. Although we are still far from the understanding of physics of accretion phenomena, the numerical works and gamma-ray observations will provide us with a better view of accretion phenomena in the future.

Appendix A

Derivation of some equations

A.1 Energy equation

Here, we derive the equation (2.3) from the first law of thermodynamics

$$d\epsilon = Tds - p_{\rm g} d\left(\frac{1}{\rho}\right) \tag{A.1}$$

where we write this equation with the specific variables. Multiplying ρ and dividing the equation by dt, we get

$$\rho\frac{d\epsilon}{dt} = \rho T\frac{ds}{dt} - \frac{p_{\rm g}}{\rho}\frac{d\rho}{dt}, \tag{A.2}$$

where $d/dt = \partial/(\partial t) + \boldsymbol{v}\cdot\boldsymbol{\nabla}$ is the Lagrangian derivative. Using the equation of continuity (2.1), we can write

$$\rho\frac{d\epsilon}{dt} = \frac{\partial(\rho\epsilon)}{\partial t} + \boldsymbol{\nabla}\cdot(\rho\epsilon\boldsymbol{v})\,. \tag{A.3}$$

From the definition of entropy, the term ρTds represents the net cooling and/or heating rate in unit volume,

$$\rho Tds = q_{\rm vis} - q_{\rm cool} \tag{A.4}$$

Using the equation of continuity (2.1) again, we can write

$$\frac{p_{\rm g}}{\rho}\frac{d\rho}{dt} = -p_{\rm g}\boldsymbol{\nabla}\cdot\boldsymbol{v}. \tag{A.5}$$

Thus, we can obtain the energy equation as

$$\frac{\partial(\rho\epsilon)}{\partial t} + \boldsymbol{\nabla}\cdot(\rho\epsilon\boldsymbol{v}) = -p_{\rm g}\boldsymbol{\nabla}\cdot\boldsymbol{v} + q_{\rm vis} - q_{\rm cool}. \tag{A.6}$$

A.2 Derivation of hydrostatic equilibrium

The momentum conservation for vertical direction is written as

$$\frac{\partial}{\partial t}(\rho v_z) + \frac{1}{r}\frac{\partial}{\partial r}(r v_r \rho v_z) + \frac{\partial}{\partial z}\left(\rho v_z^2\right) = -\frac{\partial p}{\partial z} - \rho\Omega_{\rm K}^2 z \tag{A.7}$$

From the equation (2.19), we find

$$\frac{\partial v_z}{\partial z} = \frac{d\ln H}{dt} = \frac{v_r}{H}\frac{\partial H}{\partial r}, \tag{A.8}$$

where we use steady assumption $\partial/\partial t = 0$ from the middle equation to the left. Assuming $v_z = z$ at $z = 0$, we obtain

$$v_z = \frac{d\ln H}{dt} z = v_r \frac{z}{H}\frac{\partial H}{\partial r}. \tag{A.9}$$

Again, we use the steady assumption from the middle to the left. Using this equation of v_z with steady assumption, we can rewrite equation (A.7) as

$$\frac{1}{r}\frac{\partial}{\partial r}\left(r v_r^2 \rho \frac{z}{H}\frac{\partial H}{\partial r}\right) + \frac{\partial}{\partial z}\left\{\rho\left(\frac{z}{H}\frac{\partial H}{\partial r}\right)^2\right\} = -\frac{\partial p}{\partial z} - \rho\Omega_{\rm K}^2 z \tag{A.10}$$

Taking $\int_0^\infty dz$ with assumption that ρ and v_r are constant for z, we obtain

$$\frac{1}{r}\frac{\partial}{\partial r}\left(r v_r^2 \Sigma \frac{dH}{dr}\right) = \frac{2P}{H} - \Sigma\Omega_{\rm K}^2 H \tag{A.11}$$

This equation have the advection term, the pressure term, and the gravity term. Estimating the order of each term, we find that the ratio of the pressure term to the advection term is $\sim (c_{\rm s}/v_r)^2$. Thus, we can ignore the advection term when we focus on the subsonic region. Then, the scale height H is determined by the equilibrium between the pressure gradient force and the gravity, which is expressed as

$$H \approx \frac{\sqrt{(2P/\Sigma)}}{\Omega_{\rm K}} \sim \frac{c_{\rm s}}{\Omega_{\rm K}}. \tag{A.12}$$

Appendix B

Test calculation for dynamical structure

Here, we show the test calculations for solving the fluid equations, (2.11), (2.12), (2.14), and (2.21). We solve the time evolution of these equations until steady state solutions are realized, using a finite differential method with time explicit procedure. Our code is similar to the ZEUS code in which the artificial viscosity is used (von Neumann & Richtmyer 1950; Stone & Norman 1992). The artificial viscosity prevents some numerical instability from growing. We use staggered mesh where the vector variables (v_r) are defined at the cell boundary while the scalar variables (l_z, Σ, E) are at the cell center. Our code use the operator splitting method. First, we make a calculation without advection term,

$$\Sigma\frac{\partial \boldsymbol{v}}{\partial t} = -\boldsymbol{\nabla} p_{\rm g} + \boldsymbol{F} - \boldsymbol{\nabla}\cdot\boldsymbol{\Pi} + \boldsymbol{\nabla}\cdot\boldsymbol{Q}_{\rm av} \tag{B.1}$$

$$\frac{\partial(\Sigma\epsilon)}{\partial t} = -p_{\rm g}\boldsymbol{\nabla}\cdot\boldsymbol{v} + Q_{\rm vis} - Q_{\rm cool} + \boldsymbol{Q}_{\rm av} : \boldsymbol{\nabla}\boldsymbol{v}, \tag{B.2}$$

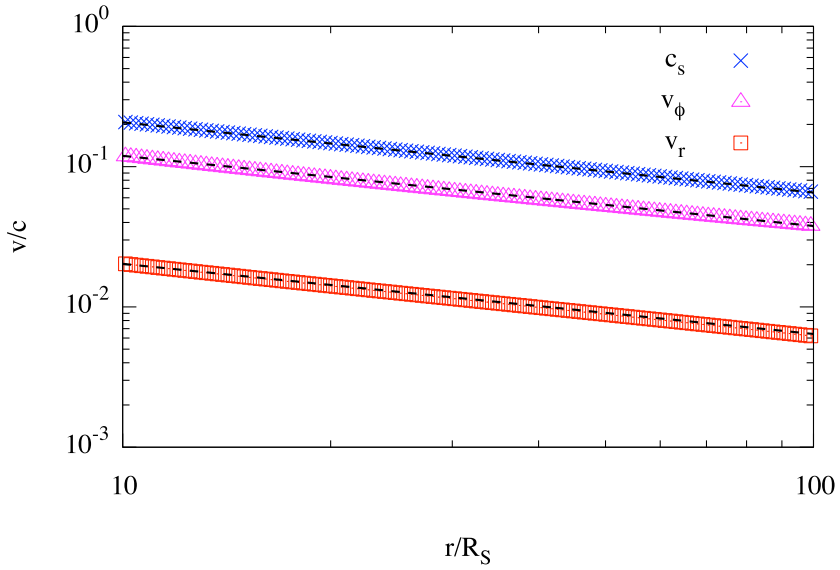

Figure B.1: The results of test calculation of fluid equations. The upper panel shows the radial profiles of the velocities. The blue crosses, magenta triangles, and red squares show the numerical results of the sound velocity $c_{\rm s}$, azimuthal velocity v_ϕ, and radial velocity v_r. The black-solid lines show the analytic solutions.

where $Q_{\rm av}$ is the artificial viscosity term. After that, we calculate the advection without source term,

$$\frac{d}{dt}\int_V \Sigma dV = -\int_{dV} \Sigma \boldsymbol{v}\cdot\boldsymbol{dS} \tag{B.3}$$

$$\frac{d}{dt}\int_V \Sigma \boldsymbol{v} dV = -\int_{dV} \Sigma \boldsymbol{v}\boldsymbol{v}\cdot\boldsymbol{dS} \tag{B.4}$$

$$\frac{d}{dt}\int_V \Sigma \epsilon dV = -\int_{dV} \Sigma \epsilon \boldsymbol{v}\cdot\boldsymbol{dS}, \tag{B.5}$$

where V is the volume of each cell and $\boldsymbol{dS}$ is the surface vector of each cell.

We check our numerical code by comparing our steady state solutions obtained by numerical calculation to the analytic ones given in equations from (2.48) to (2.51). Figure B.1 shows the radial profiles of $c_{\rm s}$, v_ϕ, and v_r. This calculation is performed with the units $G = c = M = 1$

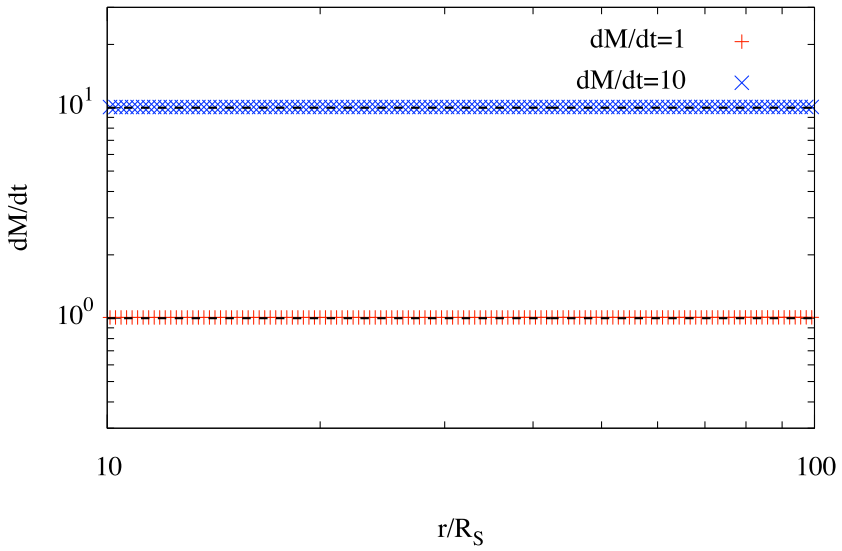

Figure B.2: The results of test calculation of fluid equations. The lower panel shows the radial profiles of mass accretion rates for both numerical solutions (points) and given values (dashed lines).

with the number of grids $N = 128$. We use parameters $\gamma = 3/2$, $\alpha = 0.1$ and $\dot{M}$ =1 or 10. The blue-crosses, magenta-triangles, and red squares show the numerical results of $c_{\rm s}$, v_ϕ, and v_r. They match well with the analytic solutions, shown by the black-dashed lines. These velocities are independent of the mass accretion rate, which is consistent with the analytic solution. Figure B.2 shows that the radial profiles of the mass accretion rate. The blue crosses and red pluses indicate the mass accretion rate for $\dot{M} = 10$ and $\dot{M} = 1$, respectively, obtained by the numerical results. These results also match the analytic solution expressed as the black-dashed lines.

Appendix C

Calculation method for the spectrum from thermal electrons

C.1 Synchrotron and Bremsstrahlung

We use a fitting formula for the synchrotron and bremsstrahlung (Narayan & Yi 1995). Here, we use the cgs units. The cooling rates by bremsstrahlung of electron-electron q_{ei} and ion-electron q_{ee} are represented as follows,

$$q_{ei} = 1.48 \times 10^{-22} n_e^2 F_{ei}(\theta_e), \tag{C.1}$$

$$q_{ee} = \begin{cases} 2.56 \times 10^{-22} n_e^2 \theta_e^{3/2} \left(1 + 1.1\theta_e + \theta_e^2 - 1.25\theta_e^{5/2}\right) & (\theta_e < 1) \\ 3.40 \times 10^{-22} n_e^2 \theta_e \left[\ln(1.123\theta_e + 1.28)\right] & (\theta_e > 1) \end{cases}, \tag{C.2}$$

where we use

$$F_{ei} = \begin{cases} 4\left(\frac{2\theta_e}{\pi^3}\right)^{0.5}(1 + 1.781\theta_e^{1.34}) & (\theta_e < 1) \\ \frac{9\theta_e}{2\pi}[\ln(1.123\theta_e + 0.48) + 1.5] & (\theta_e > 1) \end{cases}. \tag{C.3}$$

The emissivity of bremsstrahlung is related to the cooling rates as

$$q_{ei} + q_{ee} = \int_0^\infty d\nu j_{\nu,\mathrm{br}}. \tag{C.4}$$

Approximating $j_{\nu,\mathrm{br}} = j_0 \exp(-h\nu/(k_\mathrm{B}T_e))$, where j_0 does not depend on ν, we can write

$$j_{\nu,\mathrm{br}} = q_\mathrm{br}\frac{h}{k_\mathrm{B}T_e}\exp\left(-\frac{h\nu}{k_\mathrm{B}T_e}\right) \tag{C.5}$$

where $q_\mathrm{br} = q_{ei} + q_{ee}$ is the cooling rate per unit volume. We assume the gaunt factor is unity.

The synchrotron emissivity is

$$j_{\nu,sy} = \frac{4\pi e^2 n_e \nu}{\sqrt{3}cK_2(1/\theta_e)} I'\left(\frac{4\pi m_e c\nu}{3eB\theta_e^2}\right), \tag{C.6}$$

where

$$I'(x) = \frac{4.0505}{x^{1/6}}\left(1 + \frac{0.4}{x^{1/4}} + \frac{0.5316}{x^{1/2}}\right)\exp(-1.8899x^{1/3}). \tag{C.7}$$

C.2 Radiative transfer

We define the optical depth for absorption as

$$\tau_\nu \equiv \frac{\sqrt{\pi}}{2}\kappa_\nu H \sim \frac{\sqrt{\pi}}{2}\kappa_\nu R, \tag{C.8}$$

where

$$\kappa_\nu = \frac{j_{\nu,br} + j_{\nu,sy}}{4\pi B_\nu} \tag{C.9}$$

is the absorption coefficient and B_ν is the Planck function. The photon energy flux from a RIAF is written as (Manmoto et al. 1997)

$$F_\nu = \frac{2\pi}{\sqrt{3}}B_\nu\left[1 - \exp(-2\sqrt{3}\tau_\nu)\right], \tag{C.10}$$

where we use Eddington approximation (Rybicki & Lightman 1979) when estimating the vertical energy flux. The luminosity by the synchrotron and bremsstrahlung is estimated as

$$L_{\nu,0} = 2\pi R^2 F_\nu. \tag{C.11}$$

C.3 Inverse Compton scattering

We calculate the spectrum of the inverse Compton scattering. Seed photons are the photon field by bremsstrahlung and synchrotron. Assuming homogeneous and isotropic distribution, the photon occupation number evolves by (cf. Coppi & Blandford 1990),

$$\frac{dN_\gamma(\epsilon)}{dt}\Delta\epsilon = -N_\gamma(\epsilon)\Delta\epsilon\int d\gamma N_e(\gamma)R_c(\epsilon,\gamma) + \int d\gamma\int d\epsilon' N_e(\gamma)N_\gamma(\epsilon')R_c(\epsilon',\gamma)P_c(\epsilon;\epsilon',\gamma) + \dot{N}_{\gamma,0}\Delta\epsilon - \dot{N}_{\gamma,esc}\Delta\epsilon, \tag{C.12}$$

where $\epsilon = h\nu/(m_e c^2)$, $N_\gamma(\epsilon)$ is the differential number density of photon, $R_c(\epsilon,\gamma)[\mathrm{cm}^3\ \mathrm{s}^{-1}]$ is the reaction rate of the electrons of Lorentz factor γ and the photons of energy ϵ, and $P_c(\epsilon;\epsilon',\gamma)$ is the probability that the reactions by the photons of energy ϵ' and electrons of energy γ create the photons of energy ϵ. We add the injection rate of seed photons $\dot{N}_{\gamma,0}$ and escape rate of photons $\dot{N}_{\gamma,esc} = N_\gamma(\epsilon)/(R/c)$. We calculate the steady state solution of this equation. Since optical depth of the flow is less than unity, we neglect the first term of right-hand side of Equation (C.12). The differential number density can be expanded by the number of Compton scattering as $N_\gamma(\epsilon) = N_{\gamma,0} + N_{\gamma,1} + ...$, where $N_{\gamma,0}$ is determine by the balance of the escape and the injection

$$N_{\gamma,0}/(R/c) = \dot{N}_{\gamma,0} = L_{\epsilon,0}/(\pi R^3 h\nu), \tag{C.13}$$

where $L_{\epsilon,0} = (m_e c^2/h)L_{\nu,0}$. We obtain the $N_{\gamma,i}$ by solving the following equation,

$$\frac{N_{\gamma,i}(\epsilon)}{R/c}\Delta\epsilon = \int d\gamma\int d\epsilon' N_e(\gamma)N_{\gamma,i-1}(\epsilon')R_c(\epsilon',\gamma)P_c(\epsilon;\epsilon',\gamma). \tag{C.14}$$

We use the fitting formula for R_c (Coppi & Blandford 1990)

$$R(\epsilon,\gamma) = \frac{3c\sigma_T}{8\gamma\epsilon}\left[\left(1-\frac{2}{\gamma\epsilon}-\frac{2}{\gamma^2\epsilon^2}\right)\ln(1+2\gamma\epsilon)+\frac{1}{2}+\frac{4}{\gamma\epsilon}-\frac{1}{2(1+2\gamma\epsilon)^2}\right]. \tag{C.15}$$

From the energy conservation, the reaction with $4\gamma^2\epsilon/3 > \gamma+\epsilon$ does not occur. In this case, we take $R(\epsilon,\gamma) = 0$. We use delta function approximation for P_c,

$$N_\gamma(\epsilon')P_c(\epsilon;\epsilon',\gamma) = N_\gamma(\epsilon')\Delta\epsilon'\delta\left(\epsilon-\frac{4}{3}\gamma^2\epsilon'\right). \tag{C.16}$$

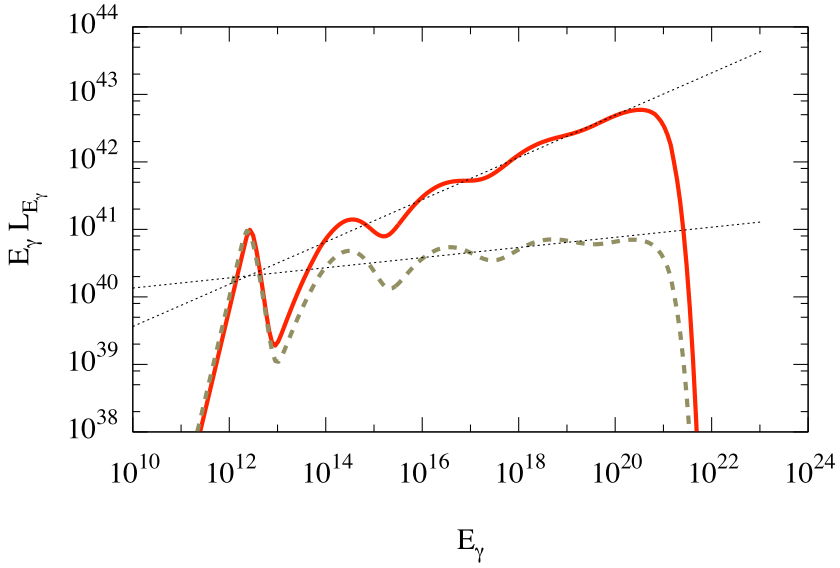

Figure C.1: The calculated inverse Compton spectra. The red-solid and green-dashed lines show the calculated spectra. Our calculations are consistent with analytic power-law fittings by Pozdnyakov et al. (1983), which are shown as the dotted lines.

From the treatment described above, we obtain

$$N_{\gamma,i}(\epsilon) = \frac{R}{c}\int d\gamma \frac{3}{4\gamma^2} N_e(\gamma) N_{\gamma,i-1}\left(\frac{3\epsilon}{4\gamma^2}\right) R_c\left(\frac{3\epsilon}{4\gamma^2}, \gamma\right). \tag{C.17}$$

We calculate $N_{\gamma,i}(\epsilon)$ until the number density of the i times scattered photons is much less than that of the bremsstrahlung in all the range in which we are interested.

C.4 Calculation check of the inverse Compton calculation

We check consistency of the calculation method described above with previous works. Pozdnyakov et al. (1983) consider a one-zone plasma cloud whose scattering optical depth $\tau_{\rm es}$ and electron temperature θ_e, and calculate emergent spectra of thermal Compton scattering by

using the Monte Carlo techniques, injecting sufficiently low energy seed photons compared to the electron energy. They found that the emergent spectra have power-law shape whose index is expressed as

$$\alpha_{\rm IC} = -\frac{\ln \tau}{\ln(12\theta_e^2 + 26\theta_e)} + \frac{0.2}{\theta_e}. \tag{C.18}$$

Figure C.1 shows the spectra obtained by our model (solid and dashed lines) and the corresponding power-law function (dotted lines) predicted by Pozdnyakov et al. (1983). We set $\theta_e = 2.0$, $\alpha = 0.1$, $\beta = 3$, and $\varpi = 10$ for both the solid and dashed lines. We use $\dot{m} = 0.03$ and $\dot{m} = 0.01$ for the solid and dashed lines, respectively. The scattering optical depths are $\tau_{\rm es} = 0.067$ and $\tau_{\rm es} = 0.022$ for solid and dashed lines, respectively. We can see good agreement between our models and predicted power-law functions. Thus, our calculation method is good approximation for optically thin accretion flows.

Appendix D

Test calculation for solving the Fokker-Planck equation

Here, we show the test calculations for solving the Fokker-Planck equations. We solve the time evolution of the Fokker-Planck equation using an implicit method proposed by Chang & Cooper (1970) until steady state solutions are realized. The Chang & Cooper method is a flux conservative finite difference scheme in which the particle number is conserved in the absence of sinks or sources. This method uses centered difference on the diffusion term but a weighted difference on the advection term. This weight is determined so that it works as the upwind difference. This procedure guarantees that the values of the distribution function are always positive if they initially have some positive values even with a sink term (Park & Petrosian 1996).

We check our numerical code by comparing our steady state solutions obtained by numerical calculations to the analytic ones given by Becker et al. (2006). Since acceleration of protons in LLAGN is limited by diffusive escape, we show the test calculation for efficient escape cases. We write the Fokker-Planck equations as

$$\frac{\partial}{\partial t}F(p) = \frac{1}{p^2}\frac{\partial}{\partial p}\left(p^2 D_p \frac{\partial F(p)}{\partial p}\right) - \frac{F(p)}{t_{\rm esc}} + \dot{F}_{\rm inj}. \tag{D.1}$$

Assuming that

$$D_p = D_* m_p^2 c^2 \left(\frac{p}{m_p c}\right)^q, \tag{D.2}$$

$$t_{\rm esc} = t_* \left(\frac{p}{m_p c}\right)^{q-2}, \tag{D.3}$$

$$\dot{F}_{\rm inj} = \frac{\dot{N}_0}{4\pi p^2}\delta(p - p_0), \tag{D.4}$$

the steady state solution is expressed as

$$\begin{aligned} N(x) &\equiv 4\pi m^3 c^3 x^2 F(x) \\ &= \frac{\dot{N}_0}{(2-q)x_0 D_*}\left(\frac{x}{x_0}\right)^{1/2}(xx_0)^{(2-q)/2} I_{(\beta-1)/2}\left(\frac{\sqrt{\theta}x_{\rm min}^{2-q}}{2-q}\right) K_{(\beta-1)/2}\left(\frac{\sqrt{\theta}x_{\rm max}^{2-q}}{2-q}\right), \end{aligned} \tag{D.5}$$

where $x = p/(m_p c)$, $x_0 = p_0/(m_p c)$, $x_{\rm min} = \min(x, x_0)$, $x_{\rm max} = \max(x, x_0)$, $\beta = 3/(2-q)$, $\theta = 1/(D_* t_*)$. We use the first and second modified Bessel function $I_n(x)$ and $K_n(x)$, respectively.

Figure D.1 shows the result of a test calculation. The red points show the numerical solution obtained by our code, and the blue-dashed line shows the analytic solution given in Equation (D.5). We use parameters $q = 5/3$, $t_* = 1$ and $p_0 = m_p c$ in units $D_* = \dot{N}_0 = m_p c = 1$. It is seen that our solutions completely overlap the analytic solution in all the range.

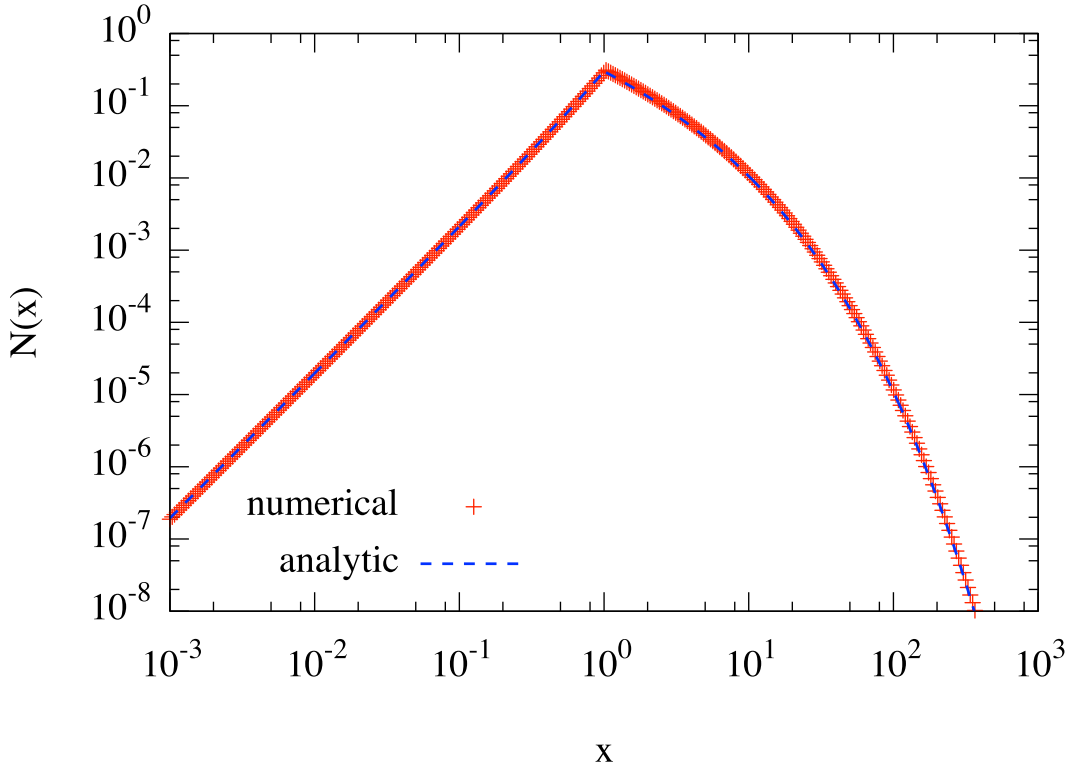

Figure D.1: The proton spectra obtained by numerical method (the red points) and analytic solution (the blue-dashed line). It is seen that our numerical solution completely overlaps the analytic one.

Bibliography

Aartsen, M. G., Abassi, R., Abdou, Y., et al. 2013, PhRvL, 111, 021103

Aartsen, M. G., Abassi, R., Abdou, Y., et al. 2013, Science, 342, 1242856

Aartsen, M. G., Ackermann, M., Adams, J., et al. 2014, PhRvL, 113, 101101

Aartsen, M. G., Ackermann, M., Adams, J., et al. 2015, PhRvD, 91, 022001

Abbasi, R. U., Abu-Zayyad, T., Allen, M., et al. 2008, PhRvL, 100, 101101

Abbasi, R. U., Abu-Zayyad, T., Al-Seady, M. et al. 2010, PhRvL, 104, 161101

Abbasi, R., Abdou, Y., Abu-Zayyad, T., et al. 2011, PhRvD 83, 012001

Abbasi, R. U., Abe, M., Abu-Zayyad, T., et al. 2015, Astropart. Phys., 64, 49

Abdo, A. A., Ackermann, M., Ajello, M., et al. 2009, ApJ, 707, 55

Abdo, A. A., Ackermann, M., Ajello, M., et al. 2010, PhRvL, 104, 101101

Abu-Zayyad, T., Aida, R., Allen, M., et al. 2013, ApJL, 768, L1

Abraham, J., Abreu, P., Aglietta, M., et al. 2008, PhRvL, 101, 061101

Abraham, J., Abreu, P., Aglietta, M., et al. 2010, PhRvL, 104, 091101

Abramowicz, M. A., Chen, X., Kato, S., Lasota, J. P., & Regev, O. 1995, ApJL, 438, L37

Abramowicz, M. A., Czerny, B., Lasota, J. P., & Szuszkiewicz, E. 1988, ApJ, 332, 646

Ackermann, M., Ajello, M., Albert, A., et al. 2014, preprint (arXiv:1410.3696)

Aharonian, F., Akhperjanian, A. G., Bazer-Bachi, A. R., et al. 2006, PhRvL, 97, 221102

Aharonian, F., Akhperjanian, A. G., Anton, G., et al. 2009, A&A, 503, 817

Aharonian, F., Akhperjanian, A. G., Anton, G., et al. 2009, ApJL, 695, L40

Aharonian, F., & Neronov, A. 2005, ApJ, 619, 306

Aharonian, F. A., & Atoyan, A. M. 2000, A&A, 362, 937

Ahlers, M., & Murase, K. 2014, PhRvD, 90, 023010

Ajello, M., Romani, R. W., Gasparrini, D., et al. 2014, ApJ, 780, 73

Alvarez-Muniz, J. & Mészáros, P. 2004, PhRvD 70, 123001

Amenomori, M., Ayabe, S., Cui, S. W., et al. 2006, JPhCS, 47, 51

Anchordoqui, L. A., Goldberg, H., Halzen, F., & Weiler, T. J. 2004, Phys. Lett. B, 600, 202

Apel, W. D., Arteaga-Velazquez, C, Bekk, K. et al., 2013, Astropart. Phys.., 47, 54

Asano, K., & Takahara, F. 2007, ApJ, 655, 762

Atoyan, A. M., & Dermer, C. D. 2001, PhRvL, 87, 221102

Atoyan, A. M., & Dermer, C. D. 2003, ApJ, 586, 79

Balbus, S. A., & Hawley, J. F. 1991, ApJ, 376, 214

Becker, P. A., Le, T., & Dermer, C. D. 2006, ApJ, 647, 539

Becker, P. A., Das, S., & Le, T. 2008, ApJL, 677, L93

Becker, J. K. 2008, Phys. Rept., 458, 173

Becker, P. A., Das, S., & Le, T. 2011, ApJ, 743, 47

Becker Tjus, J., Eichmann, B., Halzen, F., Kheirandish, A., & Saba, S. M. 2014, PhRvD, 89, 123005

Begelman, M. C., Rudak, B., & Sikora, M. 1990, ApJ, 362, 38

Berezinsky, V. 2008, Adv. Space Res., 41, 2071

Bisnovatyi-Kogan, G. S., & Ruzmaikin, A. A. 1974, Ap&SS, 28, 45

Blandford R. D., & Begelman M. C. 1999, MNRAS, 303, L1

Bodaghee A., Tomsick J. A., Pottschmidt K., Rodriguez J., Wilms J., & Pooley G. G. 2013, ApJ, 775, 98

Chandrasekhar, S. 1961, Hydrodynamic and Hydromagnetic Stability (NewYork: Dover)

Chang, J. S., & Cooper, G. 1970, J. Comp. Phys., 6, 1

Chen, X., Abramowicz, M., Lasota, J.-P., Narayan, R., & Yi, I. 1995, ApJL, 443, L61

Chen, X., Abramowicz, M., & Lasota, J.-P. 1997, ApJ, 476, 61

Chen, C. Y., Bhupal Dev, P. S., & Soni, A., 2014, preprint (arXiv:1411.5658)

Chernyakova, M., Malyshev, D., Aharonian, F. A., Crocker, R. M., & Jones, D. I. 2011, ApJ, 726, 60

Coppi, P. S., & Blandford, R. D. 1990, MNRAS, 245, 453

Derbina, V. A., Galkin, V. I., Hareyama, M., et al. 2005, ApJL, 628, L41

Dermer, C. D., Miller, J. A., & Li, H. 1996, ApJ 456, 106

Dermer, C. D., Murase, K., & Inoue, Y. 2014, JHEAp, 3−4, 29

Drury, L. O'C. 1983, Rep. Progress Phys., 46, 973

Eracleous, M., Hwang, J. A., & Flohic H. M. L. G. 2010, ApJS, 187, 135

Esin, A. A., McClintock, J. E., & Narayan, R. 1997, ApJ, 489, 865

Fernandes, C. A. C., Jarvis, M. J., Rawlings, S., et al. 2011, MNRAS, 411, 1909

Gary, S. P., Wang, J., Winske, D., & Fuselier, S. A. 1997, JGR, 102, 27159

Glasmacher, M. A. K., Catanese, M. A., Chantell, M. C., et al. 1999, Astropart. Phys., 10, 291

Goldreich, P., & Sridhar, S. 1995, ApJ, 438, 763

Gonzalez-Garcia M. C., & Nir, Y. 2003, Rev. Mod. Phys. 75, 345 G

Greisen, K. 1966, PhRvL, 16, 748

Gupta, N., & Zhang, B. 2007, Astropart. Phys., 27, 386

Hao, L., Strauss, M. A., Fan, X. et al. 2005, AJ, 129, 1795

Hirose, S., Krolik, J. H., & Blaes, O. 2009, ApJ, 691, 16

Ho, L. C. 2008, ARA&A, 46, 475

Hoshino, M. 2013, ApJ, 773, 118

Howes, G. G. 2010, MNRAS, 409, L104

Inoue, S., & Takahara, F. 1996, ApJ, 463, 555

Jiang, Y. F., Stone, J. M., & Davis, S. W. 2013, ApJ, 778, 65

Jones, F. 1990, ApJ, 361, 162

Kadowaki L.H.S., de Gouveia Dal Pino E.M., & Singh C. B., 2014, preprint (arXiv:1410.3454)

Kalashev, O., Semikoz, D., & Tkachev, I. 2014, preprint (arXiv:1410.8124)

Kashiyama, K., & Mészáros, P. 2014, ApJL, 790, L14

Kashti, T., & Waxman, E. 2005, Physical Review Letters, 95, 181101

Kato, S., Fukue, J., & Mineshige, S. 2008, Black-Hole Accretion Disks-Towards a New Paradigm (Kyoto: Kyoto Univ. Press)

Katz, J. I. 1991, ApJ, 367, 407

Kawasaki, M., Kohri, K., & Moroi, T. 2005, PhRvD, 71, 083502

Kazanas, D., & Ellison, D. C. 1986, ApJ, 304, 178

Kelner, S. R., Aharonian, F. A., & Bugayov, V. V. 2006, Phys. Rev. D, 74, 033018

Kelner, S. R., & Aharonian, F. A. 2008, Phys. Rev. D, 78, 034013

Kimura, S. S., Toma, K., & Takahara, F. 2014, ApJ, 791, 100

Kimura, S. S., Murase K., & Toma, K. 2014, preprint (arXiv:1411.3588)

Komissarov, S. S., Barkov, M. V., Vlahakis, N., & Königl, A. 2007, MNRAS, 380, 51

Kormendy J. & Ho L. C. 2013, ARA&A 51, 511

Kotera, K., Allard, D., Murase, K., et al. 2009, ApJ, 707, 370

Kotera, K., & Olinto, A. V. 2011, ARA&A, 49, 119

Kusunose, M., & Takahara, F. 2012, ApJ, 748, 34

Laha, R., Beacom, J. F., Dasgupta, B., Horiuchi, S. & Murase, K. 2013, PhRvD 88, 043009

Le, T., & Becker, P. A. 2004, ApJ, 617, L25

Le, T., & Becker, P. A. 2005, ApJ, 632, 476

Learned, J. G., & Pakvasa, S. 1995, Astropart. Phys., 3, 267,

Levinson, A. 2000, PhRvL, 85, 912

Li, Y. R., Ho, L. C., & Wang, J. M. 2011, ApJ, 742, 33

Liu, S., Melia, F., Petrosian, V., & Fatuzzo, M. 2006, ApJ, 647, 1099

Loeb, A., & Waxman, E. 2006, JCAP, 5, 003

Lynn, J. W., Quataert, E., Chandran, B. D. G., & Parrish, I. J. 2014, ApJ, 791, 71

Mahadevan R., Narayan R., & Krolik J., 1997, ApJ, 486, 268

Mahadevan, R., & Quataert, E. 1997, ApJ, 490, 605

Malyshev, D., Zdziarski, A. A., & Chernyakova, M. 2013, MNRAS, 434, 2380

Manmoto, T., Mineshige, S., & Kusunose M. 1997, ApJ, 489, 791

Mannheim, K., & Schlickeiser, R. 1994, A&A, 286, 983

Mannheim, K. 1995, Astropart. Phys., 3, 295

Matsumoto, R., Fukue, J., Kato, S., & Okazaki, A. S. 1984, PASJ, 36, 71

McKinney, J. C. 2006, MNRAS, 368, 1561

Murase, K., Ahlers, M. & Lacki, B. C. 2013, PhRvD 88, 121301

Murase, K., Inoue, Y., & Dermer, C. D. 2014, PhRvD, 90, 023007

Murase, K., Inoue, S., & Nagataki, S. 2008, ApJ, 689, L105

Murase, K., Inoue, S., & Asano, K. 2009, IJMPD, 18, 1609

Murase, K., & Ioka, K. 2013, PhRvL, 111, 121102

Murase, K., Ioka, K., Nagataki, S., & Nakamura, T. 2006, ApJ, 651, L5

Mücke, A., & Protheroe, R. J. 2001, Astropart. Phys., 15, 121

Nakamura, E. K., Kusunose, M., Matsumoto, R., & Kato, S. 1997, PASJ, 49, 503

Narayan, R., & Yi, I. 1994, ApJ, 428, L13

Narayan, R., & Yi, I. 1995, ApJ, 452, 710

Narayan, R., Yi, I., & Mahadevan, R. 1995, Nature, 374, 623

Narayan, R., Kato, S., & Honma, F. 1997 ApJ, 476, 49

Narayan R., Sa dowski A., Penna R. F., & Kulkarni A. K., 2012, MNRAS, 426, 3241

Nemmen, R. S., Storchi-Bergmann, T., Yuan, F., Eracleous, M., Terashima, Y., & Wilson, A. S. 2006, ApJ, 643, 652

Nemmen, R. S., Storchi-Bergmann, T. & Eracleous, M. 2014, MNRAS, 438, 2804

Niedźwiecki, A., Xie, F.-G., & Stepnik, A. 2013, MNRAS, 432, 1576

Niedźwiecki, A., Xie, F.-G., & Stepnik, A. 2014, MNRAS, 443, 1733

Oda, H., Machida, M., Nakamura, K., & Matsumoto, R. 2007, PASJ, 59, 457

Ohsuga, K., & Mineshige, S. 2011, ApJ, 736, 2

Paczyński, B., & Wiita P. J. 1980, A&A, 88, 23

Park, B. T., & Petrosian, V. 1996, ApJS, 103, 255

Poutanen, J., & Coppi, P. S. 1998, Phys. Scr., T77, 57

Pozdnyakov, L. A., Sobol, I. M., & Syunyaev, R. A. 1983, ASPRv, 2, 189

Press, W. H., Teukolsky, S. A., William, T. V., & Brian, P. F. 1992, NUMERICAL RECIPES in FORTRAN (Cambridge: Cambridge University press)

Pringle, J.E. 1981, ARA&A, 19, 137

Protheroe, R. J., & Kazanas, D. 1983, ApJ, 265, 620

Protheroe, R. J., & Szabo, A. P. 1992, PhRvL, 69, 2885

Punsly, B., & Zhang, S. 2011, ApJ, 735, L3

Quataert, E., & Gruzinov, A. 1999, ApJ, 520, 248

Quataert, E., Dorland, W., & Hammett, G. W. 2002, ApJ, 577, 524

Riquelme, M. A., Quataert, E., Sharma, P., & Spitkovsky, A. 2012, ApJ, 755, 50

Ross, R. R., Fabian, A. C., & Mineshige, S. 1992, MNRAS, 258, 189

Romero, G. E., Vieyro1, F. L., & Vila, G. S., 2010, A&A, 519, 109

Rybicki, G. B., & Lightman, A. P. 1979, Radiative Processes in Astrophysics (New York : Wiley)

Sadowski, A., Narayan, R., Penna, R., & Zhu, Y. 2013, MNRAS, 436, 3856

Sahakyan, N., Yang, R., Aharonian, F. A., & Rieger, F. M. 2013, ApJL, 770, L6

Sano, T., Inutsuka, S., Turner, N. J., & Stone, J. M. 2004, ApJ, 605, 321

Shakura, N. I., & Sunyaev, R. A. 1973, A&A, 24, 337

Sharma, P., Hammett, G. W., Quataert, E., & Stone, J. M. 2006, ApJ, 637, 952

Sharma, P., Quataert, E., Hammett, G. W., & Stone, J. M. 2007, ApJ, 667, 714

Sironi, L. 2014, preprint (arXiv:1411.6014)

Sironi, L., & Narayan, R. 2014, preprint (arXiv:1411.5685)

Spitzer, L. 1962. Physics of Fully Ionized Gases (New York: Interscience)

Stawarz, Ł., & Petrosian, V. 2008, ApJ, 681, 1725

Stecker, F. W. 1968, PhRvL, 21, 1016

Stecker, F. W. 2005, PhRvD, 72, 107301

Stecker, F. W. 2013, PhRvD, 88, 047301

Stecker, F. W., Done, C., Salamon, M. H., & Sommers, P. 1991, PhRvL, 66, 2697

Stepney, S. 1983, MNRAS, 202, 467

Stone, J. M., & Norman, M. L. 1992, ApJS, 80, 753

Subramanian, P., Becker, P. A., & Kazanas, D. 1999, ApJ, 523, 203

Szabo, A. P., & Protheroe, R. J. 1994, Astropart. Phys., 2, 375

Takahara, F., & Kusunose, M. 1985, Prog. Theor. Phys., 73, 1390

Takami, H. 2010, MNRAS, 413, 1845

Takami, H., Murase, K., & Dermer, C. D. 2014, preprint (arXiv:1412.4716)

Tamborra, I., Ando, S., & Murase, K. 2014, JCAP, 9, 043

Tavecchio, F., Ghisellini, G., & Guetta, D.,2014, ApJL, 793, L18

Toma, K., & Takahara, T. 2012, ApJ, 754, 148

Ueda, Y., Akiyama, M., Ohta, K., & Miyaji, T. 2003, ApJ, 598, 886

Velikhov, E. P. 1959, Sov. Phys. JETP, 36, 995.

von Neumann, J., & Richtmyer, R. D. 1950, Appl. Phys., 21, 232

Waxman, E., & Bahcall J., 1998, Phys. Rev. D 59, 023002

Winter, W. 2013, PhRvD, 88, 083007

Yuan, F. 2001, MNRAS, 327, 119

Yuan, F., Quataert, E., & Narayan, R. 2003, ApJ, 598, 301

Yuan, F., Cui, W., & Narayan, R. 2005, ApJ, 620, 905

Yuan, F., Wu M., & Bu D. 2012, ApJ, 761, 130

Yuan, F., & Narayan, R. 2014, ARA&A, 620, 905

Zandanel, F., Tamborra, I., Gabici, S., & Ando, S. 2014, preprint (arXiv:1410.8697)

Zatsepin, G. T., & Kuzmin, V. A. 1966, JETPL, 4, 78

Zdziarski, A. A., Poutanen, J., Paciesas, W. S., & Wen, L. 2002, ApJ, 578, 357

Paper List

Primary papers for this thesis

- Kimura, S. S., Toma, K., & Takahara, F. 2014, ApJ, 791, 100
- Kimura, S. S., Murase K., & Toma, K. 2014, ApJ submitted (arXiv:1411.3588)

Other papers

- Kimura, S. S. & Tsuribe, T. 2012, PASJ, 64, 116
- Yamaguchi, M. S. & Kimura, S. S. 2014, EPS, 66, 132
- Ohtani, T., Kimura, S. S., Tsuribe, T., & Vorobyov E. I. 2014, PASJ, 66, 112